CHEMO-MECHANICAL AND THERMAL BEHAVIOR OF 3D PRINTED CEMENT COMPOSITES

By

Michael Tillman Kosson

Dissertation

Submitted to the Faculty of the

Graduate School of Vanderbilt University

In partial fulfillment of the requirements

for the degree of

DOCTOR OF PHILOSOPHY

in

Chemical and Biomolecular Engineering

August, 12, 2022

Nashville, TN

Approved:

Florence Sanchez, PhD

G. Kane Jennings, PhD

Douglas E. Adams, PhD

Joseph J. Biernacki, DRE, PE

Carlos A. Silvera Batista, PhD

For all the people who supported and encouraged me along the way.

ACKNOWLEDGEMENTS

I would like to thank my committee members for all of their time and insight: Dr. G. Kane Jennings, Dr. Joseph Biernacki, Dr. Douglas Adams, and Dr. Carlos Silvera Batista. I would especially like to thank my advisor, mentor, and committee chair, Dr. Florence Sanchez, for all of her guidance and advice for the past five years; for the countless hours in her office, at her dining room table, and on Zoom; and for providing me the trust and flexibility to take care of myself in what has been a world of unusual circumstances.

Thank you to all of the Vanderbilt staff who have helped me with so many things in the laboratory and administratively. I would especially like to thank Dr. Lesa Brown, who has helped me every step of the way and without whom I would never have accomplished so much of what I have. Thank you also to Rossane Delapp, Rich Teising, Darlene Weaver, Felisha Baquera, and everyone else. Thank you to Hunter Conti, my excellent undergraduate research assistant.

I cannot express enough gratitude to my partner in all things, Sarah Kendrick, for all of her encouragement, support, and love; for dealing with my frustrations and my bad jokes. Thank you to my family for everything you have done for me: Mom, Dad, Gabe, Garette, and Ryan, especially the months you let me move into your guest room. Dad, thank you for being able to wear a ‘Dad hat’ and a ‘Dr. Kosson hat’. Thank you to Robin and Marvin, especially for the months you let me move into *your* guest room. I love you all and I could not be more fortunate.

I will forever be appreciative for the relationships I have been able to build at Vanderbilt, and while I cannot name everyone, I would especially like to thank Joshua Passantino, Madeline Johnson, Hannah Stephens, and Tyler Stephens for being my other family at Vanderbilt and for the many shenanigans. I will never forget the gold medal curling match or those weekends at the lake. Thank you to Autumn Taylor, there’s nobody else who would have let me drag them into the lab so many weekends. Thank you to Jonah Rosch, Mohsin Rahim, and Josh again, who lived with me for all those years at the Robertson house. Thank you to my friends from Tulane who have continued to support me and who learned the difference between cement and concrete: Joel Straus, Ben Salwen, Brian Lynch, and Emily Acker. Thank you to Dansby for being a very good boy.

Finally, I would like to thank the organizations that have provided me with funding during my graduate studies: the National Science Foundation under NSF CMMI 1563389, a collaboration with colleagues at Tennessee Technological University and Purdue University, Vanderbilt University under a Discovery Grant and a Trans-Institution Program Vanderbilt Reinvestment Award, and Dr. Florence Sanchez from her faculty development fund.

TABLE OF CONTENTS

Page

LIST OF TABLES

Table Page

List of Figures

Figure Page

CHAPTER 1

INTRODUCTION

1.1. Overview

3D printing is a process by which structures are built up layer-by-layer by progressively adding material to create a three-dimensional object. Also known as additive manufacturing, 3D printing has experienced rapid growth into new technologies and applications [1-8]. Meanwhile, growth in worker productivity and profit margins in the infrastructure and construction industries have lagged behind those for other industries, and these industries produce more than 21 million tons of concrete waste in the United States alone per year [2, 9]. Advances in 3D printing, specifically the 3D printing of cementitious materials, may provide the technological basis to help break the productivity stagnation and reduce waste in these industries.

While concrete – the most ubiquitously used construction material in the world – is materially inexpensive, traditional casting methods have very high associated labor cost, resulting in complexity and customization being expensive. By automatically depositing material based on a computer-generated model, 3D printing allows greater freedom for customization compared to traditional casting techniques, reduces the cost of creating sophisticated architectural designs, and shortens design and development cycles [7, 8]. It could also allow for a reduction in expenses relating to labor and formwork, which account for between 35% and 60% of the cost of building concrete structures [9]. However, because cementitious materials are subject to more constraints to be appropriate for use as 3D printing inks compared to casting, the development of new materials and a better understanding of the interplay between ink formulation, extrusion process, and mechanical and thermal properties are needed to make 3D printing commercially viable.

Internal fiber reinforcement [10-24] and nanoparticle inclusion [18, 25-34] have been identified as approaches, which can impact the cement ink behavior, improving mechanical performance and rheological control. Many types of fiber reinforcement and nanoparticles have been investigated, but for the research presented here, the focus has been on carbon micro and nanofibers – due to their outstanding strength-to-weight ratio making them promising

reinforcement candidates [35-41] – and halloysite nanoclay – due to its demonstrated effects on rheology and hardened mechanical properties and its high aspect ratio [42-45]. While many studies have focused on the rheological properties of cement inks [18, 46-62] and the mechanical anisotropy caused by the layer-by-layer building process [33, 52, 63-82], very little research has focused on the effects of the extrusion process on the chemo-mechanical behavior of the filaments or on the anisotropy of the thermal properties [83-85].

Hypothesis: Interactions between the printing process and cement ink formulation can result in changes in the microstructure and phase assemblages of extruded filaments, which, in turn, impact the macroscale mechanical and thermal performance of printed structures. These interactions can be controlled by changing the cement ink formulation through internal nano and microscale reinforcements and nanoparticle addition.

1.2. Objectives and Approach

The *overall objective* of the research was to investigate the relationship between the 3D printing process and the multiscale chemo-mechanical performance of extruded cementitious filaments and how that relationship can be controlled through cement ink formulation. To-date, most research has investigated the relationship between rheology and printability, anisotropic macroscale mechanical behavior, and the behavior of interlayer interfaces, and little to no research has focused on the impact of the printing process on the chemo-mechanical behavior of the printed filaments. In particular, the composition of extruded filaments can be dynamically affected by the pressure and shear stresses inherent to extrusion, resulting in the formation of a watery lubrication layer at the surface of extruded filaments and the potential for microstructural reorganization [86-88]. The prevalence of filament heterogeneity caused by extrusion pressure can be affected through the addition of carbon micro/nanofibers and nanoclays, through alignment of particles in the direction of extrusion, hydrophobic/hydrophilic interactions with the paste water, or through migration of the particles themselves under extrusion pressure. Additionally, the effects of internal architecture and ink composition on the thermal performance of printed structures have not been adequately investigated. The chemo-mechanical performance of 3D printed filaments and structures with and without the incorporation of carbon micro and nanofibers and halloysite nanoclay was investigated by analyzing (i) filament formation and

morphology, (ii) physical and chemical properties of the microstructure, (iii) micromechanical properties, and (iv)physical and chemical properties of the microstructure. The relationship between cement ink formulation, internal architecture, and thermal performance was also investigated. The four *specific objectives* addressed in this dissertation are:

1. Investigate the effects of the 3D printing process on the microstructure and micromechanical properties of printed filaments
2. Determine the effects of internal carbon micro and nanofiber reinforcement on the microstructure and macroscale mechanical properties of 3D printed cementitious structures
3. Characterize the effects of halloysite nanoclay addition on the microstructure and mechanical response of 3D printed cementitious filaments and structures
4. Evaluate the effects the internal architecture of 3D printed cementitious filaments and halloysite nanoclay addition on the thermal performance of 3D printed cement-based structures

A multiscale experimental approach was used that examined the material behavior from the microstructure within extruded filaments to the macroscale properties of printed structures. For all experiments, specimens cast with the cement ink were utilized as references to identify the effects of the printing process. The approach integrates microstructural characterization with environmental scanning electron microscopy, chemical characterization with energy-dispersive X-ray spectroscopy and thermogravimetric analysis, macromechanical characterization with uniaxial compression and three-point bending testing, and thermal characterization with an infrared imaging technique. The selection of cement ink additions was carefully considered to increase the understanding of the effects of common approaches to addressing the requirements of 3D printing with cementitious materials (i.e., internal reinforcement and rheology-control additives) on the multiscale behavior of the printed filaments and structures. The research aims to provide a better understanding of the relationships between the printing process, filament properties, and macroscale mechanical and thermal performance.

1.3. Structure of the Dissertation

This dissertation is organized into seven chapters. Chapter 2 contains a review of relevant literature pertaining to the research in this dissertation. Chapter 3 discusses the effects of extrusion process on the chemical and microstructural behavior of printed filaments. The

microstructure and micromechanical properties of printed filaments were investigated through coupled statistical grid nanoindentation, environmental scanning electron microscopy, and energy dispersive X-ray spectroscopy. Chapter 4 discusses the impacts of carbon micro and nanofiber addition to the cement ink on filament formation, microstructure, and macroscale mechanical properties. The microstructure was investigated with environmental scanning electron microscopy, chemistry with energy dispersive X-ray spectroscopy and thermogravimetric analysis, and macroscale mechanical properties with uniaxial compressive testing. Chapter 5 discusses the effects of halloysite nanoclay incorporation into the cement ink on filament formation, microstructure, chemistry, micromechanics, and macroscale mechanical properties. Microstructure, chemistry, and micromechanics were collected with a similar experimental program as for Chapter 3 to compare cement inks with and without halloysite nanoclay. Macroscale mechanical properties were investigated with uniaxial compression and three-point bending flexure testing. Chapter 6 discusses the impact of internal architecture and the addition of halloysite nanoclay on the thermal performance of printed structures. Thermal performance was investigated through an infrared imaging technique, which yields comparative effective conductivity properties. Finally, Chapter 7 summarizes the results of this research and presents recommendations for future work.

CHAPTER 2

LITERATURE REVIEW

2.1. Overview

This section provides a synopsis of the literature relating to the research detailed in this dissertation. An overview of the state of extrusion-based 3D printing with cementitious materials is provided, including fresh state properties and printability, as well as hardened macro and micromechanical properties and anisotropy. Also discussed are reinforcement strategies, particularly the incorporation of short fibers (typically less than 5 cm in length) in cement inks. Next is a brief overview of the effects of nanoclays in cementitious materials with a focus on their use in cement inks and an overview on halloysite nanoclay, which was the nanoclay type used for the research in this dissertation. Finally, the thermal performance of buildings and the opportunity offered by 3D printing to improve thermal control o are discussed.

2.2. Construction-Scale 3D Printing

3D printing, also known as additive manufacturing, was first invented in the 1980's as a method by which a computer model could be used to produce a three-dimensional structure by stacked cross-sections [89]. With computational and hardware advances, 3D printing has become increasingly popular, particularly with thermoplastic materials. By having a robotic layer-by-layer deposition or bonding of material, complex geometries which may be difficult or impossible to construct with traditional methods can be created cheaply and easily. More recently, interest has grown in adopting 3D printing methods for construction, particularly with cement-based materials printed by extrusion [7].

Concrete is the most ubiquitously used material in the world after water [8]. It is attractive as a structural material due to its low material cost and characteristically high compressive strength. However, concrete-based construction is labor-intensive and produces a large amount of waste, particularly due to single-use formwork, which is used to shape poured concrete. Labor and formwork costs typically account for 35 to 60% of the cost associated with concrete construction [9]. Additionally, concrete is a carbon-intensive material, primarily due to the high energy demand of the cement production process, which accounts for about 5 – 7% of global carbon

emissions [90]. By building in an automated and formwork-free fashion, 3D printing can improve construction efficiency and sustainability. It can also improve architectural design freedom by reducing the cost associated with complex geometry and increasing material flexibility [7, 8]. By placing material only where necessary for the functionality of a building and by increasing the possibility of incorporating alternative materials, 3D printing can be used to reduce the environmental impact of the construction industry [91].

However, there are technical challenges, which must be addressed before construction-scale 3D printing can be widely adopted. For a cement-based material to be appropriate for use as a 3D printing 'ink', it must have appropriate rheology in the fresh state to allow both extrusion and buildability. It must provide adequate material properties in the hardened state despite the introduction of anisotropy from the directionality of the printing process. Reinforcement strategies must be developed due to the practical limitations of using traditional steel rebar lattices with an extrusion process [1-4, 6, 8, 48, 61, 92, 93]. Also, the relationship between ink composition, printed architecture, and thermal performance needs to be better understood [94]. Consideration should, therefore, be given to identify the complex relationships between the printing process, cement chemistry, microstructure, and macrostructural behavior and to utilize the findings to develop new cement inks.

2.3. Fresh Properties and Printability Requirements of Cement Inks

The window of appropriate rheological characteristics for a cementitious material to be used as a 3D printing cement ink is much narrower than that of traditional casting methods, as cement inks have competing workability and shape-stability requirements. A cement ink must be sufficiently workable that it can be formed into filaments, extruded, and compacted without vibration, while also having sufficient buildability to hold its shape without slump or deformation once it has been placed and under the weight of subsequent layers. It must set as quickly as possible for early-age strength development, but not so quickly that interlayer adhesion is negatively affected or cold-joints are formed between layers [4, 8, 54, 61, 62]. Some of these requirements can also be affected by printing process parameters and conditions. For example, the time between layer depositions can be tuned to provide for the bleeding and set time characteristics of the cement ink. Consequently, the relationship between the fresh properties of the ink and the process parameters must be carefully considered to ensure printability [53, 54, 59, 60].

Workability, or the ease with which cementitious materials may be mixed, compacted, and placed, is an important component of printability [57, 58]. Traditionally, several tests are used to determine the workability of concrete, including the slump test, compacting factor tests, and flow tests, which are covered by various standards in many countries [54, 57]. Sufficient paste workability is required for 3D printing applications in order to ensure that air voids may be removed before extrusion and that the paste may be properly shaped into filaments during extrusion [54]. Practically, workability has two components: dynamic yield stress and plastic viscosity.

Cementitious materials are often modeled as a Bingham fluid or a Herschel Bulkley fluid, with the three-parameter Herschel Bulkley considered to do a better job of approximating the non-linear stress-strain relationship than the two-parameter Bingham model [95, 96]. In many cases, these models are useful for predicting the flow behaviors of fresh pastes because they account for the fact that fresh cementitious materials do not flow below a critical dynamic yield stress [46, 62, 95, 97]. However, these models assume that the paste behaves as a homogenous fluid, ignoring the tendency of the component materials to segregate, particularly when exposed to the pressure required for extrusion. Cementitious materials have been shown to produce a lubrication layer at the pipe wall when pumped, caused by the migration of suspended particles away from the walls of the pipe (or the printing nozzle in the case of 3D printing). Their pumpability is influenced by their ability to form and maintain the lubrication layer under pumping conditions, and models that do not account for its formation do not accurately predict the pumping and extrusion behavior of fresh cementitious materials [3, 8, 52, 58, 86, 98-102]. Furthermore, the thickness and behavior of the lubrication layer is affected by the composition of the paste mix [3, 99], and so must be carefully considered during mix design.

During pumping, it has been shown that particle migration is primarily shear-induced or caused by wall effects. These effects are likely to be exacerbated by the relatively narrow diameter through which the ink is to be extruded in many 3D printing systems, due to the higher surface area-to-volume ratio of such systems. Shear-induced particle migration is the result of the competing driving forces of colliding particles in zones that are highly sheared or highly concentrated zones migrating out of those zones and the local increase in suspension viscosity caused by this migration. Consequently, particle migration tends to be localized to regions of

high shear and at flow interfaces. This process is thought to be largely responsible for the formation of lubrication layers at the nozzle wall, as cement and aggregate particles migrate away from the high-shear wall region [99, 101-103]. Therefore, the material must also maintain resistance to dynamic segregation or flow induced particle migration to preserve adequate particle distribution in the hardened paste. Printing discontinuity errors caused by nozzle blockages due to particle segregation are of particular concern for cement inks [61]. Additionally, for sensitive mixes, particle segregation may destabilize the paste to the extent that water drainage occurs, preventing it from being an effective ink [86-88]. In order to combat drainage, viscosity modifying admixtures and ultrafine substances such as nanoclay and silica fume may be added to the ink [88]. However, **there has been little to no investigation into the relationship between the printing process, shear-induced particle migration, and hardened microstructure and mechanical properties.**

Once placed, an extruded filament must have sufficient buildability, or the ability to hold its shape after being extruded, and then to bear the weight of subsequent layers in its fresh state without significant filament deformation or structure collapse [46, 51-56]. In order to prevent print failure due to extruded filament deformation, a cement ink must have a sufficiently high static yield stress [49, 50], which is contrasting with the requirement of sufficiently low dynamic yield stress for extrudability, thereby narrowing the range of pastes that may be considered printable. One approach is to take advantage of the structural buildup inherent to cementitious materials to improve this relationship. Cementitious materials are generally thixotropic, meaning that their viscosity is reversibly time dependent relative to the material being sheared. As more time passes since the material has been sheared (i.e., extruded) the yield stress of the material increases, making the time between layers an important factor in an ink's buildability [18, 46-48]. There are several types of additives, which have been utilized to increase the thixotropic behavior and improve buildability of cement inks, including nanoclays [18, 25-31]**. The effects of printability additives on hardened microstructure and mechanical properties requires, however, further investigation.**

2.4. Hardened Mechanical Properties and Anisotropy

In addition to printability requirements, a cement ink must have sufficient hardened material properties to be useful as a structural material. Like traditionally cast cementitious materials, 3D

printed cementitious materials have characteristically high compressive strength and are comparatively weak and brittle in tension. However, the layer-by-layer and orientational nature of extrusion-based 3D printing methods introduce significant mechanical anisotropy – the mechanical properties are dependent on the directionality in which they are tested [80-82].

In compression, 3D printed structures have generally performed similarly to cast references when tested with load applied perpendicular to interfacial alignment, with some studies reporting 3D printed specimens to be slightly stronger than cast references, presumably due to densification of the paste during extrusion [52, 79]. In flexure, printed structures have been reported to have 6-14% higher strength than reference cast samples when load is applied orthogonally to filament orientation, but significant reductions have been found in other orientations [52, 63, 79].

For many 3D printed cementitious structures, the interlayer interfacial region is the first point of failure and the largest source of material anisotropy [8, 65, 69, 76-78]. There are several mechanisms thought to contribute to the relative weakness of interfacial regions. It has been shown that interlayer bonding strength is greatly affected by the amount of water that is present on the surface of the filaments when they are joined, as its presence promotes interlayer mixing [33, 71, 75]. Consequently, the cycle time between the deposition of each layer has been found to greatly influence interlayer bonding strength. Short cycle times have been found to promote strong interfacial bonding, as there is water present due to extrusion pressure-induced segregation. However, as the cycle time increases, interlayer bonding strength decreases, and several studies have found that it reaches a local minimum at a cycle time of 15 to 20 minutes. Initially, surface water level decreases due to evaporation, but after reaching a minimum level, bleeding increases surface water until the paste begins hardening [59, 75, 80]. Longer cycle times have generally been found to produce weaker interlayer bonds with higher porosity [63, 64, 70, 72-74]. It has also been suggested that thixotropic buildup in the lower layer, while beneficial to ink buildability, may prevent mixing with subsequently placed layers to some degree [33, 68-70]. Several other factors also play an important role in determining interlayer bonding strength, including print quality, bond area, and factors influencing ink rheology such as aggregate content and paste age [63-66, 71]. Interfacial bonding strength has been found to vary from system to system, ranging from interfaces that are effectively as strong as the bulk filament

material to quasi-cold joints, which are consistently the origin of material failure during testing [63-67]. It has also been demonstrated that with careful design of the architecture, weak interfaces can be utilized to increase toughness and flaw tolerance by promoting damage delocalization [104].

However, despite studies on the anisotropic nature of printed structures, the effects of the extrusion process on the hardened filaments themselves has yet to be understood, especially with regards to the multiscale nature of cementitious materials. While cementitious materials are generally considered to be homogenous at the macroscale, cement microstructure is a complex arrangement of chemical phases that interact to impart macroscale properties. Consequently, changes to the local composition of filaments caused by extrusion pressure-induced segregation may lead to stronger and weaker zones in the hardened microstructure, and **the impact of the extrusion process on the microstructure and micromechanical properties of the filaments requires investigation.**

Nanoindentation is a method that uses a diamond-tipped probe with known mechanical properties to determine the local mechanical properties of the probed area within the microstructure. Statistical grid nanoindentation, whereby a representative collection of indents to characterize micromechanical phases is collected, has been relatively widely used to investigate the micromechanical properties of cementitious materials, but there have been few micromechanical investigations of 3D printed cementitious materials, and they have focused on inter-filament interfacial characteristics rather than the effect of the printing process on bulk filament properties or been very limited in scope [74, 105]. These studies have demonstrated a strong relationship between ink workability, printing parameters, and the micromechanical properties of interfilament interfacial regions, with poor interlayer bonding corresponding to significant reduction in micromechanical properties [74] and investigated the role of microstructural randomness as a computational modeling parameter [105].

2.5. Reinforcement Strategies and Short Fiber Reinforcement

One practical limitation of 3D printing cementitious materials is that it is largely incompatible with traditional reinforcement strategies. Specifically, because the paste is not poured into a formwork structure in which rebar may be prearranged, it is not possible to provide tensile

reinforcement in this way. Because cementitious materials are broadly characterized as being strong in compression but weak in tension, some form of tensile reinforcement is necessary for 3D printed cementitious materials to be industrially viable [61, 106, 107]. Several novel reinforcement solutions have been proposed by various authors, including printing over simultaneously placed steel cables [108-111], printing with designed voids which rebar can be added to after hardening [112], placing wire mesh between [113] or across [114] printed layers, and printing steel reinforcement simultaneously with printed concrete [115].

The most common approach has been the addition of short fibers to the cement ink during initial mixing. Short fiber reinforcements are easy to incorporate and have been shown to significantly increase the strength and ductility of 3D printed cementitious materials and to be effective at mitigating shrinkage [10-24]. Fibers have been considered as a reinforcement strategy for 3D printed cementitious materials since as early as 2011, although that study does not include details about fibers used or their effects [112]. A variety of fiber types have been investigated in 3D printing, including glass, basalt, carbon, and a wide variety of polymers.

Fibers have been reported to align in the direction of printing, thereby significantly contributing to the mechanical anisotropy of printed structures [18, 24, 106]. This is particularly true when the fibers are longer than the diameter of the nozzle through which they are extruded. While the degree of fiber alignment is likely to be reduced as the printing nozzle is scaled up, some degree of alignment can be expected due to shearing in the flow profile of the ink [18]. This control of fiber alignment provides the opportunity to tune the material properties for its intended use, utilizing mechanical anisotropy to the benefit of the design application. Fiber alignment is generally thought to be most beneficial to mechanical properties when flexure load is applied perpendicularly to the direction of orientation (or parallel for tension) [20, 24]. This effect has led to higher flexure strength being reported for some 3D printed fiber reinforced cementitious materials compared to the same mixture when cast [17, 18]. Such materials have also been demonstrated to have post-yield strain-softening behavior, as well as improved ductility from improved deflection capacity and fracture energy [14, 17]. Consequently, the degree of strength improvement was found to be influenced not only by the type of fiber used, but also by the print pattern utilized (and therefore the fiber alignment relative to the loading direction), with the greatest improvement in flexure strength being conferred when load is applied perpendicular to

filament alignment [13, 24]. However, fiber alignment can also have detrimental effects on printed structures in some cases, as it can promote failure through fiber pull-out, which is the dominant fiber failure mechanism rather than fiber yielding in some systems [14, 17, 20, 21, 116].

In some cases, fiber reinforcement has been found to correspond to weaker interlayer bonding, with higher fiber loading corresponding to a larger interlayer bond strength reduction. It was hypothesized that the reduction in interlayer bond strength was due to an increase in stiffness of the fresh paste, reducing the effectiveness of interlayer bonding [14, 117], as fibers have been shown to affect paste rheology [118, 119].

While the mechanical behavior of short fiber reinforced 3D printed cement-based materials have been shown to be influenced by the printing process and fiber alignment along the print direction [10, 13, 24, 120], **there is limited information on the effect of the fibers during the extrusion process and the resulting microstructure of the printed material.** Yet, understanding the influence of the fibers on the filament formation is important for tailoring the properties of 3D printed cement-based materials. In addition, **3D printing of cement-based materials with carbon nano and microfibers has received little attention**, despite the demonstrated benefits of carbon fibers in traditional cast concrete, including strength improvements and smart property capabilities [35-41].

2.6. Nanoclay Incorporation in Cement-based Materials

Nanoclays have been identified one class of materials, which can be used to improve the performance of cement inks in the fresh state, and can be used to improve mechanical properties in hardened state [25-30, 32, 33]. In the fresh state, nanoclays have been shown to improve printability by increasing thixotropic behavior [32-34]. When exposed to shear stresses, thixotropic particles are dispersed in the paste water in a colloidal suspension. After shearing ceases, particles rapidly flocculate out of suspension, causing structural build-up [121]. The resulting time dependency for rheological behavior allows the cement ink to be workable during filament formation and extrusion, while also having a higher static viscosity once it has been placed for better buildability. Nanoclays also benefit the stability of cement inks through their hydrophilicity, which helps to hold the paste together under pressure and reduce segregation

[32]. This stability-enhancement is of particular interest as a means to allow the inclusion of otherwise beneficial materials which may negatively impact paste cohesion, particularly hydrophobic short fibers such as carbon nanofibers. In the hardened state, nanoclays have been shown to be beneficial to mechanical performance of cementitious materials through pozzolanic activity by reacting with calcium hydroxide to form calcium silicate hydrate gel, the main structural component of cementitious materials, and by providing a filling effect that densifies pore structures [32, 44, 122, 123].

Halloysite nanoclay (HNC) is a type of nanoclay that is of particular interest. In addition to having demonstrated similar benefits on cementitious materials as other nanoclays in the fresh [45] and hardened states [44], HNC has a high aspect ratio, needle-like structure, which may provide additional benefit by bridging microcracks and providing a degree of internal reinforcement [42, 43], which may be enhanced by preferential alignment of HNC particles during 3D printing. HNC particles are typically 30-70 nm in diameter and 1-3 μm in length and are composed of multi-walled tubes, with a siloxane outer layer and aluminol inner layer [124].

As nanoclays become more popular as a printability aid, a better understanding the relationship between the printing process, nanoclay addition, and hardened properties is required. To date, no studies have focused on the effect of nanoclay addition on the hardened properties of extruded filaments, or how nanoclay addition interacts with extrusion pressure to impact the microstructure.

2.7. Thermal Performance of Buildings and 3D Printed Cement-based Materials

Global demand for new buildings continues to rise, with the total number of buildings on Earth expected to double by 2060 [125] and environmental heating and cooling projected to account for 49% of the total growth in energy demand by 2050 [126]. With the energy performance of buildings being one of the primary determining factors for this increase in energy demand, developing new materials and technology to improve thermal building envelope performance has been identified as being of particular importance [126]. Consequently, global investment in improving building energy efficiency has grown rapidly in recent years, from $129 billion in 2015 to $180 billion in 2020, and continues to accelerate [127].

Much of the recent research on improving the thermal performance of building envelopes has been on developing new cementitious materials with improved thermal characteristics. In particular, development has focused on modifying cement microstructure by altering the pore structure or by including materials that can absorb changes in thermal conditions (phase change materials). Pore structure optimization has been researched extensively to develop cement-based materials with improved thermal characteristics [128-131], with many techniques and material inclusions having been evaluated for impact on pore structure and thermal performance, including air-entraining additives [132-134], lightweight and porous aggregates [133, 135-142], and chemically active additives such as bentonite nanoclay [143], silica fume [144, 145], or fly ash [144, 146, 147]. Phase change materials, which utilize the enthalpy of fusion of materials with freezing/melting points in relevant ranges for climate control to buffer against cyclical temperature changes and reduce thermal load, have also been studied extensively as a method to improve the thermal performance of building materials. Commonly studied phase change materials, which are often microencapsulated to minimize chemical interaction with the surrounding material include organics such as paraffin wax and inorganics such as salt hydrates. Such materials must have favorable thermal characteristics and be compatible with the rheological and structural requirements of the material in which they are incorporated, though they generally result in a reduction in mechanical performance [148-151].

3D printing has also been identified as a technology for improving the thermal performance of building envelopes by utilizing specially designed internal architecture and void spaces within building envelopes to introduce thermal anisotropy which can induce directional heat-flow and help to improve thermal control [83-85, 152-158]. By selectively placing cement ‘ink’ filaments only where designated to build structures up layer-by-layer, 3D printing can be utilized to tune material placement, such that structural and thermal considerations can be accounted for in material selection and structural design. While much of the research focus for 3D printing with cement-based materials has been on ensuring appropriate rheology for printability and hardened mechanical properties, thermal performance has recently garnered increased attention as a design consideration, utilizing several strategies including tuning internal architecture, phase-change materials, foaming concrete, and polymer-foam injected into void spaces to improve thermal conductivity and thermal storage capacity [25, 83, 84, 94, 158-165]. However**, while there have been several studies, which have used computational modeling to investigate the**

relationship between internal architecture and thermal performance in 3D printed cement-based materials [152-158]**, there has been little experimental investigation** [83-85]**.** The ability of 3D printing to create hierarchical structures may also create new opportunities for improving thermal performance, with the composition, architecture, and properties of the material changing within the structure to account for the structural and thermal requirements of specific locations [7, 158]. In this way, thermal anisotropy can be leveraged to improve building thermal performance.

Additionally, while nanoclays have become popular in cement inks as a printability aid, comparatively little attention has been paid to the effect of nanoclay inclusion on the thermal properties of cementitious materials or on its effect at higher temperatures that are relevant for building envelopes [143, 166-168]. To the knowledge of the author, **no published studies have investigated nanoclay thermal performance in 3D printed structures.** Still, because they impact pore structure, they can be expected to affect thermal properties. Halloysite nanoclay (HNC) is of particular interest due to reported reduction in thermal conductivity of cementitious materials in some cases [167, 168], as well as its high aspect ratio and needle-like structure. The potential for preferential alignment of HNC's needle-like structure during printing may also increase thermal anisotropy.

2.8. Conclusions

A synopsis of the previous literature relating to the research detailed in this dissertation was provided. The following conclusions could be drawn:

- Given the tendency for extruded filaments to form a lubrication layer, a better understanding of the complex relationships between extrusion, shear-induced segregation, and hardened microstructure and mechanical properties is needed.
- The 3D printing process has been shown to introduce significant anisotropy to the mechanical properties of 3D printed structures, which must be accounted for in structural design, but can also be leveraged for hierarchical design. However, further investigation is required on the impact of 3D printing on bulk filament microstructure.
- Because 3D printing does not allow for traditional reinforcement and because of demonstrated benefits of carbon fibers as reinforcement in cast cementitious materials,

further research is needed into the fiber reinforcing abilities of carbon nano and microfibers and their influence on the extrusion process and the resulting hardened microstructure and macroscale properties.

- Nanoclays have been identified as thixotropy-improving additives in cement inks and have been shown to improve hardened properties in non-printing applications, but the effect of the relationship between nanoclays and the printing process on hardened properties has not been investigated.
- As thermal performance of building envelopes becomes increasingly important, the effect of internal architecture and ink composition on the thermal performance of printed structures requires additional experimental investigation.

CHAPTER 3

NANOMECHANICAL CHARACTERIZATION OF 3D PRINTED CEMENT PASTES

The results of this chapter are being incorporated into the following manuscript:

Kosson M., Brown L., and Sanchez F. Nanomechanical Characterization of 3D Printed Cement Pastes. Submitted June 2022.

3.1. Overview

In this study, statistical grid nanoindentation paired with environmental scanning electron microscopy (ESEM) and energy dispersive X-ray spectroscopy (EDS) was utilized to examine the micromechanical properties (modulus and hardness) and microstructure of filaments in 3D printed cement paste structures. Cast specimens created using the same cement ink formulation and a formulation with a higher water-to-cement (w/c) ratio were also tested as references for comparison. The effect of the extrusion process on the distribution of the C–S–H phases is also reported. Results showed that the extrusion through a small-diameter nozzle affected the mesoscale agglomeration process of the primary hydrate phases and that the local packing arrangement was the dominant factor in the micromechanical response of the printed filaments.

3.2. Materials and Methods

3.2.1. Materials

For the cement ink, Type I/II portland cement (LafargeHolcim, USA) was the binding agent. MasterGlenium 7700 (BASF, USA), a high-range water reducing admixture, was used to lower viscosity and increase workability to allow the cement ink to be extruded freely. MasterMatrix VMA 362 (BASF, USA), a viscosity-modifying admixture and MasterMatrix UW 450 (BASF, USA), a liquid cellulose-based anti-washout admixture, were used to increase paste stability and resistance to segregation during extrusion.

3.2.2. Cement paste preparation

3.2.2.1. Cement ink design

A cement ink with a 100 g cement basis was used with 30 g of water, 0.35 g of Glenium 7700, 0.9 g of VMA 362, and 1.0 g of UW 450. These admixture dosages provided adequate segregation prevention to ensure paste cohesiveness printability based on preliminary testing and were within the manufacturer's recommended dosages for cementitious materials [169-171]. An otherwise identical cement ink with a water-to-cement (w/c) ratio of 0.5 was also used to prepare cast specimens as a comparison to illustrate the effect of a high w/c ratio on the material micromechanical properties. This cement ink design, however, would not be expected to be printable, having insufficient buildability.

The water and admixtures were sonicated using a 500 W probe sonicator (Fisher Scientific Model 505 Sonic Dismembrator, Hampton, NH, USA) operating at 50% power amplitude for 20 seconds to ensure homogenous mixing. The cement ink was mixed using a stainless-steel paddle bit in a mounted brushed DC motor attached to a DC power supply to control the rotation speed. The homogenized water-admixture combination was added to the cement powder and mixed using a stainless-steel paddle bit in a mounted corded drill attached to a DC power supply. The cement ink was mixed for 3 minutes: 1 minute ramping rotation speed up from 200 RPM to 1000 RPM, and 2 minutes at 1000 RPM.

3.2.2.2. Preparation of 3D printed and cast cement pastes

Three 3D printed structures were created using a Hydra 430 gantry model 3D printer with an EMO-XT modular 3D print head (Hyrel 3D, Norcross, GA, USA; Figure 3-1a and b). A cylinder-shaped .STL file with a height and diameter of 2.49 cm was sliced with a 100% rectilinear infill and no perimeter layers, such that all filaments within a given layer were aligned and orthogonal from the previous layer (Figure 3-1c). Each layer was 1 mm high. The mixed cement ink was loaded into the printing head in multiple stages, with tamping being done with a 1.6 mm diameter stainless-steel rod after each stage to mitigate air bubbles. Structures were printed by extruding the cement ink through a half-inch long 14 gauge (inner-diameter 1.6 mm) needle onto a glass substrate. A 25-layer high cylindrical with a *ca.* 2.5 cm diameter and 2.5 cm height was yielded (Figure 3-1b).

Cast specimens (Figure 3-1d) were similarly poured into cylindrical molds with a diameter of 2.5 cm and a height of *ca.* 2.5 cm in multiple stages, with tamping occurring after each stage to mitigate air bubbles. Specimens were cast with two different water cement ratios – 0.3 to mimic the cement ink used for 3D printing and 0.5 to understand the influence of a higher w/c ratio on the material's micromechanical properties.

All specimens were then allowed to cure for a total of 28 days in a curing chamber at 100% relative humidity and room temperature before they were prepared for characterization. Cast specimens were demolded after 24 hours to have exposure conditions closer to that of the 3D printed structures.

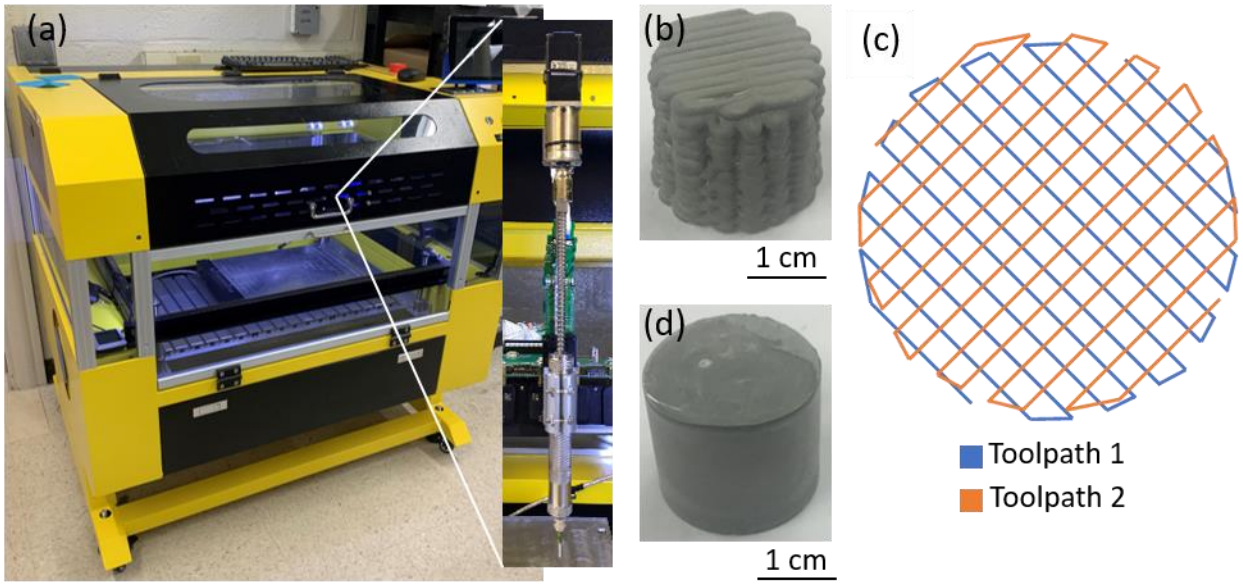

Figure 3-1. (a) Hydra 430 gantry model 3D printer used for printing cement pastes with the modular EMO-XT print head assembly which is mounted inside, (b) a 3D printed cement paste structure with a rectilinear pattern, (c) a diagram of the toolpath used (toolpath 1 and toolpath 2 are orthogonal from each other), and (d) a cast cement paste specimen.

3.2.3. Characterization

3.2.3.1. Sample preparation

The 3D printed structures were cut using a slow-speed diamond saw along the build direction such that the layers alternated between being orthogonal and parallel to the cut face (Figure 3-2a). Cast specimens were cut in a similar manner so that the exposed face was orthogonal to the bottom of the sample. Samples were then epoxy mounted and polished in four steps, first with 320 grit and 600 grit silicon carbide papers, then with 6 µm and 1 µm diamond pastes on a polishing cloth, with ethanol used as a lubricant. Samples were sonicated in ethanol using an FS110D Ultrasonic Cleaner (Fisher Scientific, USA) for five minutes at room temperature between each polishing step to remove polishing residual and prevent cross-contamination of abrasive particles. Polishing with the 1 µm diamond paste continued until the surface was visibly reflective. Surface roughness was measured using the scanning probe microscopy (SPM) capabilities of a Hysitron TI 980 TriboIndenter (Bruker, USA) with a diamond Berkovich tip. SPM images were collected over a 50 µm x 50 µm area, at a setpoint of 2.0 µN. Three roughness measurements were taken near the chosen grid indentation sites, and polishing was considered adequate if the average of the three root-mean-square roughnesses was less than 50 nm. Polishing with the 1 µm diamond paste continued until the roughness condition was met. Surface roughness less than 50 nm has been shown in the literature to be appropriate for nanoindentation on cementitious materials [172].

3.2.3.2. Grid nanoindentation and statistical analysis

Nanoindentation was performed using a Hysitron TI 980 TriboIndenter with a diamond Berkovich tip. Tip area function calibrations were performed using an area function defined from 100 indents on fused quartz, a material with known physical characteristics. Grids of 10 x 100 indents were collected in regions of interest, with a new area function being collected before each grid. A 10 µm spacing was utilized between indents in both the X and Y direction to avoid interference between indentation sites. At each indent location, a trapezoidal load function with a 10 second loading period, a 15 second hold period, and a 10 second unloading period was performed with a maximum load of 2 mN. Fiducial indents were placed at a known distance along the top and bottom edges of each grid using a similar loading function, but with a maximum force of 100 mN, to assist in locating the grid for ESEM/EDS analysis (Figure 3-2b).

Grids were collected at least 2 mm from any sample edge. Grid locations were verified to be placed within filaments rather than across interfilament interfaces using large-area backscattered electron (BSE) ESEM maps. Grid locations were also examined using the TI 980's optical camera to ensure that there were no large voids or significant cracking. Grids were placed near the bottom, middle, and top of the 3D printed structures corresponding to early, intermediate, and late print regions, respectively (Figure 3-2a).

All indentation curves were evaluated visually (Figure 3-2c and d), with abnormal curves (Figure 3-2d) that indicated sample cracking, improper contact between the sample and the tip, or tip slippage at the boundary between two distinct mechanical phases being removed from further analysis. Approximately 15-25% of curves were typically rejected. At each indentation point, the unloading portion of the load vs. displacement curve was analyzed using the Oliver and Pharr Method [173-175] to determine the local hardness and indentation modulus, with the Poisson's ratio of the specimen assumed to be 0.3 [176-178], Poisson's ratio of the diamond indenter probe known to be 0.07, and the modulus of the diamond indenter probe known to be 1140 GPa.

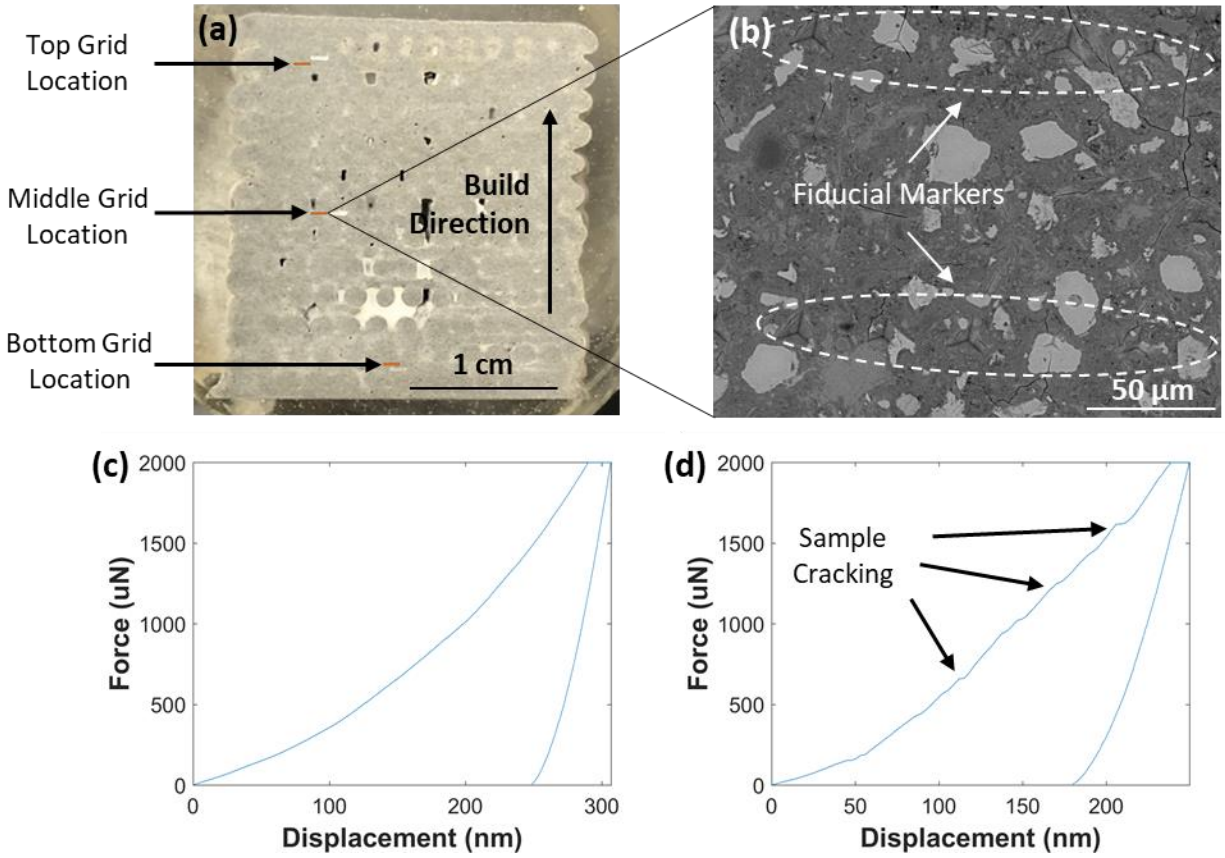

Figure 3-2. (a) Polished 3D printed cement paste, with indentation grid locations denoted, (b) a BSE image of a portion of a grid location, with fiducial markers highlighted, (c) a typical load-displacement curve, (d) a load-displacement curve removed from analysis due to evidence of sample cracking.

The indentation modulus and hardness nanoindentation datasets were initially plotted as normalized histograms to visualize the mechanical property distributions (Figure 3-3a) and generate the experimental probability density functions (PDFs). The datasets were then segmented into mechanically distinct phases by fitting *n* Gaussian distributions to the experimental PDFs using a MATLAB-based multimodal Gaussian fitting algorithm, which coupled an expectation maximization technique with a looping algorithm to allow for multiple trials (Figure 3-3b). The number of characteristic peaks in the experimental PDFs was used to initially set the starting number of Gaussian distributions, *n*. Bin sizes of 1 GPa and 0.1 GPa were used, respectively, for all the Gaussian indentation modulus and hardness fits. These bin

sizes have shown to be appropriate for cement pastes [179-181]. The overall best theoretical PDF for each dataset was selected based on comparison to the respective experimental PDF via the Kullback-Liebler (KL) divergence as well as visual inspection of the agreement between the experimental PDF and theoretical PDF (i.e. appropriate shape and location of the fitted Gaussian distributions). Fits and bin size selection were also verified by determining the coefficient of determination (R^2) value for linear regression between the theoretical and experimental cumulative density functions (CDFs) (Figure 3-3c). R^2 values were typically .997 or greater.

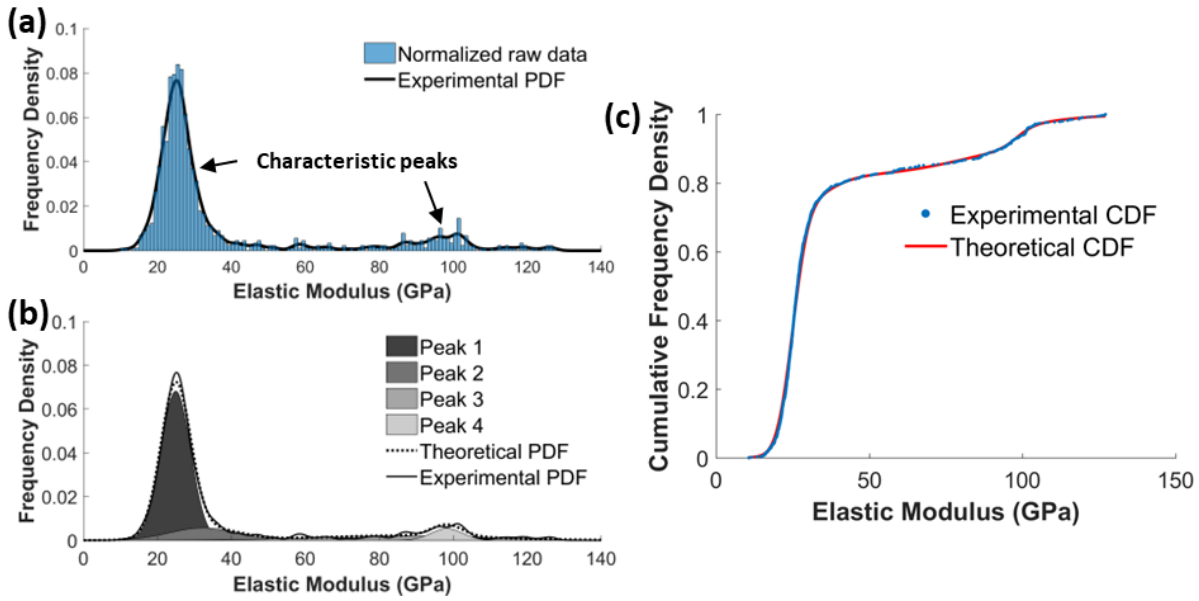

Figure 3-3. (a) Experimental PDF with normalized histogram of raw data for a 3D printed filament, (b) Gaussian deconvoluted distributions with the experimental and theoretical PDFs, and (c) comparison of the experimental cumulative density function (CDF) and theoretical CDF.

3.2.3.3. ESEM and EDS

An FEI Quanta FEG 650 environmental scanning electron microscope (ESEM) (FEI Company, USA) equipped with a Schottky field emission gun and an Oxford Ultim Max 170 energy dispersive X-ray spectrometer (EDS) was used to collect SEM backscattered electron (BSE) images and EDS spectra from the polished samples. An accelerating voltage of 15.0 keV, a spot size of 3.5, a chamber pressure of 130 Pa, and a working distance of 10.5 mm were used. Large-area BSE and EDS maps were collected using a 450x single field of view magnification and an

Oxford software stitching algorithm in order to characterize the chemical elements at each indent location. The EDS maps were averaged over 100 frames using a resolution of 1024, a process time of 5, and a pixel dwell time of 30 µs.

Given that the nanoindentation indents were difficult to visibly identify in the BSE maps, indent locations were approximated by using the location of the highly-visible fiducial indents and the known distance between the fiducial indents and the nanoindentation grid. For both the nanoindentation indents and the fiducial indents, the X and Y coordinates recorded by the TI 980 software were assumed to indicate the center point of the indent. Spatial correlation between microstructural features and micromechanical properties was observed by overlaying indent markers on their corresponding location on the BSE maps and color-coding them based on to which peak they were most likely to belong. Chemical composition at each indent was determined by averaging the EDS chemical composition for a 5x5 pixel square around the center pixel for the calculated indent location, removing pixels determined to be associated with porosity from ImageJ thresholding analysis.

Using the framework defined in [182], all indents identified as being associated with hydrated phases were categorized according to their silicon-to-calcium (Si/Ca) ratio and aluminum-to-calcium (Al/Ca) ratio into five categories: calcium silicate hydrate (C–S–H), mostly C–S–H, mostly calcium hydroxide (CH), CH, and aluminum (Al) Rich. Indents with Si/Ca ratio greater than or equal to 0.4 and Al/Ca ratio less than or equal to 0.16 were classified as C–S–H. Indents with Si/Ca and Al/Ca ratios less than or equal to 0.1 were classified as CH. If the Si/Ca ratio was between 0.1 and 0.4 and the Al/Ca ratio was less than or equal to values interpolated between the CH and C–S–H values, the indent was considered to be a mixture of CH and C–S–H. Such indents with a Si/Ca ratio greater than or equal to 0.25 were considered to be mostly C-S-H, and the others were classified as mostly CH. All other indents were considered to be Al Rich. Based on these classifications, the proportion of indents and median modulus and hardness values for each category was determined for each indentation grid. PDFs of the modulus and hardness values for C–S–H classified indents were created to analyze the effect of the printing process on the mechanical properties of C–S–H.

3.3. Results and Discussion

3.3.1. Influence of the printing process on local indentation modulus and hardness

The sensitivity of the cement ink to the extrusion-based printing process was evidenced by variation in the median indentation moduli between different locations on the same printed structure. In general, lower modulus values were measured towards the bottom and top of the printed structures though no clear correlation in relation to the filament placement during the print progression from bottom to top (i.e., early versus late placement) could be established. All printed structures displayed printed filaments that exhibited median indentation moduli greater than 23 GPa and printed filaments with median indentation moduli less than 20 GPa. The printed filaments with the higher (or lower) median modulus values generally presented also higher (or lower) hardness values though the trend was less pronounced for hardness. The majority of the indents of the higher mechanical property (HMP) filaments had indentation modulus values in the 20-30 GPa range and hardness values in the 1-2 GPa range, while more than 50% of the indents of the lower mechanical property (LMP) filaments had indentation modulus values that were in the 10-20 GPa range and hardness values less than 1 GPa. The ranges of median indentation modulus and hardness values found for the HMP filaments and LMP filaments of the 3D printed structures and for the reference cast cement pastes are provided in Table 3-1. When compared to the cast cement pastes, the HMP filaments exhibited a similar distribution of modulus and hardness values to that of the cast cement pastes with a w/c ratio of 0.3 (reference cast cement paste) (Figure 3-4a and b). In contrast, the LMP filaments had a distribution of indentation modulus values that was shifted to lower modulus values compared to the HMP filaments and the reference cast cement paste. The distribution of modulus values of the LMP filaments more closely mirrored that of the cast cement paste with the higher w/c ratio of 0.5, with a similar quantity of indents in the 10-20 GPa range, suggesting a dynamic change in the local w/c ratio during the printing process (Figure 3-4). A similar trend was seen for the hardness but it was less marked (Figure 3-4). Under extrusion pressure, the bulk cement ink inside the 3D print head was prone to filtration/segregation, resulting in water redistribution and the formation of a watery lubrication layer at the filament-extruder interface, thus causing a dynamically changing w/c ratio of the extruded filaments as the extrusion progressed. Extrusion-induced segregation and drainage have been previously reported in the literature [3, 88, 183]. The

changes in the local w/c ratio of the printed filaments were further attributed to the complex balance between the cement ink sensitivity to drainage and liquid phase filtration during extrusion, the effect of load of subsequent layers on the development of a water film between printed layers of the extruded filaments, and evaporation of the mixing capillary water upon extrusion. The decrease in modulus with an increase in w/c ratio was consistent with the commonly reported effect in the literature of the w/c ratio being inversely related to the cement paste strength [184-186].

Table 3-1. Ranges of median indentation modulus and hardness values for the high and low mechanical property filaments and reference cast cement pastes.

	Median modulus ranges (GPa)	Median hardness ranges (GPa)
HMP filaments[a]	23.1-27.9	1.0-1.2
LMP filaments[b]	13.7-18.8	0.9-1.1
Cast – w/c=0.3[c]	26.7-27.8	0.9-1.1

[a] Ranges based on 6 HMP filaments obtained across 3 printed structures.

[b] Ranges based on 3 LMP filaments obtained across 3 printed structures.

[c] Ranges based on 3 cast replicates.

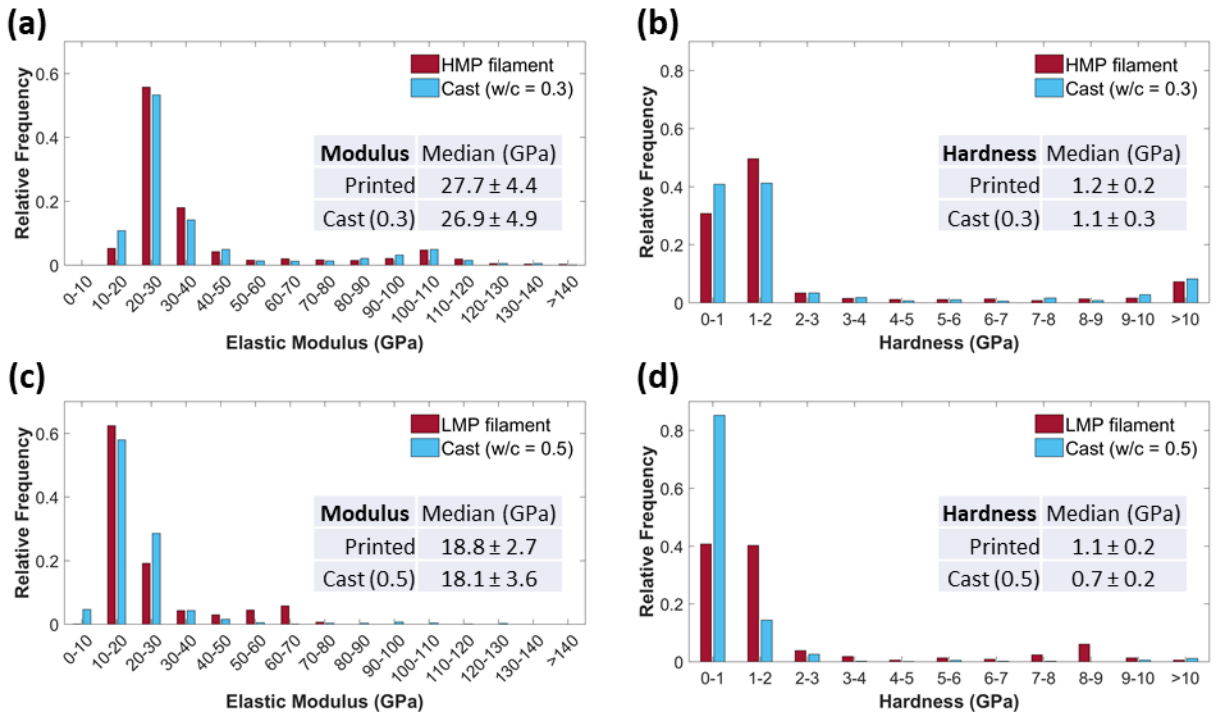

Figure 3-4. Histograms of indentation modulus and hardness distributions of (a), (b) a representative high mechanical property filament (HMP filament) compared to distributions of the reference cast cement paste and (c), (d) a representative low mechanical property filament (LMP filament) compared to distributions of the cast cement paste with a w/c ratio of 0.5.

3.3.2. Mechanically distinct phases from nanoindentation

Segmentation by Gaussian fitting of the nanoindentation data yielded four (4) mechanically distinct phases for the 3D printed filaments and the reference cast cement paste and three (3) mechanically distinct phases for the cast cement paste with the higher w/c ratio of 0.5 (Figure 3-5 and Figure 3-6). The ranges of mean modulus and hardness values of the peaks found for the printed filaments and the reference cast cement paste are provided in Tables A-1 and A-2. For all cases, the majority of indents (more than 55%) were associated with the first mechanically distinct phase (Peak 1), while typically no more than 20% of indents were associated with Peak 2 and the remainder with Peak 3 and/or Peak 4. For clarity, the remaining analysis focuses the presentation of the results and discussion on one representative printed filament of each high and low mechanical properties and cast cement paste specimen of each w/c ratio. All deconvolution

parameters for the representative filaments and cast specimens can be found in Tables A-3 and A-4.

The frequency distribution of the indentation modulus of the representative HMP filament overall mirrored that of the reference cast cement paste, while that of the representative LMP filament exhibited a smaller peak separation, a narrower spread of the distribution, and a greater frequency of Peak 1 modulus values. For the HMP filament, the Peak 1 modulus (E) and hardness (H) values were centered around 25 GPa and 1.1 GPa and spanned 14 – 36 GPa and 0.4 – 2.6 GPa, respectively, similar to the Peak 1 values of the reference cast cement paste. For the LMP filament, the Peak 1 modulus values were lower (E = 10 – 25 GPa) and more comparable to those of the cast cement paste with the higher w/c ratio of 0.5. Contrary to the indentation modulus, the decrease in Peak 1 hardness values seen for the cast cement pastes as the w/c ratio increased from 0.3 to 0.5 was not seen for the printed filaments. These results importantly indicated that the 3D printing process affected the stiffness (modulus) of the mechanically distinct phase associated with Peak 1 but not its resistance to local plastic deformation (hardness). Furthermore, the mean modulus values of Peak 1 were similar to the respective median modulus values of the printed filaments, suggesting that the mechanically distinct phase associated with Peak 1 likely controlled the overall mechanical response of the extruded filaments.

Remarkably, the shape of the frequency distribution of Peak 1 of the printed filaments and cast cement pastes was unimodal, and, from purely mechanical evidence and previous literature [180, 181, 187-192], the phases associated with Peak 1 seem to resemble chemical phases corresponding primarily to low density hydration products. The addition of viscosity modifying admixtures (VMA) to cement pastes has been shown to have a significant impact on the hydration process of Portland cement and to change the shape of the modulus frequency distribution of the main hydrated phases from bimodal frequency distributions that are characteristic of two distinct types of the main hydrate phase calcium-silicate-hydrate (C–S–H), to having a single, larger peak associated with a much greater proportion of hydrated products [193, 194]. This observation shows that the presence of VMA and anti-washout admixtures that are necessary to obtain a printable cement ink can impact the distribution and micromechanical properties of the hydrated phases.

Peak 2 modulus values displayed a larger spread and corresponded to a much lower fraction of indents compared to Peak 1. The range of Peak 2 modulus values had a similar direction shift in modulus between the HMP filament and LMP filament as Peak 1 (i.e., decrease for the LMP filament). The HMP filament showed similar average modulus values for Peak 2 as the reference cast cement paste ($E = 36.7 \pm 7.6$ GPa and $E = 38.5 \pm 8.8$ GPa, respectively), while the LMP filament showed a much lower average value ($E = 26.3 \pm 5.9$ GPa). The Peak 2 modulus values for the LMP filament were similar to what was seen for Peak 2 in the cast cement paste with the higher w/c ratio of 0.5 ($E = 26.3 \pm 5.9$ GPa and $E = 26.3 \pm 9.0$ GPa, respectively), further suggesting that the dynamic changes in local w/c ratio during the printing process contributed to shifts in local modulus properties of the printed filaments. However, similarly to Peak 1, there was no difference in the Peak 2 hardness values between the printed filaments and the reference cast cement paste.

The effect of the extrusion-based printing process was further seen from the mechanically distinct phases associated with Peaks 3 and 4. Peaks 3 and 4 of the printed filaments tended to show more dramatic shifts when compared to Peaks 3 and 4 of the reference cast cement paste or the cast cement paste with a w/c ratio of 0.5, suggesting a likely effect of the extrusion-based process on unhydrated particle dissolution and phase assemblage. Furthermore, Peak 4 (seen in the HMP filament and LMP filament as well as the reference cast cement paste) corresponded to a range of high-modulus indents (100 – 114 GPa for the HMP filament, 58 – 66 GPa for the LMP filament, and 101 – 109 GPa for the reference cast cement paste) that was not present in the cast cement paste with a w/c ratio of 0.5. Contrary to Peak 1, the shifts in indentation modulus of Peaks 3 and 4 for the printed filaments were matched by shifts in hardness. These results indicated that the 3D printing process affected both the stiffness and the resistance to local plastic deformation of the mechanically distinct phases associated with Peaks 3 and 4. Overall, the LMP filament exhibited a lower frequency of indents associated with Peaks 3 and 4 (14.8%) compared to the HMP filament (18.6%), indicating a more advanced cement hydration stage for the LMP filament. These results were consistent with changes in local water availability during the extrusion-based printing process, which was thought to affect the local w/c ratio during the hydration process.

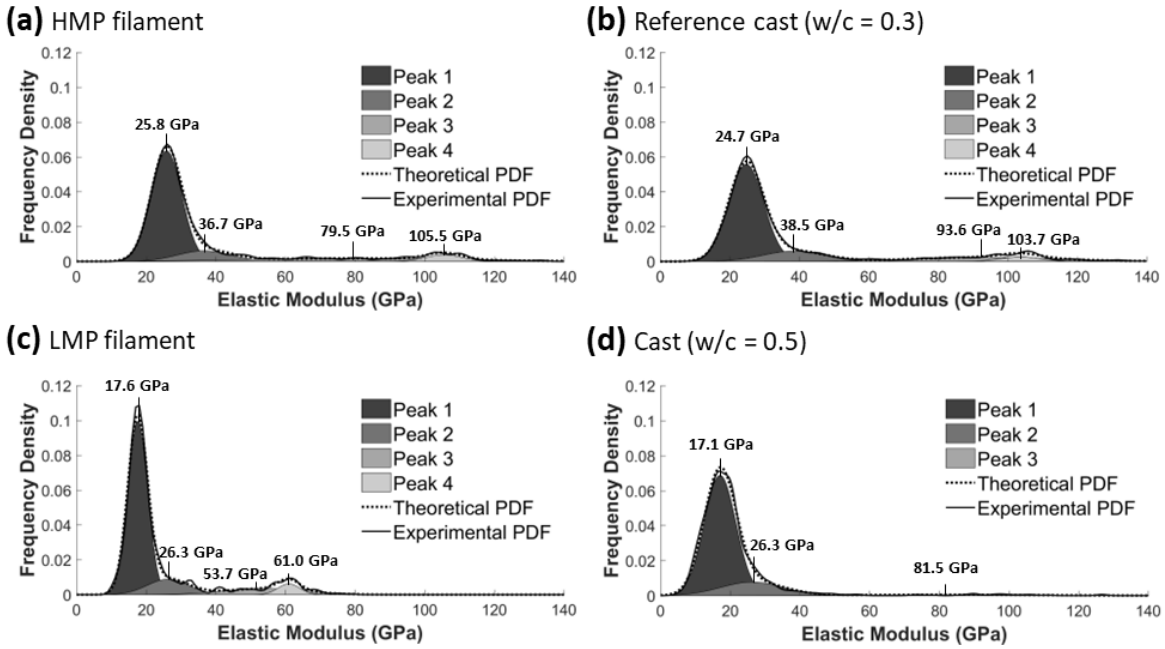

Figure 3-5. Gaussian deconvolution for indentation modulus of representative 3D printed filaments and cast cement paste specimens. (a) High mechanical property filament (HMP filament), (b) reference cast cement paste, (c) low mechanical property filament (LMP filament), and (d) cast cement paste with a w/c ratio of 0.5.

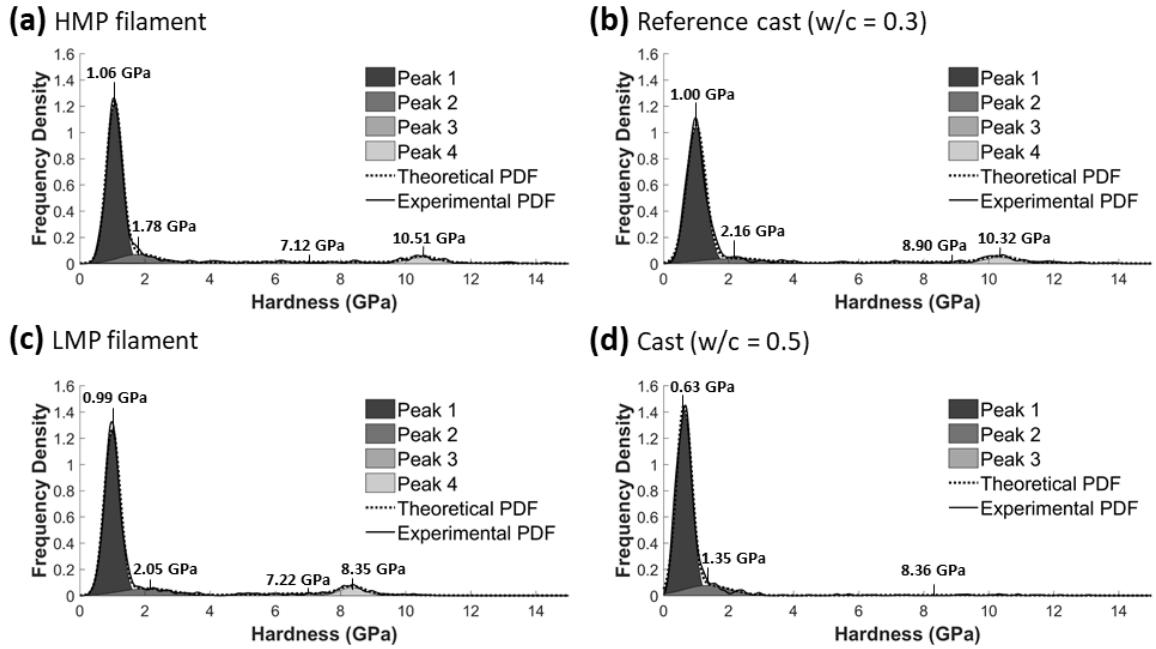

Figure 3-6. Gaussian deconvolution for indentation hardness of representative 3D printed filaments and cast cement paste specimens. (a) High mechanical property filament (HMP filament), (b) reference cast cement paste with a w/c ratio of 0.3, (c) low mechanical property filament (LMP filament), and (d) cast cement paste with a w/c ratio of 0.5.

3.3.3. Correlation of mechanical information with spatial morphology and chemical information

3.3.3.1. Mechanically distinct phases and microstructural features

Overall, a good correspondence between micromechanical properties and microstructural features was confirmed via color-coding of indent locations overlaid on large-area backscattered electrons (BSE) maps of grid areas (Figure 3-7). Indents associated with Peak 1 (green markers in Figure 3-7) were nearly all located within the hydrated portion of the microstructure (dark grey features). Indents associated with Peak 2 (blue markers) were primarily in hydrated areas that can be expected to have higher mechanical properties (i.e., crystalline hydrates, intermixed solids, hydrates on or near the boundaries of unhydrated cement particles, or within unusual features indicative of less common hydration products). Indents associated with Peaks 3 and 4 (yellow and magenta markers, respectively) were found to be located within the brightest phases of the BSE images, which are typically associated with unhydrated cement particles in cement

paste microstructure. Indents associated with Peak 3 (lower average indentation modulus and higher standard deviation compared to Peak 4) were generally found near the edge of the brightest phases or within areas of the brightest phases that showed similarity with the local morphology surrounding that phase. Indents associated with Peak 4 (higher average indentation modulus and lower standard deviation compared to Peak 3) were typically located within the core of the brightest phases and away from their edges and or within edge areas that showed morphological differences with the local morphology surrounding that phase. Based on this spatial correlation of indent location with morphology observations from ESEM and known chemical phases from the literature for cementitious materials [176, 180, 181, 187-192, 195-207], the mechanically distinct phases identified from Gaussian deconvolution of the nanoindentation data could be associated with the following general chemical phases: *Peak 1* – main cement hydration products [i.e., C–S–H, mixtures of C–S–H and calcium hydroxide (CH), CH, and hydrated calcium sulfoaluminate phases (e.g., ettringite)]; *Peak 2* – high stiffness hydration products and hydration products on or near boundaries of unhydrated cement particles; and, *Peaks 3 and 4* – unhydrated cement particles.

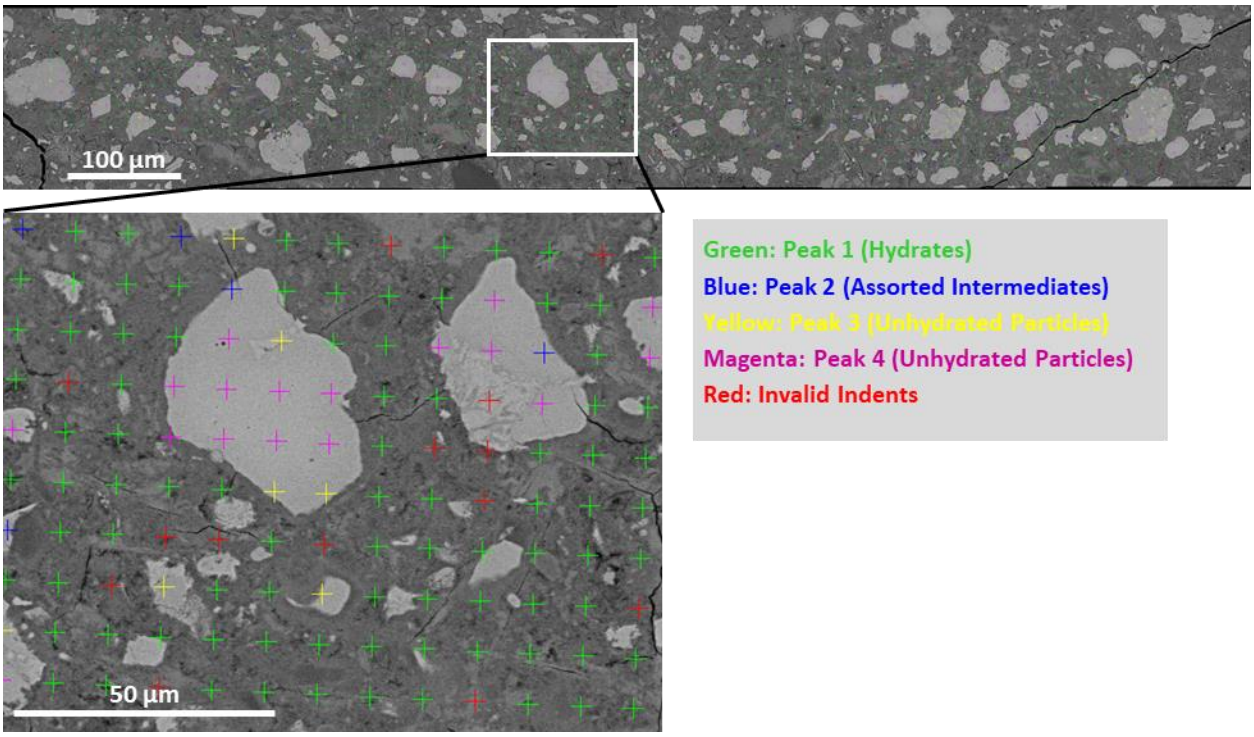

Figure 3-7. Example of a large-area backscattered electron (BSE) map with color-coded markers overlaid on indent locations.

3.3.3.2. Coupling nanoindentation and chemical information from ESEM/EDS

The effect of extrusion during printing on hydrate phase assemblage was revealed by segmenting the EDS data as a function of elemental ratios such that the chemical signature of the 3D printed and cast indents could be compared (Figure 3-8 and Table 3-2). For this analysis, indents associated with Peak 1 and those associated with Peak 2 identified as being in the hydrated portion of the microstructure were considered. The coupling of nanoindentation and chemical information showed that the local indentation response was predominantly the result of a multi-phase response rather than that of pure phases. A majority of the hydrate indents of the 3D printed filaments and cast cement pastes (more than 70%) exhibited a chemical composition that corresponded to mixtures of C–S–H and CH (mostly C–S–H or mostly CH), indicating a probable formation of microcomposites of CH and C–S–H of varying microstructural arrangements.

Notably, the ranges of indentation modulus values of the hydrate phases did not show, overall, major differences between each morphological category (Table 3-3) and were in particular anomalously lower for CH than reported in the literature (M = 36-49 GPa for pure CH as reported from nanoindentation [190, 195, 208-210]). Similarly, the indentation modulus of the C–S–H/CH mixtures did not appear to be enhanced by CH when compared to pure C–S–H. These results suggested an effect of the pore structure and microstructural arrangement of the phases on the mechanical properties of the hydrate phases. It also suggested that the adsorption of the printability admixtures on the surface of the hydrate phases had an effect on their mechanical response. The use of VMA has been reported to cause anomalous dispersion of hydration products and CH to grow preferentially in void walls [193, 211, 212]. The low modulus values found for indents identified as CH in the printed filaments and cast cement pastes were thought to be the result of growth of CH in less confined space and nanoindentation on porous assemblages of CH rather than on large CH crystals, thus reflecting the pore structure effect. Representative porous assemblages of CH can be seen in Figure 3-9 for the 3D printed filaments and the reference cast cement paste along with a significant number of indent failures due to the presence of porosity and edge effects. The effect of porosity on CH assemblages and C–S–H/CH mixtures on the modulus has been reported in [213] and showed a significant

decrease in modulus value with an increase in porosity. It has also been reported in the literature that the presence of pores highly influences the response obtained from nanoindentation tests [214]. The nanoindentation results reflected the mechanical properties of porous mixed phases (i.e., CH mix and C–S–H/CH mixtures) and the presence of porosity.

Furthermore, the 3D printed filaments had an overall greater percentage of C–S–H/CH indents compared to both cast cement pastes (81-83% vs. 76-78%, respectively). It was believed that the greater formation of C–S–H/CH mixtures in the 3D printed filaments did not result from the dynamic change in the local w/c ratio alone but rather was favored by an effect of the extrusion shear forces (developed during the progressive forcing of the cement ink through the extrusion nozzle) on the dissolution of the unhydrated cement particles. The effect of the extrusion process on hydrated phase formation was further seen from the proportion of indents of Peak 1 having an elemental composition corresponding to Aluminum (Al)-rich phases, with a lower percentage for the 3D printed filaments compared to the cast cement pastes. The effect was more pronounced for the HMP filament, which was thought to have a lower local w/c ratio, with only 5.4% Al-rich indents compared to 12.4% for the reference cast cement paste and 9.9% for the cast cement paste with a w/c ratio of 0.5 (Table 3-2). The extrusion shear forces were thought to selectively drive an increased dissolution of the regions of unhydrated particles that were rich in calcium (Ca) and silicon (Si) and poor in Al, thus resulting in less Al being present in the hydrated microstructure and reducing the proportion of indents associated with Al-rich phases compared to the cast cement pastes. The effect of the extrusion process on phase assemblage was also noticeable from the fractions of indents identified as pure C–S–H relative to the fractions of indents identified as pure CH (Table 3-2). For the 3D printed filaments, the proportion of pure C–S–H and pure CH were found to be similar while the cast cement pastes showed different proportions consistent with the w/c ratio (i.e., the lower the w/c ratio, the higher content of C–S–H phases and the lower content of CH [184]).

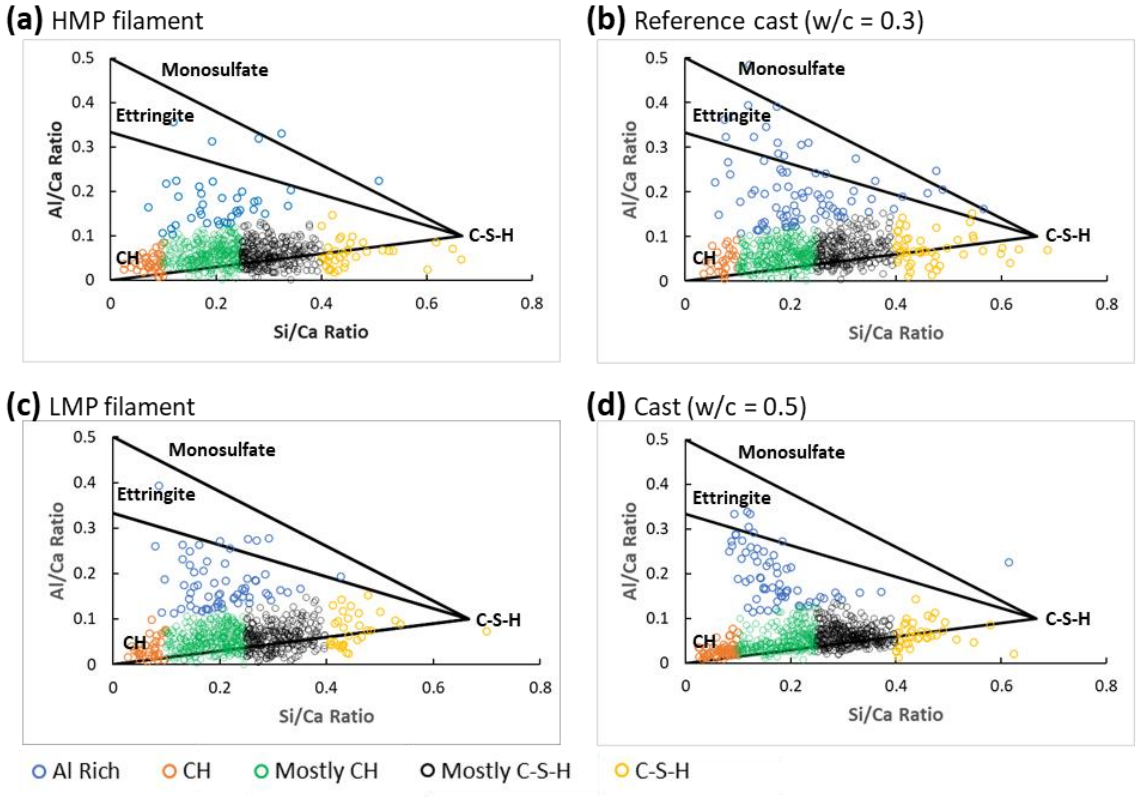

Figure 3-8. Distributions of Al/Ca ratio vs. Si/Ca ratio of hydrates for representative 3D printed filaments and cast cement paste specimens. (a) HMP filament, (b) reference cast cement paste with a w/c ratio of 0.3, (c) LMP filament, and (d) cast cement paste with a w/c ratio of 0.5. Indents are color-coded into categories of hydrates according to the framework described in [182]. Theoretical values for C–S–H, CH, ettringite, and monosulfate are shown.

Table 3-2. Percentage of hydrate indents in each morphological phase category determined from statistical deconvolution analysis of representative 3D printed filaments and cast cement paste specimens with w/c ratios of 0.3 (reference) and 0.5.

	C–S–H	C–S–H/CH mixtures		CH	Al-rich phases
		Mostly C–S–H[a]	Mostly CH[b]		
HMP filament	5.3%	39.7%	44.1%	5.4%	5.4%
LMP filament	4.8%	36.7%	44.4%	4.9%	9.1%
Cast – w/c=0.3	7.4%	36.2%	40.2%	3.8%	12.4%

Cast – w/c=0.5	4.9%	44.1%	33.5%	8.1%	9.5%

[a] C–S–H with a low percent of CH (CH poor C–S–H)

[b] C–S–H with high percent of CH (CH-rich C–S–H)

Table 3-3. Median modulus values ± MAD (in GPa) of hydrate indents in each morphological category of representative HMP filament and LMP filament compared to the cast cement pastes with w/c ratios of 0.3 (reference) and 0.5.

	C–S–H	C–S–H/CH mixtures		CH	Al-rich phases
		Mostly C–S–H[1]	Mostly CH[2]		
HMP filament	26.6 ± 2.2	26.7 ± 2.8	26.0 ± 3.0	30.9 ± 5.1	27.1 ± 4.4
LMP filament	17.9 ± 1.4	17.9 ± 1.7	17.7 ± 2.0	19.4 ± 1.6	18.2 ± 1.8
Cast – w/c=0.3	26.6 ± 5.0	25.4 ± 3.1	24.9 ± 3.3	25.9 ± 3.9	25.3 ± 3.0
Cast – w/c=0.5	18.4 ± 5.0	16.9 ± 3.3	18.1 ± 3.0	19.5 ± 3.3	17.7 ± 3.9

[1] C–S–H with a low percent of CH (CH poor C–S–H)

[2] C–S–H with high percent of CH (CH-rich C–S–H)

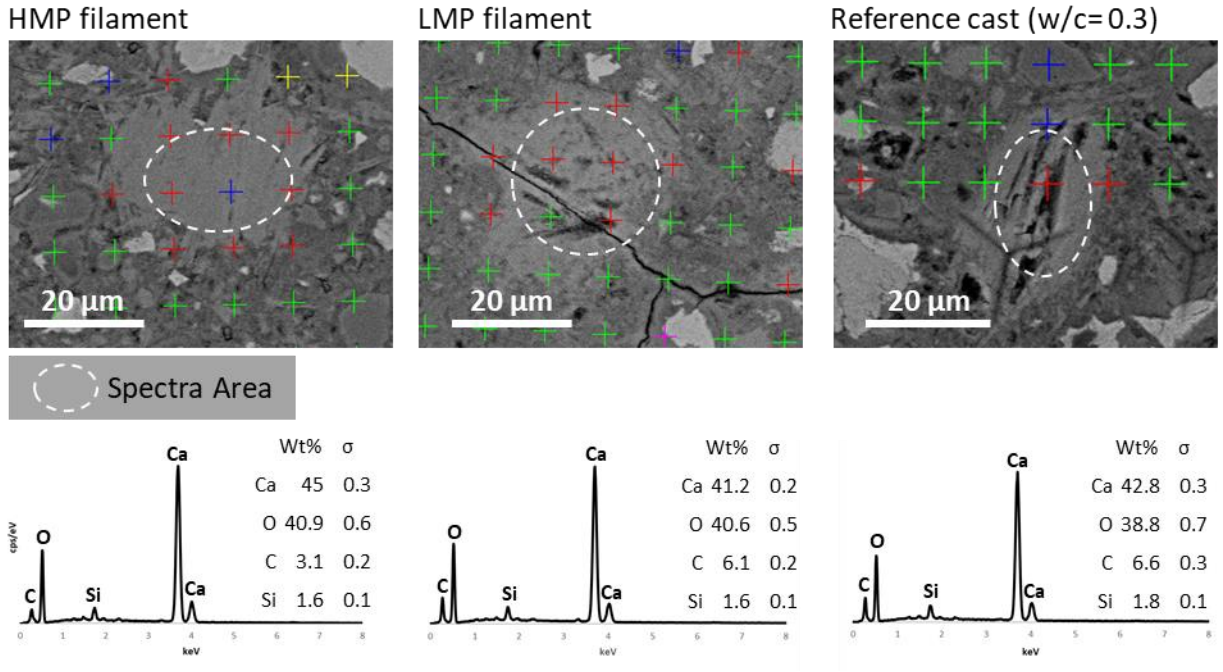

Figure 3-9. Backscattered electron (BSE) images and energy-dispersive X-ray spectroscopy (EDS) spectra showing porous assemblages of calcium hydroxide (CH) and preferential indent

failure (red crosses) in representative 3D printed filaments and reference cast cement paste (with visible marking fiducial).

ESEM/EDS analysis of the indents associated with Peaks 3 and 4 provided additional insight into the evolution of the unhydrated cement particles and corresponding formation of C–S–H/CH mixtures and Al-rich phases during the extrusion process. These indents were found to have a chemical composition that was either high in Ca and Si and without significant Al and Fe, or a chemical composition that was rich in Al and Fe. Figure 3-10 shows representative unhydrated cement particles with and without inclusions rich in Al and Fe for the 3D printed filaments and the reference cast cement paste. The inclusions had a much higher Al and Fe content (8-10 wt% for each element) compared to the remainder of the unhydrated cement particle and the unhydrated cement particles with no inclusions (less than 1 wt% of each element). Indent locations on portions of unhydrated cement particles with high Al and Fe (Al + Fe concentration > 15 wt%) were generally found to have higher indentation modulus values than those without, indicating that the inclusions had higher local mechanical properties than other areas of the unhydrated cement particles.

While the dynamic change in local w/c ratio in the 3D printed filaments could explain changes in the level of hydration of the unhydrated cement particles, it did not fully explain the downward shift in Peak 3 modulus and hardness values for the HMP filament relative to the reference cast cement paste, nor the LMP filament having Peak 3 and 4 indentation modulus and hardness values below the Peak 3 values of the cast cement paste with a w/c ratio of 0.5. The reduction in Peak 3 indentation modulus and hardness values of the HMP filament and LMP filament compared to the reference cast cement paste suggested that the extrusion process selectively drove hydration on the regions of the unhydrated particle with lower mechanical properties (i.e., regions near edges and without high Al and Fe content). The reduction in indentation modulus and hardness values was further extended to Peak 4 for the LMP filament, suggesting a further dissolution of the unhydrated cement particles that impacted the whole particle as a result of a higher local w/c ratio. In contrast, only localized regions of the unhydrated cement particles for the HMP filament that were exposed to less water seemed to be affected, primarily through a

shift in Peak 3. Consistent with a greater w/c ratio and increased hydration, the LMP filament exhibited overall a lower surface coverage of unhydrated cement particles though to a lesser degree than for the cast cement paste with a w/c ratio of 0.5. The changes in the mechanical response of the unhydrated cement particles in the 3D printed filaments further pointed towards an effect of the extrusion shear forces on the hydration process. It has been previously reported in the literature that stress applied on fresh cement paste, such as that applied during extrusion, can significantly impact hydration and reaction kinetics between solids and liquids and lead to enhanced dissolution and accelerated hydration of unhydrated cement particles [215, 216].

Remarkably, while the LMP filament and HMP filament exhibited a similar fraction of indents comprised of C–S–H and C–S–H/CH mixtures, the LMP filament presented indentation modulus values that were significantly lower than those of the HMP filament. This marked downward shift in terms of modulus values, which was also seen for the cast cement paste with a w/c ratio of 0.5, pointed toward an effect of the microstructure (i.e., porosity) and different microstructural arrangements of the C–S–H and C–S–H/CH mixtures. These hydrates were thought to be more loosely packed and interspersed with a higher porosity in the LMP filament than in the HMP filament as a result of a higher, extrusion-induced, local w/c ratio that provided more space available in the interstices between the cement grains during hydration. It was also thought that the extrusion process might have altered the C–S–H phase distribution. The mesostructure (around 100 nm) of C–S–H phases have been reported to play a significant role in determining cement paste properties [195, 205, 217-219]. The C–S–H phases found in the LMP filament exhibited overall a similar range of Si/Ca ratios (Figure 3-8) but lower modulus values than the C–S–H phases of the HMP filament (Si/Ca ratios ranging from ca. 0.4 – 0.6 and ca. 0.4 – 0.7 and median modulus values of 17.9 ± 1.4 GPa versus 26.6 ± 2.2 GPa). This observation could indicate an effect of the extrusion process on the C–S–H phase packing density and their intrinsic mechanical characteristics. Differing elastic moduli of C–S–H for similar mineralogical composition have been attributed in the literature to changes in porosity and packing densities, with the higher the packing density, the higher the elastic modulus of the C–S–H mesoscale aggregations [195, 205, 217, 218, 220, 221].

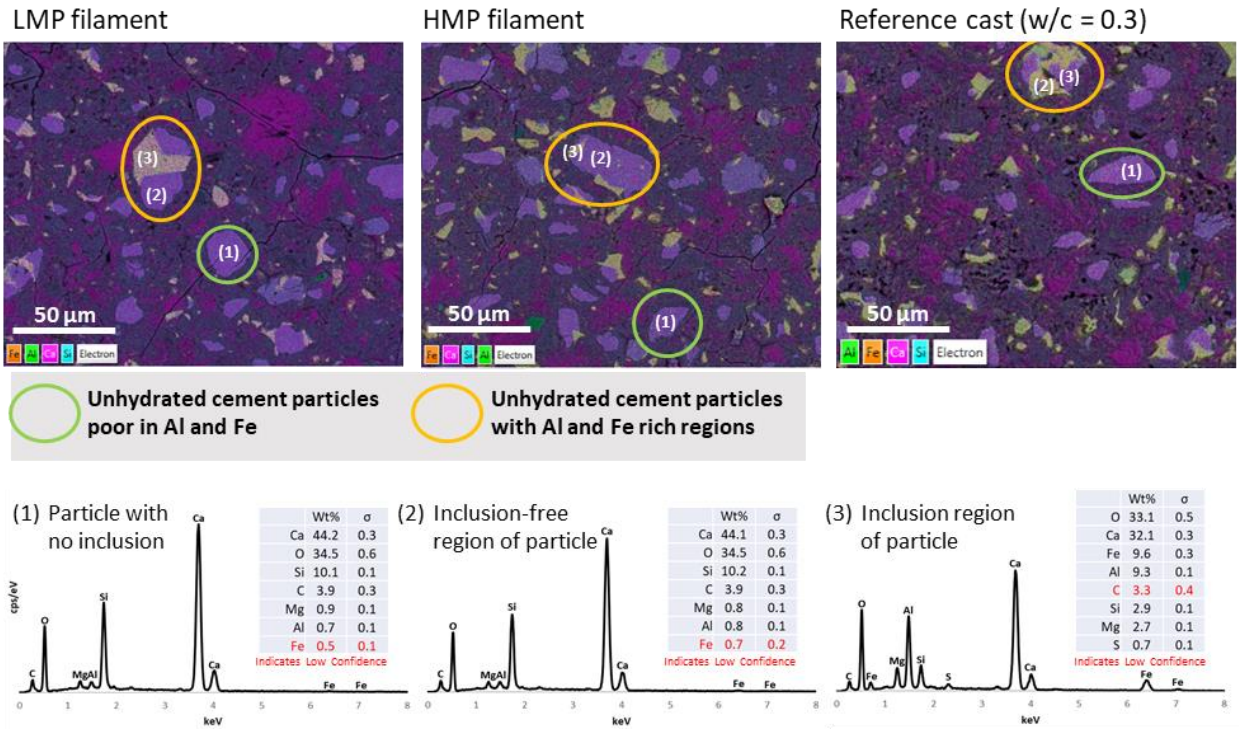

Figure 3-10. Layered EDS maps highlighting unhydrated cement particles with and without inclusions rich in Al and Fe in representative low mechanical property filament (LMP filament), high mechanical property filament (HMP filament) and the reference cast cement paste. Numbering indicates representative spectra of unhydrated particles and region of unhydrated particles with and without Al and Fe rich inclusions.

3.3.4. Effect of 3D printing on C-S-H phase distribution

Further refinement of the EDS segmentation and examination of the indents only identified as C–S–H provided additional insight into the effect of the extrusion-based printing process on the distribution of C–S–H products and the dependency of the mechanical properties of the 3D printed filaments on the C–S–H morphology and packing density. This was accomplished by plotting the PDFs of indentation modulus (Figure 3-11) and hardness (Figure 3-12) values for indents identified as C–S–H. In this analysis, all the mixed phases, CH, and all other minor phases were carefully excluded so that the data refer only to the C–S–H phases. The PDFs of the C–S–H phases were then color-coded according to the ranges of elastic modulus values

corresponding to the mechanical signatures of high-density (HD) C–S–H (28-37 GPa), low-density (LD) C–S–H (15-28 GPa), and loosely-packed (LP) C–S–H (less than 15 GPa) as reported in the literature for w/c ratios ranging from 0.3 to 0.5 [180, 181, 187-192]. These C–S–H phases have been shown to be morphologically similar but structurally distinct and to be related to their packing density [195, 205, 217, 218, 220]. It is generally accepted that C–S–H is made-up of small building blocks described as globules, particles, disks, and/or foils that are arranged in a disordered fashion for LD C–S–H (average packing density of 0.64) and in a closely packed order for HD C–S–H (average packing density of 0.75) [195, 205, 217-219, 222-224]. The packing density of LD C–S–H and HD C–S–H are principally the result of continuum distributions of local densities that compose the cement matrix. In the present study, the ranges of modulus values of the C–S–H phases of the printed filaments and cast cement pastes overlapped with those of the mixtures of CH and C–S–H and other hydrated phases, suggesting that the mechanical properties of the C–S–H phases were likely influenced by the pore structure and microstructural arrangement of the surrounding mixed phases.

Distinctive shifts in the distributions of the indentation moduli of the C–S–H phases (Figure 3-11) were seen between the HMP filament and LMP filament and compared to the cast cement pastes. The shifts in the PDF peaks corresponded to changes in the relative fractions of LP, LD, and HD C–S–H. Based on the mechanical signatures, the C–S–H phases in the HMP filament were identified as a mix of LD and HD C–S–H while the C–S–H phases in the LMP filament were identified as primarily low-density phases (LP + LD C–S–H), which was consistent with an increase in the local w/c ratio induced by the extrusion process. For the HMP filament, the relative fractions of LD and HD C–S–H were slightly increased at the expense of the relative fraction of the LP C–S–H that completely disappeared. These results suggested that the extrusion-based printing process favored an increase in packing density of the C–S–H, thus making the C–S–H phases stiffer. For the LMP filament, the relative fraction of LD C–S–H was significantly increased from *ca*. 62% (reference cast) to *ca*. 96% and was accompanied by the complete disappearance of HD C–S–H. In comparison, the relative fractions of LP C–S–H and LD C–S–H in the cast cement paste with a w/c ratio of 0.5 were *ca*. 33% and *ca*. 63%, respectively. Grid nanoindentation results reported in the literature show that as the w/c ratio increases, more low-density phases (LP + LD C–S–H) are found and that the porosity increases [205, 219, 225]. The greater formation of LD C–S–H in the LMP filament could not, however,

solely be explained by an increase in the local w/c ratio. Rather, the preferential formation of LD C–S–H and significant reduction in LP C–S–H in the LMP filament indicated an effect of the extrusion forces on the C–S–H packing density and porosity, which was facilitated by the water lubrication layer. The shapes of the PDFs were significantly more compressed for the 3D printed filaments compared to those for the cast cement pastes, particularly for the LMP filament. The 3D printed filaments presented a narrow peak while the cast cement pastes tended to have a broader peak. These observations taken with the fact that LD C–S–H accounts for most of the C–S–H phases of the printed filaments suggested that 3D printing promoted less variation in the local packing fractions and thus a more uniform distribution of modulus values of LD C–S–H compared to traditional casting. It was further thought that the extrusion pressure combined with the formation of small diameter filaments favored the mesoscale assembly and aggregation of more oblate C–S–H platelets (high aspect ratio disks) whose largest face tended to align along the print path. The effect of water and pressure on the preferential orientation of calcium aluminosilicate hydrate compacts and the effect on the modulus and hardness have recently been reported in the literature [226]. The mesoscale assemblage of oblate platelets has been shown to lead to a lower packing density than that of disks and to increase the fraction of pores formed at the scale of around 100 nm [219]. It has also been reported that an increase in w/c ratio increases the aspect ratio of the C–S–H platelets, thus increasing the mesopores and lowering the packing density. This trend supports the idea of mesoscale aggregation of higher aspect ratio C–S–H platelets in the LMP filament, resulting in more low-density phases and therefore lower indentation modulus C–S–H than in the HMP filament.

These findings were further supported by the frequency distributions of the C–S–H hardness. Notably, no significant shift in the primary peak of the hardness frequency distributions of C–S–H was observed between the HMP filament and the LMP filament despite the significant difference in their fractions of LD and HD C–S–H and ranges of modulus values. Contrary to the modulus, the hardness of the C–S–H appeared to be insensitive to the dynamic changes in local w/c ratio during the printing process. The C–S–H hardness values of the printed filaments were all centered around 1 GPa and ranged from 0.5 to 1.5 GPa. This range of hardness values was consistent with previous studies [196, 205, 209, 218, 227-229] and corresponded to the presence of both low- and high-density phases. In comparison, the cast cement pastes exhibited a softening of the C–S–H (i.e., decrease in hardness) with an increase in the w/c ratio from 0.3 to

0.5 that was also consistent with the changes in the relative proportion of LD and HD C–S–H. The C–S–H hardness response in the 3D printed filaments reflected the reduction in LP C–S–H and pointed toward the development of oriented mesoscale aggregation of C–S–H during the extrusion-based 3D printing process of small diameter filaments rather than the more randomly oriented C–S–H aggregation as in the cast cement pastes. A proposed schematic representation of the development of oriented mesoscale aggregation of oblate C–S–H platelets during the extrusion-based printing process of small diameter filaments is provided in Figure 3-13. It is also clear from the modulus and hardness results and their comparison between the printed filaments and cast cement pastes that the form of packing arrangement of the C–S–H phases at the mesoscale is the predominant factor of their micromechanical response. Alignment of the mesoscale aggregation of the hydrate phases along the print path suggested also potential anisotropy of the micromechanical properties within the printed filaments (parallel versus orthogonal to the print path) and requires further investigations.

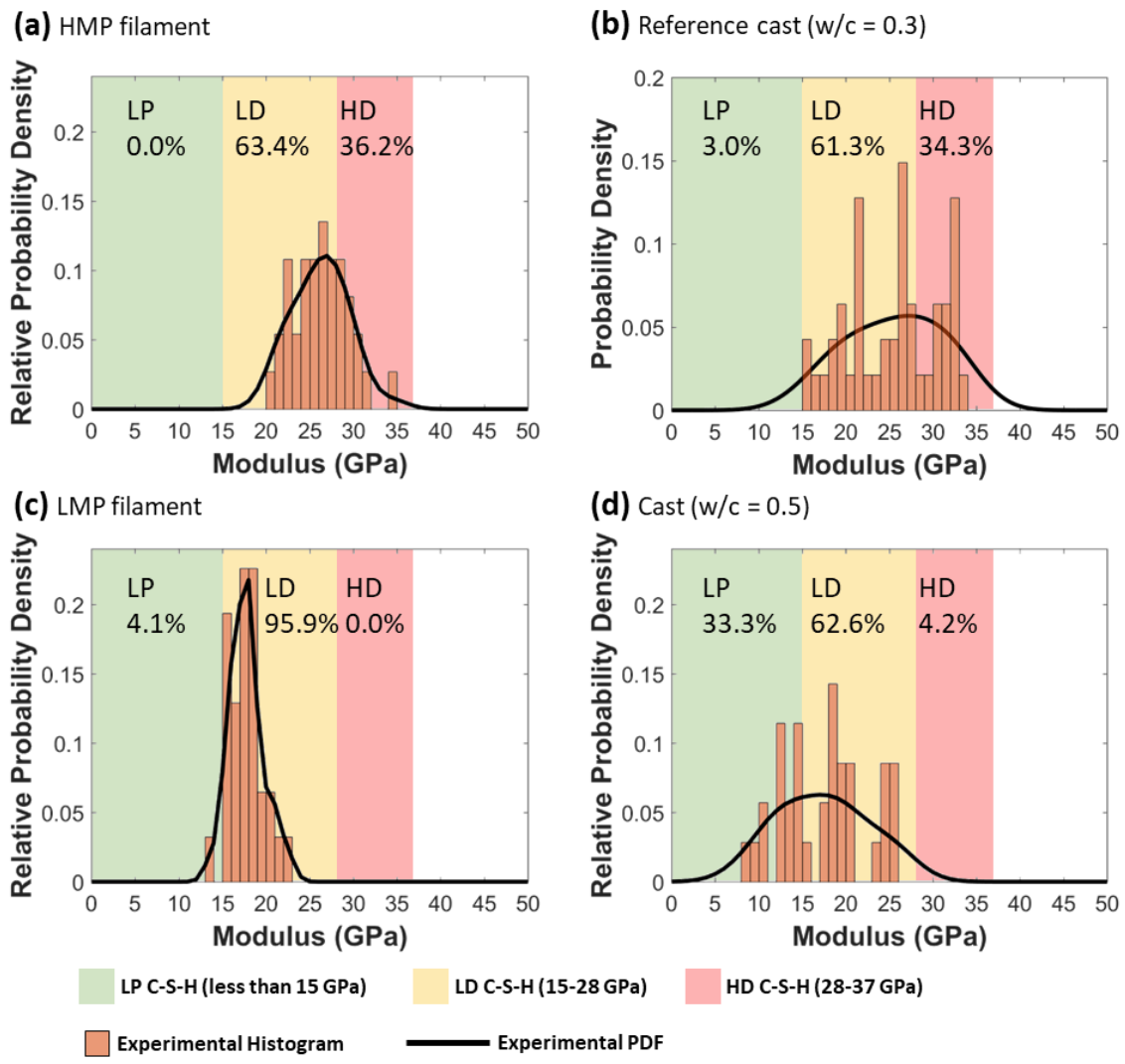

Figure 3-11. Modulus PDFs for indents categorized as "pure" C–S–H based on EDS and nanoindentation data of representative 3D printed filaments and cast cement paste specimens. Modulus ranges for C–S–H categories are based on typical values reported in the literature for loosely packed (LP), low-density (LD), and high-density (HD) C–S–H.

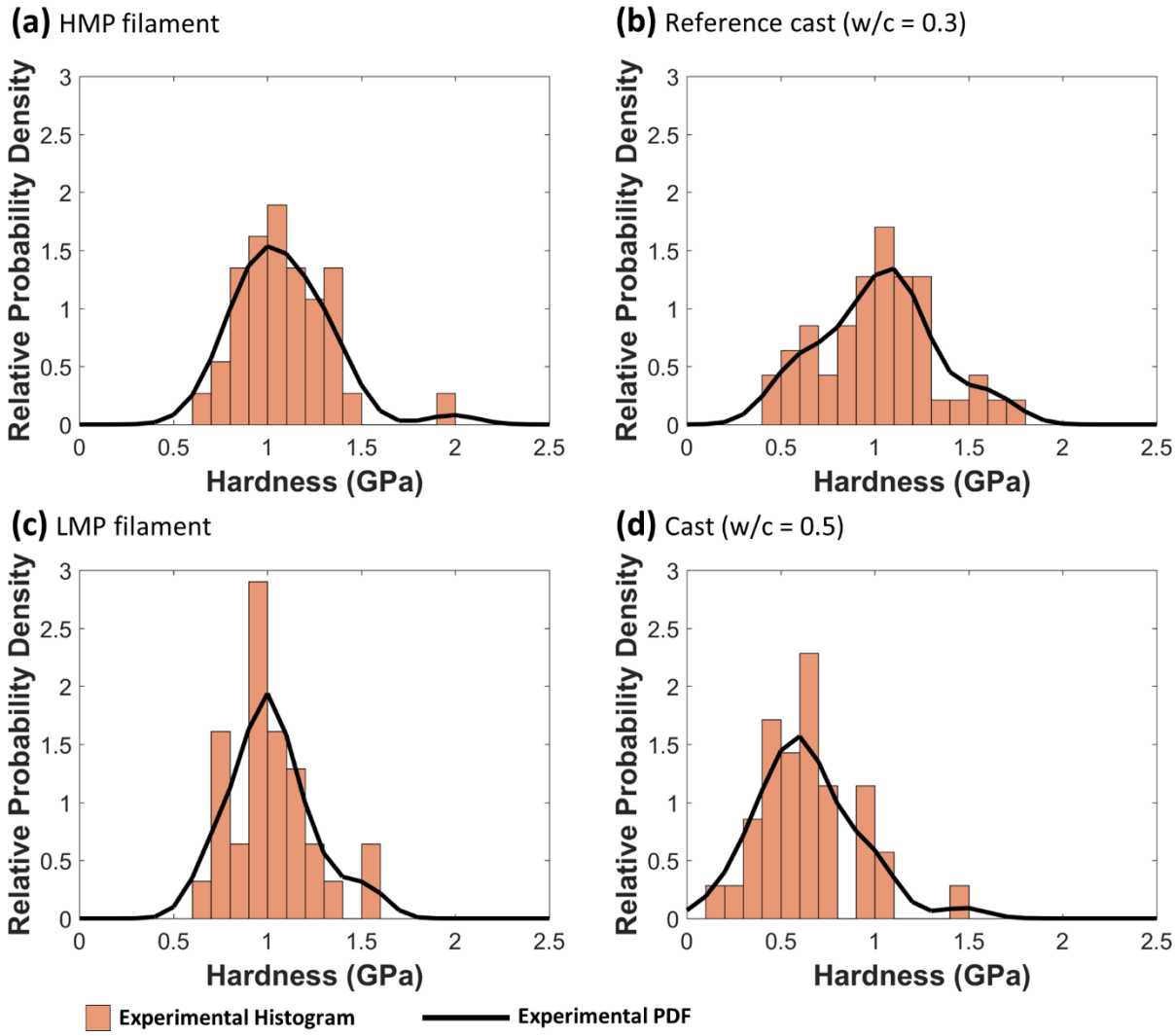

Figure 3-12. Hardness PDFs for indents categorized as “pure” C–S–H based on EDS and nanoindentation data of representative 3D printed filaments and cast cement paste specimens.

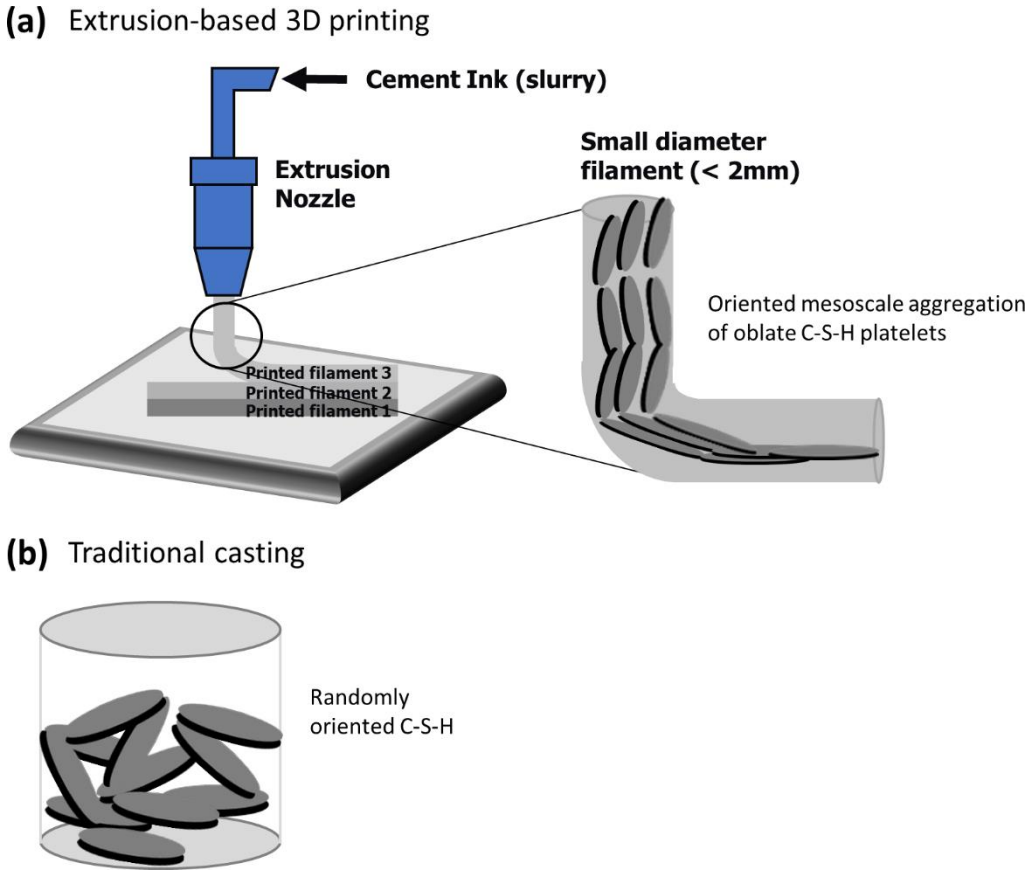

Figure 3-13. Schematic representation of (a) the development of oriented mesoscale aggregation of oblate C–S–H platelets during extrusion-based 3D printing of small diameter filaments and (b) randomly oriented C–S–H aggregation in traditional casting.

3.4. Conclusions

The micromechanical properties (indentation elastic modulus and hardness) of extruded filaments in 3D printed cement paste structures were studied using grid nanoindentation and correlated with microstructural observations and chemical analysis at each indent location. Based on the presented results, the following conclusions can be drawn:

- Dynamic changes in the local w/c ratio during the extrusion process combined with stress-induced dissolution of cement particles affected the hydrate phase assemblages and micromechanical properties of the printed filaments.

- The blend of chemical admixtures (VMA, UW, and high-range water reducer) used to ensure printability of the cement ink influenced the distribution of the primary hydrated phases and resulted in an anomalous overlap of their micromechanical properties.
- The extrusion of small diameter filaments affected the mesoscale assemblage and local packing of the C–S–H phases and might have favored the mesoscale aggregation of oblate C–S–H platelets.
- It is suggested that extrusion through a small-diameter nozzle contributed to preferentially aligning the primary hydrate phases along the print path compared to a more random arrangement in traditional casting.

These findings suggest that 3D printing through a small-diameter nozzle can provide a way for a greater control of the mesoscale agglomeration process of C–S–H, which could lead to stronger, more durable, and sustainable cement-based materials.

CHAPTER 4

EARLY-AGE PERFORMANCE OF 3D PRINTED CARBON NANOFIBER AND CARBON MICROFIBER CEMENT COMPOSITES

This chapter is adapted from Early-Age Performance of 3D Printed Carbon Nanofiber and Carbon Microfiber Cement Composites published in the Transportation Research Record and has been reproduced with the permission of the publisher and my co-authors: Brown L. and Sanchez F. https://doi.org/10.1177/0361198120902704.

4.1. Overview

This study presents on the extrusion process of cement ink with carbon nano and microfibers during 3D printing and the resulting early age material characteristics. The effect of the 3D printing process on the filament structure and microstructure of the extruded cement paste was examined, and the compressive strength of the 3D printed cement composites with and without carbon nano and microfiber reinforcements within the cement ink was compared to that of their traditionally cast counterparts at seven days.

4.2. Materials and Methods

4.2.1. Materials

The materials discussed in Section 3.2.1 were used in this study including Type I/II portland cement, the polycarboxylate-based high-range water reducer (MasterGlenium 7700), the viscosity-modifying admixture (MasterMatrix VMA 362), and the anti-washout admixture (MasterMatrix UW 450). Commercially available, vapor-grown Pyrograf-III PR-19-LHT carbon nanofibers (CNFs; Applied Sciences, Inc., Cedarville, OH, USA) and polyacrylonitrile carbon microfibers (CFs; Toho Tenax America, Inc., Rockwood, TN, USA) were used as reinforcement. Per the manufacturers, the CNFs ranged from 70 to 200 nm in diameter and 30,000 to 100,000 nm in length, and the CFs were *ca.* 7 μm in diameter and 3 mm long.

4.2.2. Cement composite preparation

4.2.2.1. Cement ink design

Three cement paste mixes were developed, with and without a single type of fiber reinforcement: a plain cement mix (reference cement ink), a cement mix with 0.2% CNFs per mass of cement (CNF cement ink), and a cement mix with 0.1% CFs per mass of cement (CF cement ink). A water-to-cement ratio of 0.3, a VMA 362 loading of 0.9% (per mass of cement), a Glenium 7700 loading of 0.4% (per mass of cement), and a UW 450 loading of 1.0% (per mass of cement) were used for all mixes. These admixture loadings were within the manufacturer's recommended dosages for cementitious materials [169-171] and were found to provide adequate segregation prevention to allow for a cohesive and printable material based on preliminary testing.

All cement inks were prepared using a stainless-steel paddle bit in a mounted brushed DC motor attached to a DC power supply to control the rotation speed. For the cement ink containing CFs, the fibers were added to the cement powder and allowed to mix for 2 min at 400 RPM before the addition of water and admixtures. For the cement ink containing CNFs, the fibers were added to the water and admixtures and sonicated using a 500 W probe sonicator (Fisher Scientific Model 505 Sonic Dismembrator, Hampton, NH, USA) operating at 50% power amplitude with a 20 s on/off pulse for a total time of 10 min. Once the water, admixtures, and fibers (where applicable) were added to the cement powder, the cement inks were mixed for 3 min, with the first minute spent gradually increasing the rotation speed from 200 RPM to 1000 RPM, and the remaining two minutes spent at 1000 RPM.

4.2.2.2. Preparation of 3D printed and cast cement composites

All 3D printed cement composite columns were created according to the procedures outlined in Section 3.2.2.2. A minimum of five replicates were 3D printed and five replicates were cast of each cement ink.

4.2.3. Characterization

4.2.3.1. Slump test

Slump measurements were initially attempted with a miniature Abrams slump cone constructed from polytetrafluoroethylene [230]. However, the cement inks tested were too viscous for this

method and would not release from the cone under their own weight. Therefore, the cement inks were slump tested using a straight piece of polyvinyl chloride with an inner diameter of 4.1 cm and a height of 3.8 cm.

4.2.3.2. Scanning electron microscopy

An FEI Quanta FEG 650 environmental scanning electron microscope (ESEM) (FEI Company, USA) equipped with a Schottky field emission gun and energy dispersive X-ray spectroscopy (EDS) was used to collect SEM backscatter electron (BSE) images from the internal faces of fractured surfaces as well as polished samples recovered after MTS testing. Polished samples were epoxy mounted and polished in four steps, first with 320 grit and 600 grit silicon carbide paper, then with 6 µm and 1 µm diamond paste on a polishing cloth. An accelerating voltage of 15.0 keV, a chamber pressure of 130 Pa, and a working distance of 10.5 mm were used.

BSE images collected at 400x were thresholded using ImageJ (National Institute of Health, Bethesda, MD) to create a binary image that provided segmentation between unhydrated cement particles and all other phases. To prevent spurious results from microscale particles, only particles larger than 15 μm^2 were included in the analysis. The final binary image was then analyzed for area coverage of the unhydrated cement particles. For each sample type, 50 images were analyzed. Similarly, large area BSE images of printed filaments of the 3D printed cement composite fabricated with the CF cement ink were analyzed using the ImageJ software and in-house developed Matlab codes to determine the density and the average minimum CF-to-CF distance.

4.2.3.3. Compressive Testing

Before compressive testing, the top and bottom surfaces of the 3D printed and cast samples were ground using a 320 grit polishing cloth until each surface was within 0.5 degrees from perpendicularity to the axis according to the specifications in ASTM C39 [231]. Compressive testing was conducted at 7 days of age using an MTS 810 material testing system (MTS Systems Corporation, USA) in displacement-control mode with a loading rate of 5 µm/s according to a modified ASTM C39 [231]. The load was applied along the build direction from the top surface of the 3D printed samples, such that it was orthogonal to both directions of the rectilinear print path (Figure 4-1). The load direction with respect to the print path was selected to account for the

anisotropic nature of 3D printed materials. The literature has shown that the orientation of the print pattern with regards to the compressive loading direction can have a direct influence on the material compressive properties with the highest strengths expected when the load is applied orthogonally to the print path [13, 20, 54, 76] . A minimum of five rectilinear 3D printed and five cast samples of each cement ink type were tested. Testing was allowed to proceed until the load dropped to 25% of the maximum load.

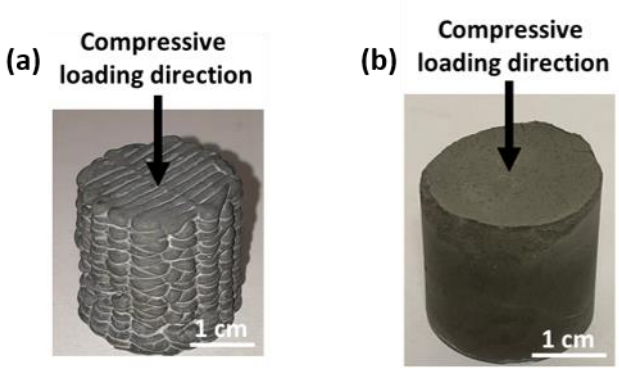

Figure 4-1. Compressive loading direction shown for (a) a 3D printed cement composite sample in a rectilinear pattern, and (b) a cast cement composite sample.

4.3. Results and Discussion

4.3.1. Extrusion and filament formation

The early-age behavior of the tested cement inks was characterized by their stiff consistency and minimal slump (Figure 4-2a). The low slump of the cement inks was necessary to allow each printed filament to support the weight of subsequent layers without deformation and to preserve the shape integrity of the overall structure. No significant difference in the slump behavior was seen between the different cement inks.

During the extrusion process, a layer of water could be observed at the surface of the printed filaments with all cement inks (Figure 4-2b). This layer of water was thought to be the result of water being driven from the bulk cement ink into the extruded filament due to the extrusion pressure inside the 3D print head (liquid phase filtration), which resulted in the formation of a lubrication layer along the wall of the nozzle (drainage) that facilitated the flow of the cement

ink. Consequently, the remaining cement ink in the 3D print head after completion of the print appeared considerably dryer and more consolidated than the extruded cement ink. The sensitivity of cement pastes during extrusion to drainage and liquid phase filtration through the granular solid has been previously reported in the literature [232]. These observations further indicated the heterogeneous evolution of the cement ink inside the 3D print head with the formation of a consolidated, low-water content zone and the presence of a high-water content, shearing zone at the extrusion nozzle.

The reinforcement type was found to influence the mechanism of the extrusion process. The cement ink with CNFs tended to underextrude, producing a printed filament with a smaller diameter compared to that obtained using the reference cement ink, while the cement ink with CFs tended to be subjected to sudden discontinuation of extrusion and occasionally resulted in a failed print (Figure 4-2c). The underextrusion seen with the CNF cement ink was thought to be caused by the hydrophobicity of the CNFs, which, locally, repelled water into the bulk of the cement ink and under the extrusion pressure drove some of the water out of the cement ink, resulting in a thicker lubrication layer (i.e., more drainage). This led to a thinner diameter printed filament compared to that of the reference cement ink printed under the same conditions. The discontinuation in the filament extrusion with the CF cement ink was thought to be due to a combination of blockages caused by the CFs that were transverse to the printing nozzle and were not able to pass through (1.6 mm nozzle diameter versus 3-6 mm average CF length) and an increased viscosity of the cement ink in the presence of CFs that limited the migration of paste water through the print head and thus liquid phase filtration. Short carbon fiber additions have been shown in the literature to increase the viscosity of fresh cementitious materials [118].

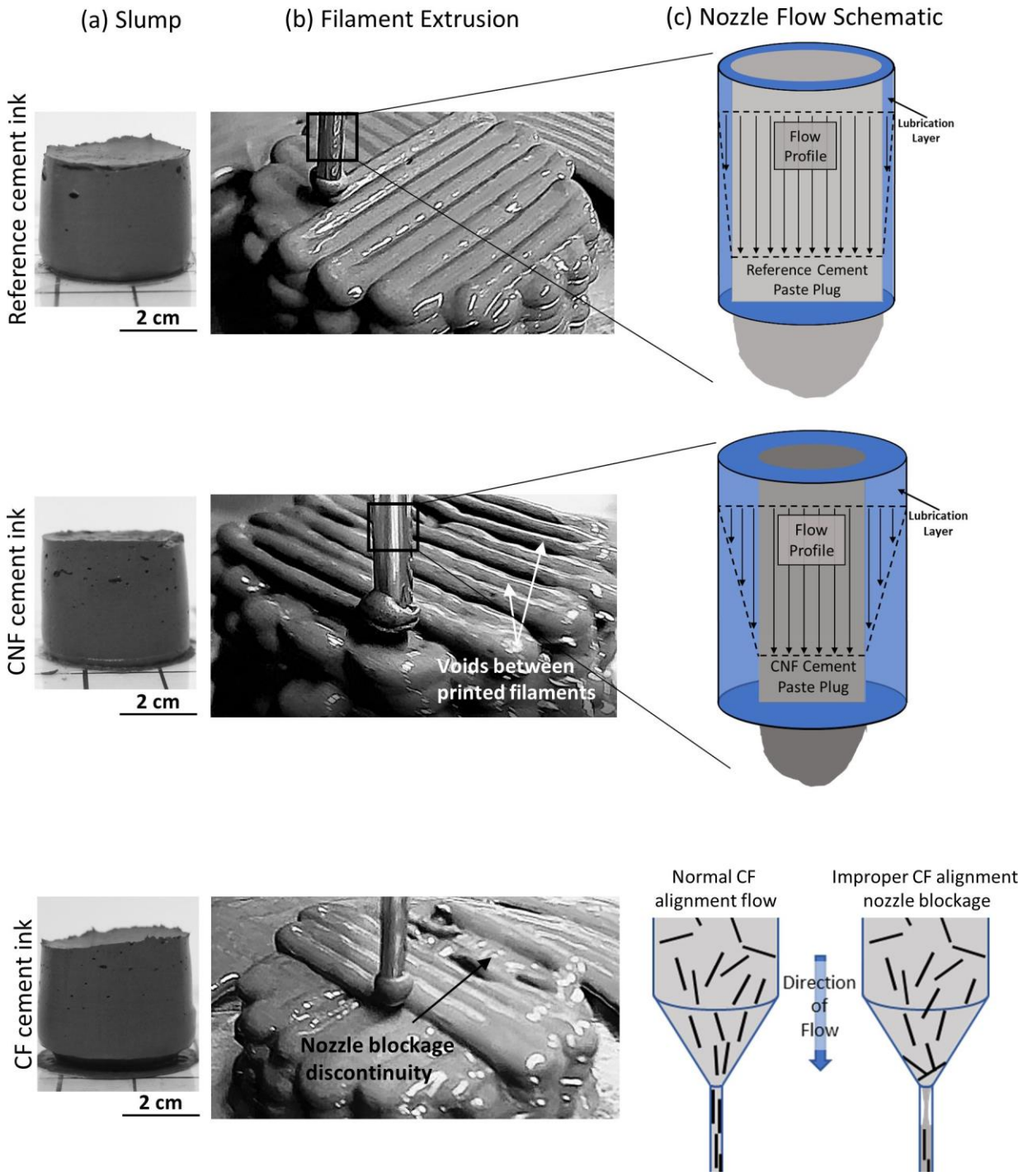

Figure 4-2. (a) Slump, (b) filament extrusion, and (c) nozzle flow schematics for the 3D printed cement composites fabricated with the reference cement ink, CF cement ink, and CNF cement ink.

Microstructural analysis of the 3D printed and cast cement composites further revealed that the 3D printing process influenced the level of unhydrated cement particles in the composites at 7 days, as shown from the differences in their percentage of surface coverage in the composite cross-section (Figure 4-3). The presence of unhydrated cement particles in the 3D printed cement composites was further influenced by the effect of the fibers on the extruded filament formation during the extrusion process in the case of the CFs. The 3D printed cement composites fabricated with the reference and CNF cement inks exhibited overall a lower percentage of surface coverage of unhydrated cement particles compared to their cast counterparts (*ca*. 13%-14% versus *ca*. 15%-17%), while the 3D printed cement composite fabricated with the CF cement ink had a higher percentage (*ca*. 21% versus *ca*. 17%).

The lower surface coverage of unhydrated cement particles (i.e., greater hydration) for the reference and CNF cement inks was in agreement with the presence of the liquid phase filtration during extrusion. The liquid phase filtration pushed water from the bulk cement ink inside the print head into the extruded filament, thus yielding a greater effective water-to-cement ratio in the printed filament compared to that of a cast cement paste. This greater effective water-to-cement ratio resulted in a lower surface coverage of unhydrated cement particles. In contrast, the higher surface coverage of unhydrated cement particles (i.e., lower hydration) for the CF cement ink was consistent with a lower liquid phase filtration due to the increased viscosity of the CF cement paste, which resulted in less water being pushed into the extruded filament and thus in a lower effective water-to-cement ratio in the printed filament.

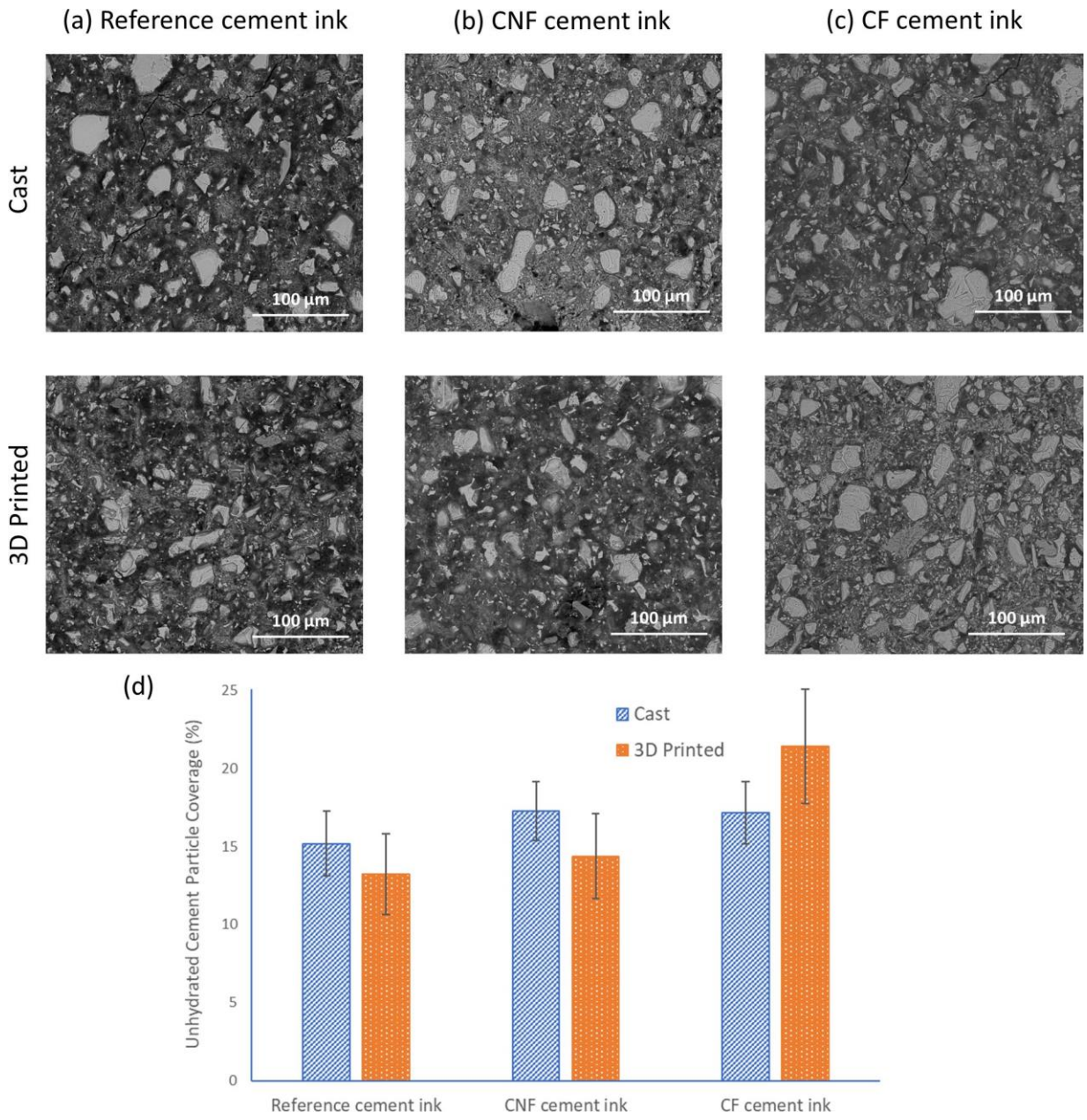

Figure 4-3. BSE images of the cast and 3D printed cement composites fabricated with (a) the reference cement ink, (b) the CF cement ink, and (c) the CNF cement ink, respectively, showing unhydrated cement particles; and (d) percentage of unhydrated cement particle surface coverage for each cast and printed cement composite type.

4.3.2. Filament morphology and fiber distribution

SEM images evidenced a heterogeneous distribution of the CNFs and CFs along the filaments in the 3D printed cement composites. For the 3D printed cement composite fabricated with the CNF cement ink, a non-uniform distribution of individually embedded and clustered CNFs were found throughout the composites similar to that of the cast cement composite. Furthermore, no apparent preferential alignment of the individual CNFs or CNF clusters was seen in the 3D printed filaments, suggesting a limited influence of the 3D printing process on the distribution of the CNFs. The CNF clusters were randomly distributed within the cement composites and were of various size and shape with a diameter of 50 µm or less. It was thought that the low slump of the tested cement inks mitigated the presence of bleed-water for both the cast and the printed cement composites, limiting the movement of the CNFs through the hydrating cement paste and thus their reagglomeration. CNF clustering has been shown in the literature to be influenced by bleed-water with an increasing gradient in cluster size in the direction of bleed-water migration [233, 234] and to be reduced by hindering the movement of the CNFs in the fresh cement paste [41, 235]. Studies and methods of quantification of CNFs in cement pastes can be found elsewhere [41, 234].

In contrast, the 3D printed cement composite fabricated with the CF cement ink exhibited a preferential alignment of the CFs, which was consistent with the directionality along the print path of the extrusion nozzle (Figure 4-4). Nozzle induced preferential alignment of fibers has been previously reported in the literature [13, 24, 236]. Additionally, the rectilinear printing pattern provided a layering effect in the CF alignment whereby fibers in each layer were oriented orthogonally to fibers in adjacent layers. Variations in CF distribution within a given layer were seen, with some areas having a high density of CFs and others having a low density (Figure 4-4d). As an example, for the filament shown in Figure 4-4d, the high CF density zone had a density of 24 fibers/mm^2 and a CF-to-CF average minimum distance of *ca*. 0.10 mm while the low CF density zone had a density of 7 fibers/mm^2 and a CF-to-CF average minimum distance of *ca*. 0.15 mm. This non-uniformity in fiber distribution within a printed layer was thought to be due to the partial blockage of the extrusion nozzle with CFs during printing, which led to a sporadic release of the CFs with, in some cases, a lower density of CFs being released from the extrusion nozzle and in others a higher density of CFs being suddenly released. In contrast, the

CFs in the cast cement composite had a more random orientation, which was consistent with the lack of extrusion pressure and lower confinement seen in traditional casting (Figure 4-4b).

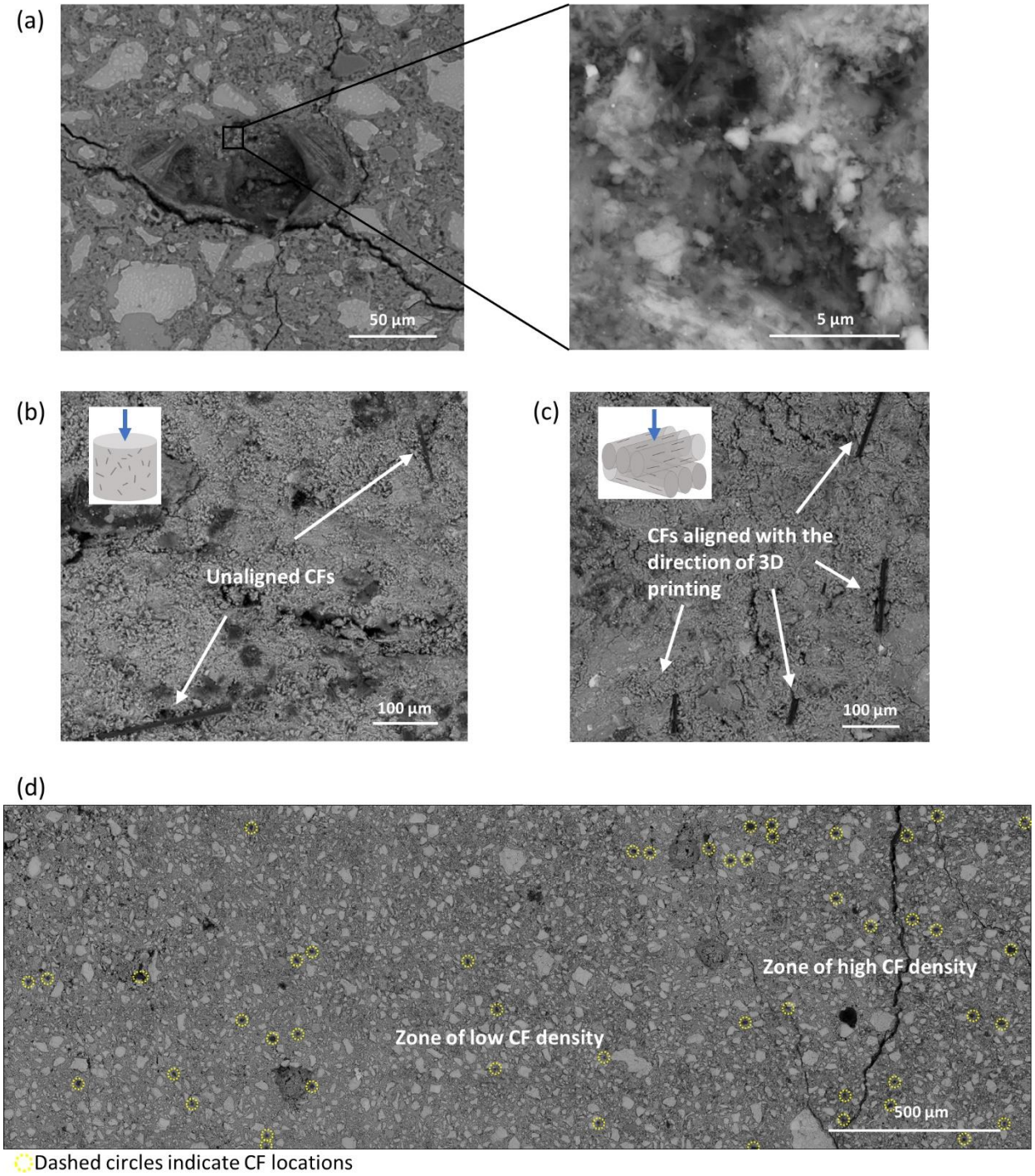

Figure 4-4. BSE images showing (a) a CNF cluster with a closeup of the fiber entanglement, (b) unaligned CFs in a cast specimen and corresponding schematic for compressive loading

direction, (c) aligned CFs in a 3D printed specimen and corresponding schematics for fiber alignment with respect to compressive loading direction, and (d) large area BSE image of a filament layer in the 3D printed cement composite fabricated with the CF cement ink.

4.3.3. Boundary interface between printed filaments

Inspection using ESEM analysis of the 3D printed cement composites generally did not show any distinctive change in microstructure that was characteristic of interfacial boundaries between printed filaments, with the exception of air cavities seen between printed filaments of the composite fabricated with the CNF cement ink (Figure 4-5). These cavities were consistent with the phenomenon of underextrusion observed with this cement ink. Examination of the mechanically tested 3D printed cement composite fabricated with the CNF cement ink indicated the presence of preferential cracking at the edges of the air cavities that coincided with the filament boundaries. This indicated a weaker interfacial bond between the filaments at the location of underextrusion. There did not seem to be, however, a notable difference in the microstructure composition between the areas surrounding the cavities and the other parts of the composite, with unhydrated cement particles being present up to the edge of the cavities (Figure 4-5b). For the 3D printed cement composite fabricated with the CF cement ink, there was no significant microstructural change indicative of the presence of an interfacial region between filaments. However, layers of alternating CF orientations within adjacent filaments could be seen, indicative of the rectilinear printing pattern (Figure 4-5c).

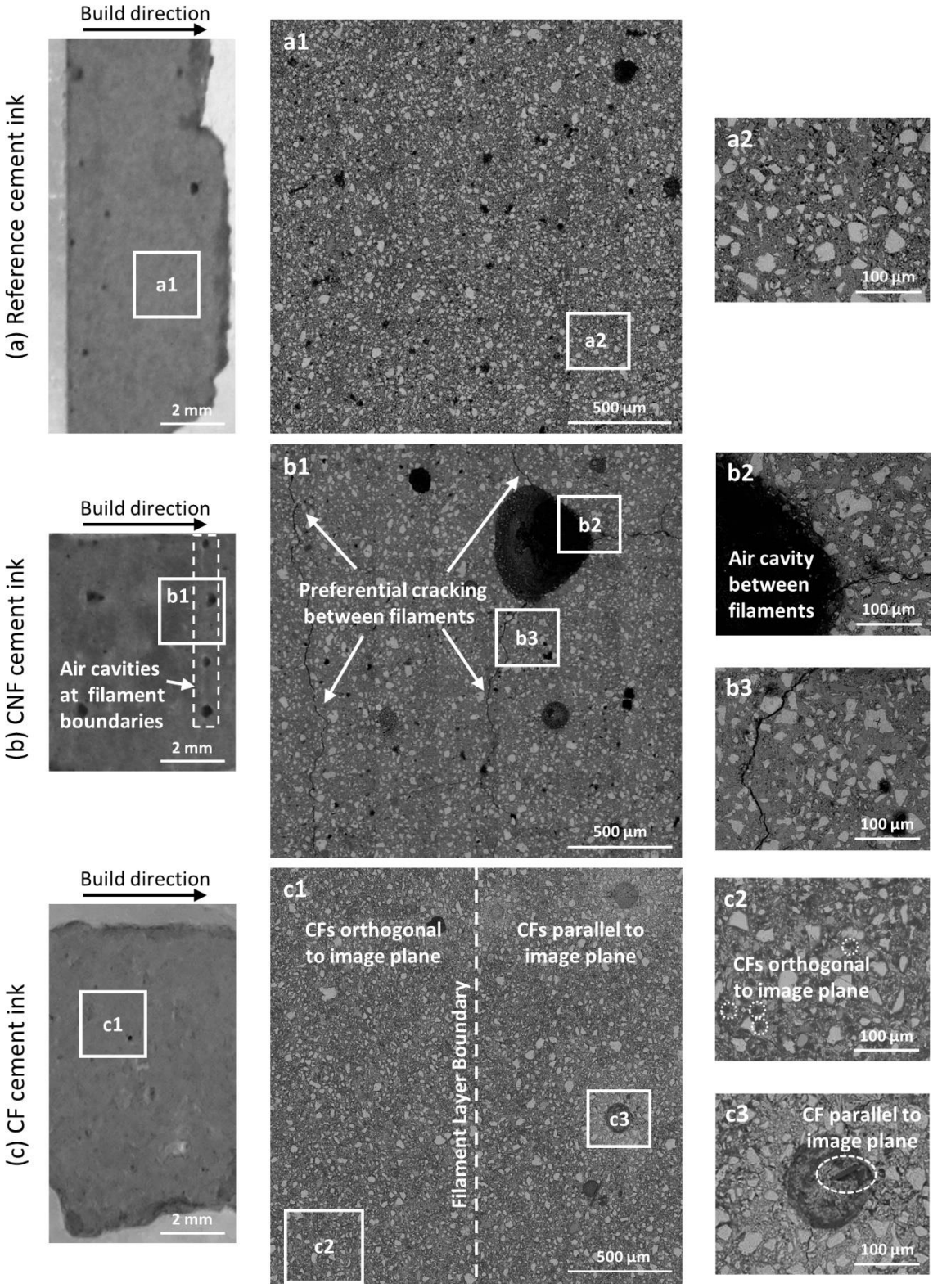

Figure 4-5. Photographs of representative specimens (left), BSE large-area map (middle), and BSE images (right) of the 3D printed cement composites fabricated with (a) the reference cement

ink, (b) the CNF cement ink, showing air cavities between printed filaments and preferential cracking, and (c) the CF cement ink, showing CF orientation in adjacent filament layers.

4.3.4. Compressive strength at 7 days

3D printing resulted overall in lower average compressive strengths of the 3D printed cement composites compared to their cast counterparts (Figure 4-6a). It was thought that load transfer differences between the cast and 3D printed cement composites contributed to the lower overall strength of the 3D printed specimens, with load being preferentially transferred in the 3D printed specimens along the boundary interface between the printed filaments.

The type of fiber reinforcement (CNFs versus CFs) in the cement ink further affected the compressive strength behavior of the 3D printed cement composites. The cement composites fabricated with the CNF cement ink had a more drastic reduction in average compressive strength from cast to 3D printed (44%) as compared to that fabricated with the reference cement ink (20%) or to that fabricated with the CF cement ink (15%). The underextrusion seen in the 3D printing process for the CNF cement ink likely weakened the interfacial bonds between filaments, further reducing the load transfer capabilities of this 3D printed cement composite (Figure 4-5b). The smaller strength reduction of the 3D printed cement composite with CF cement ink was attributed to the compressive loading direction that was orthogonal to the aligned CFs along the direction of the print path, leading to a fiber loading condition that more closely mimicked flexural behavior. This unidirectional loading with respect to the fibers and print path was in contrast to that of the cast cement composite with CFs for which the CFs were in a random orientation. Embedded short fibers have been shown in the literature to provide the most benefit to the mechanical properties of the material when they are oriented orthogonal to the direction of the load [14, 237-240].

The effect of the nozzle induced CF alignment and filament layering due to 3D printing was visible on the post yield stress behavior with the continued resistance to compression after the maximum yield stress had been reached. This was characterized in the compressive stress-strain curves (Figure 4-6b) by a continued increase in strain capacity with a tapering of the stress

retained by the composite until final rupture (i.e., strain softening behavior). A similar post peak stress behavior has been recently reported in the literature for 3D printed mortars with short straight steel fibers during flexural testing [241].

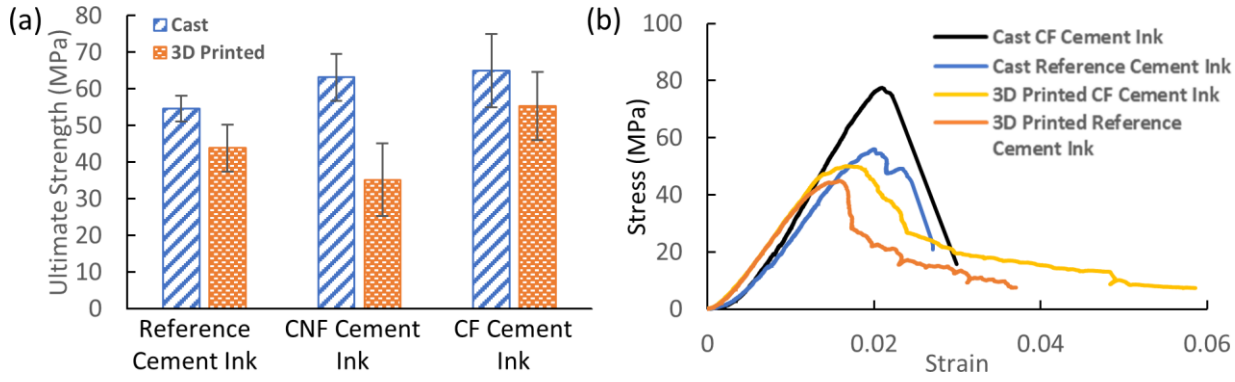

Figure 4-6. (a) Average ultimate compressive strength of each cement composite type and (b) typical stress-strain curves for the 3D printed cement composites fabricated with the reference and CF cement inks.

4.4. Conclusions

Cement inks with CNFs and CFs were developed and used to fabricate internally reinforced 3D printed cement composites. Results showed the extrusion process resulted in a heterogeneous evolution of the cement ink inside the 3D print head with the presence of a high-water content, shearing zone at the extrusion nozzle as a result of liquid phase filtration inside the 3D print head. The following conclusions could be drawn:

- The CNF cement ink tended to underextrude (thinner printed filaments) because of the hydrophobic character of the CNFs, while the CF cement ink led to sudden discontinuation of extrusion and occasionally failed prints due to CF transverse orientation with respect to the nozzle. The underextrusion seen with the CNF cement ink led to regularly spaced air cavities between the printed filaments, likely weakening the bond between the filaments and reducing the load transfer capability of the 3D printed cement composite.

- No notable interfacial region between printed filaments in the 3D printed cement composites were found with the other cement inks.
- For the CF cement ink, the extrusion resulted in a nozzle induced preferential alignment of the CFs along the print path due to the greater length of the fibers relative to the diameter of the nozzle.
- While 3D printing resulted in lower compressive strength of the composites in the direction orthogonal to the print path compared to traditional casting, the addition of CFs within the cement ink reduced the strength difference between the cast and 3D printed cement composites and provided a strain softening in the post peak behavior.

CHAPTER 5

MULTISCALE MECHANICAL PERFORMANCE OF 3D PRINTED HALLOYSITE NANOCLAY CEMENT COMPOSITES

The results of this chapter are being incorporated into the following manuscript:

Kosson M., Brown L., and Sanchez F. Multiscale Mechanical Performance of 3D Printed Halloysite Nanoclay Cement Composites. Expected submission August 2022.

5.1. Overview

In this study, statistical grid nanoindentation was paired with environmental scanning electron microscopy (ESEM) and energy dispersive X-ray spectroscopy (EDS) to examine the micromechanical properties (modulus and hardness) and microstructure of filaments in 3D printed cement paste structures with 5% replacement of cement with HNC. A cast cement paste created using the same formulation was also tested as a reference for comparison. In addition, results were compared to those of an otherwise identical 'neat' ordinary portland cement (OPC) ink with no HNC from a previous study by the author (Chapter 3). EDS and thermogravimetric analysis (TGA) results are also reported to show the effect of HNC incorporation and extrusion process on the chemical properties of the printed filaments. Compressive and flexural macromechanical testing was also performed on 3D printed and cast structures to examine the effects of HNC incorporation and extrusion process on bulk mechanical performance. Results showed that HNC incorporation resulted in the formation of low and high mechanical property filaments, which corresponded to the presence of zones of high and low concentrations of HNC and partial HNC agglomeration. However, HNC replacement of cement did not significantly affect the mean macromechanical strength of 3D printed structures, though variance in properties was significantly reduced by improving filament consistency.

5.2. Materials and Methods

5.2.1. Materials

The materials discussed in Section 3.2.1 were used in this study including Type I/II portland cement, the polycarboxylate-based high-range water reducer (MasterGlenium 7700), the

viscosity-modifying admixture (MasterMatrix VMA 362), and the anti-washout admixture (MasterMatrix UW 450). Halloysite nanoclay (HNC) (Sigma-Aldrich, USA) was used to control fresh rheology and increase thixotropic behavior.

5.2.2. Cement paste preparation

5.2.2.1. Cement ink design

Two cement paste mixes were developed, with and without 5% of the cement being replaced with HNC (HNC cement ink and OPC cement ink, respectively). For both mixes, a water-to-solids ratio of 0.3, a VMA 362 loading of 0.9% (per mass of solids), a Glenium 7700 loading of 0.35% (per mass of solids), and a UW 450 loading of 1.0% (per mass of solids) were used. These admixture loadings were within the dosages recommended by the manufacturer for cementitious materials [169-171] and provided enough rheology control and segregation prevention to allow for a reproducibly printable material in preliminary testing.

The admixtures and water were measured together, then sonicated using a 500 W probe sonicator (Fisher Scientific Model 505 Sonic Dismembrator, Hampton, NH, USA) for 20 s at 50% power to ensure homogenization. For the HNC ink, HNC was added to the cement and manually mixed until heterogeneity was not visible, then mixed with the mixing apparatus for 1 min at 400 RPM. The sonicated water and admixtures were then added to the cement powder (and HNC where applicable), and the cement inks were mixed for 1 min, with the rotation speed gradually increasing from 400 RPM to 1000 RPM, then for 2 min at 1000 RPM.

5.2.2.2. Preparation of 3D printed and cast cement paste composites

All 3D printed cement ink specimens were printed on a Hydra 430 gantry model 3D printer with EMO-XT modular printing heads (Hyrel 3D, USA; Figure 3-1a). An .STL file for a cylinder 2.49 cm in diameter and 2.5 cm in height was sliced into 1 mm high layers with a rectilinear pattern (such that each successive layer was printed perpendicularly to the previous layer) to create a column structure for micromechanical testing, microstructural analysis, and compressive testing. For flexural testing, an .STL file for a beam 7.4 cm long by 1.8 cm wide by 1.5 cm high was generated, and a slicing recipe with a concentric infill pattern (such that all filaments ran the length of the beam, orthogonal to the loading direction), and a layer height of 1 mm was used.

After mixing, the HNC cement ink, which had a higher viscosity but more resistance to paste segregation, was loaded into the 3D print head in a single stage with the aid of a vibrating table, then tamped. The OPC cement ink was loaded into the 3D print head in multiple stages and tamped with a 1.6 mm diameter rod to mitigate entrapped air after each stage. The cement inks were extruded through a 14-guage needle tip (inner-diameter 1.6 mm) onto a glass or acrylic substrate. Cylinders were 3D printed 25 layers high, which yielded a column structure that was *ca*. 2.5 cm in diameter and 2.5 cm in height (Figure 3-1b). Beams were printed 15 layers high, which yielded a flexure testing structure that was *ca.* 7.4 cm in length by 1.8 cm in width by 1.5 cm in height (Figure 5-1a).

Cast specimens (Figure 3-1d and Figure 5-1b) were similarly poured either into cylindrical molds with a diameter of 2.5 cm and a height of *ca.* 2.5 cm or beam molds with a length of 7.4 cm, a width of 1.8 cm, and a height of *ca.* 1.5 cm. Casting was conducted in multiple stages for the OPC ink, with tamping occurring after each stage to mitigate air bubbles. A vibrating table was again used to cast in a single stage for the HNC ink.

One column was printed and one cast with the HNC ink for micromechanical and microstructural characterization. Three printed and three cast columns previously tested with the OPC ink were used as reference. One column was printed and cast with each ink for thermogravimetric analysis. Six columns and six beams were printed and cast each with each cement ink for compressive and flexural testing, totaling forty-eight macroscale mechanical testing specimens.

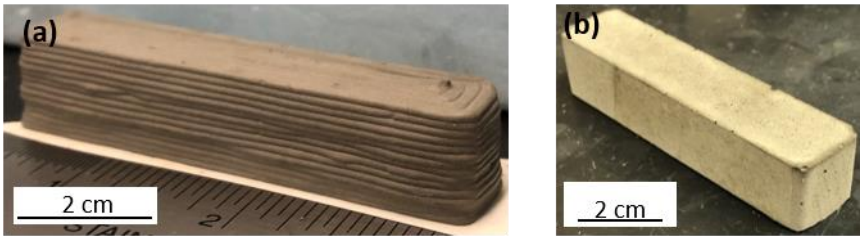

Figure 5-1. Flexural testing beams (a) cast, and (b) 3D printed with a concentric pattern

5.2.3. Microstructural and chemical characterization

5.2.3.1. Sample preparation for nanoindentation and microstructural analysis

One 3D printed and one cast column structure was prepared for nanoindentation and microstructural analysis according to the procedure described in Section 3.2.3.1.

5.2.3.2. Grid nanoindentation and statistical analysis

Grid nanoindentation and statistical analysis was performed on polished specimens according to the procedure described in Section 3.2.3.2.

5.2.3.3. ESEM and EDS characterization

Backscattered electron (BSE) images and energy dispersive X-ray spectroscopy (EDS) spectra were collected on polished samples according to the procedure described in Section 3.2.3.3.

Microstructural features and micromechanical properties were spatially correlated by overlaying indent markers on their corresponding location on these BSE maps and color-coding them based on to which peak they were most likely to belong (Figure 5-2). Chemical composition at each indent was determined by averaging the EDS spectra for each pixel in a 5-by-5 pixel square around the pixel for the calculated indent location, removing porosity-associated pixels as determined from ImageJ thresholding analysis. Further image analysis was conducted on grid-area BSE images (6 images per grid area) with ImageJ by thresholding images based on grayscale range to determine the proportion of the microstructural area associated with phases of interest, particularly unhydrated cement particles and clusters of HNC. Only images associated with the grid area could be used for this analysis, as only grid areas had known micromechanical properties that could be correlated with microstructural analysis. This limitation prevented the analysis of a larger area of the microstructure with this method.

In addition to using the framework defined in [182] to categorize hydrated phase-associated indents into five categories as described in Section 3.2.3.3, a sixth category associated with HNC clusters was defined as indent with a (Si + Al)/Ca ratio greater than 0.85.

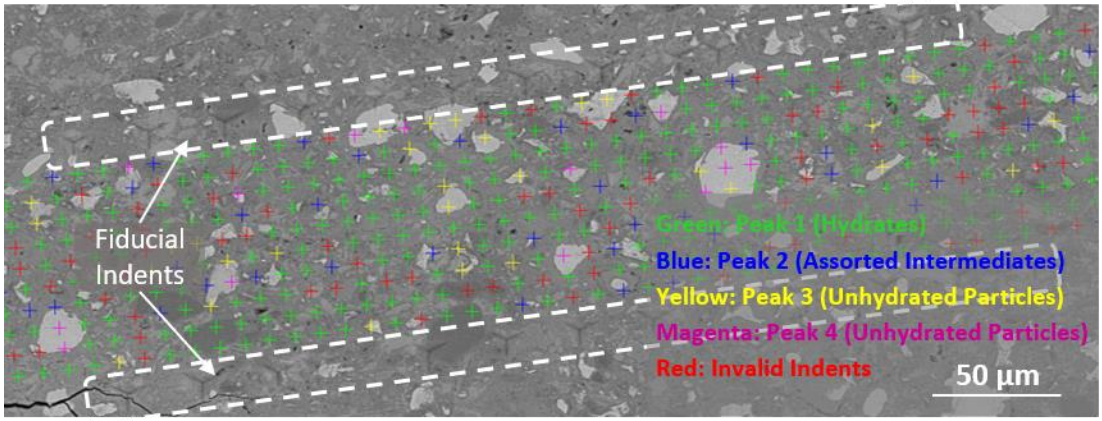

Figure 5-2. BSE map of a grid area showing the lines of fiducial indents and cross icons at indent locations.

5.2.3.4. Thermogravimetric analysis

For each cement ink formulation, a 3D printed rectilinear column and a cast column were crushed into fine powder using a mortar and pestle, totaling four powder specimens. A Q600 SDT analyzer (TA Instruments, USA) was used to conduct thermogravimetric analysis (TGA) on three replicates of each specimen type. For each replicate, approximately 30 mg of specimen powder was used. Each TGA replicate was conducted by heating the sample up to 1000 °C at a rate of 10 °C/min in a chamber continuously flushed with nitrogen. Characteristic peaks in derivative weight versus temperature plots were identified to measure weight loss associated with the thermal decomposition of CH and calcium carbonate ($CaCO_3$). The impacts of printing and HNC incorporation on carbonation were also examined with this method to investigate the reactivity of the CH during curing. The primary peaks associated with the thermal decomposition of CH and $CaCO_3$ were identified as being centered around approximately 440 °C and 690 °C, respectively, for all sample types. The temperature range associated with decomposition was determined to be 395-470 °C for CH and 630-720 °C for $CaCO_3$ (Figure 5-3). Because CH decomposes into calcium oxide and water vapor, a stoichiometric constant of 4.12 was used to multiply the weight loss associated with CH decomposition to determine the mass percentage of CH in the microstructure. Similarly, the weight loss associated with calcium carbonate was

multiplied by a stoichiometric constant of 2.28 to convert the mass lost in the form of carbon dioxide to mass of calcium carbonate in the sample.

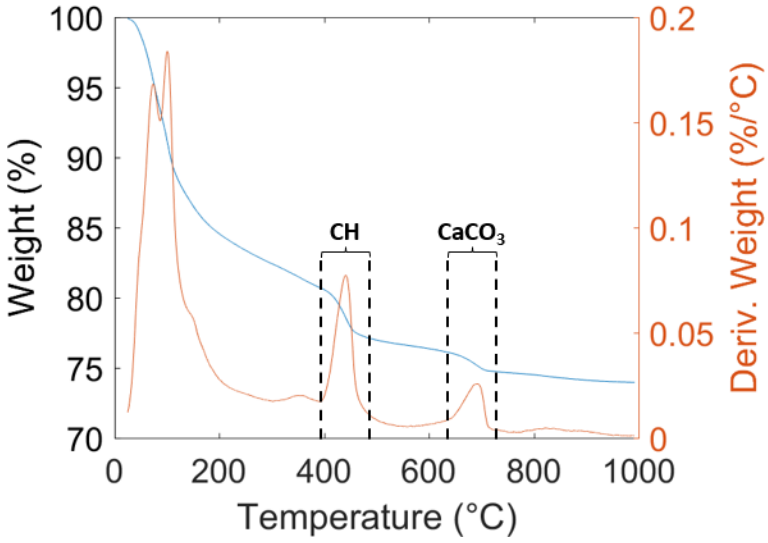

Figure 5-3. TGA curve for a 3D printed HNC ink specimen showing characteristic peak ranges for CH and $CaCO_3$.

5.2.4. Macromechanical testing

5.2.4.1. Macroscale compressive testing

Before compressive testing, the top and bottom surfaces of all specimens were ground until each surface was within 0.5 degrees from perpendicularity to the axis according to the specifications in ASTM C39 [231] using 320 grit silicon carbide paper. Compressive testing was conducted on 35 day-old specimens in a saturated-surface-dried condition using a Tinius Olsen Super L 60 K universal testing machine (Tinius Olsen, Inc., USA) in displacement-control mode with a loading rate of 5 µm/s according to a modified ASTM C39 [231]. The load was applied to the top surface of the specimens, such that it was perpendicular to both directions of the rectilinear print path for printed specimens (Figure 5-4a). Previous literature has shown that 3D printed cementitious materials have mechanical anisotropy, with the highest strengths to be expected with the load perpendicular to the print path [13, 20, 54, 76], so load direction was selected to enable maximum compressive response for the 3D printed specimens. Six 3D printed and six cast

specimens of each cement ink type were tested. Testing proceeded post-yield until the load was 25% of the peak load.

5.2.4.2. Macroscale flexural testing

Before flexure testing, the top surfaces of the 3D printed and cast samples were ground using 320 grit silicon carbide paper until each surface was visibly flat. Three-point bending flexural testing was conducted on 35 day-old specimens in a saturated-surface-dried condition using a Tinius Olsen 50ST universal testing machine in displacement-control mode with a loading rate of 100 µm/min according to a modified ASTM C293 [242]. The load was applied to the top surface of the 3D printed samples, such that it was orthogonal to all filaments running the length of the beam, also selected to account for the anisotropic nature of 3D printed materials (Figure 5-4b). Six 3D printed and six cast specimens of each cement ink type were tested. Testing was allowed to proceed until brittle sample failure.

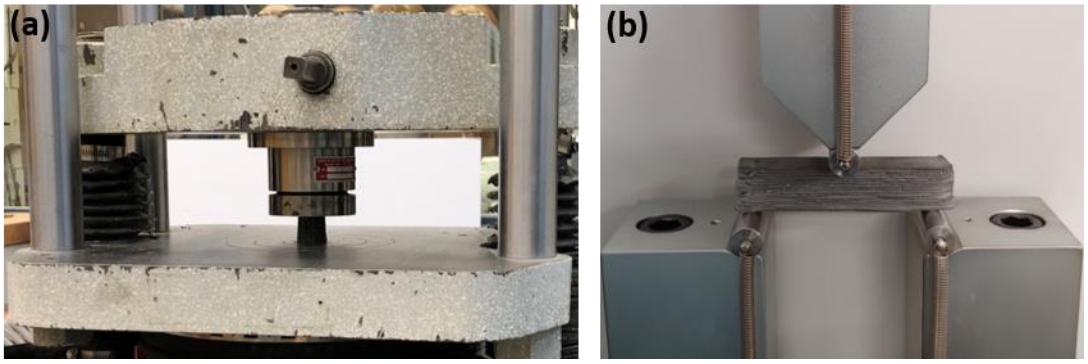

Figure 5-4. Macroscale mechanical experimental setup for (a) compressive testing and (b) three-point bending flexure testing.

5.3. Results and Discussion

5.3.1. Qualitative observations of the influence of HNC incorporation on filament formation and 3D printing of cement pastes

The incorporation of halloysite nanoclay (HNC) into the cement ink significantly changed the behavior of the cement paste in the fresh and hardened states. In the fresh state, HNC incorporation was observed to increase the viscosity of the paste, necessitating the use of a

vibrating table to load the printing heads. However, the ink was also more cohesive and less prone to water segregation, resulting in it being able to withstand the vibrations necessary for loading and having visibly less surface water than the OPC ink during filament extrusion (Figure 5-5a and b). The increased viscosity and decreased segregation resulted in printed filaments that were more consistent (less prone to segregation-induced underextrusion or discontinuities, Figure 5-5c and d) and had improved buildability compared to the OPC ink (decreased deformation under the weight of successive layers, visible when observing the relative deviation from the intended rectangular cross-sectional shape in Figure 5-6a and b). The reduction in surface water resulted in the HNC inks having a slightly rougher surface quality.

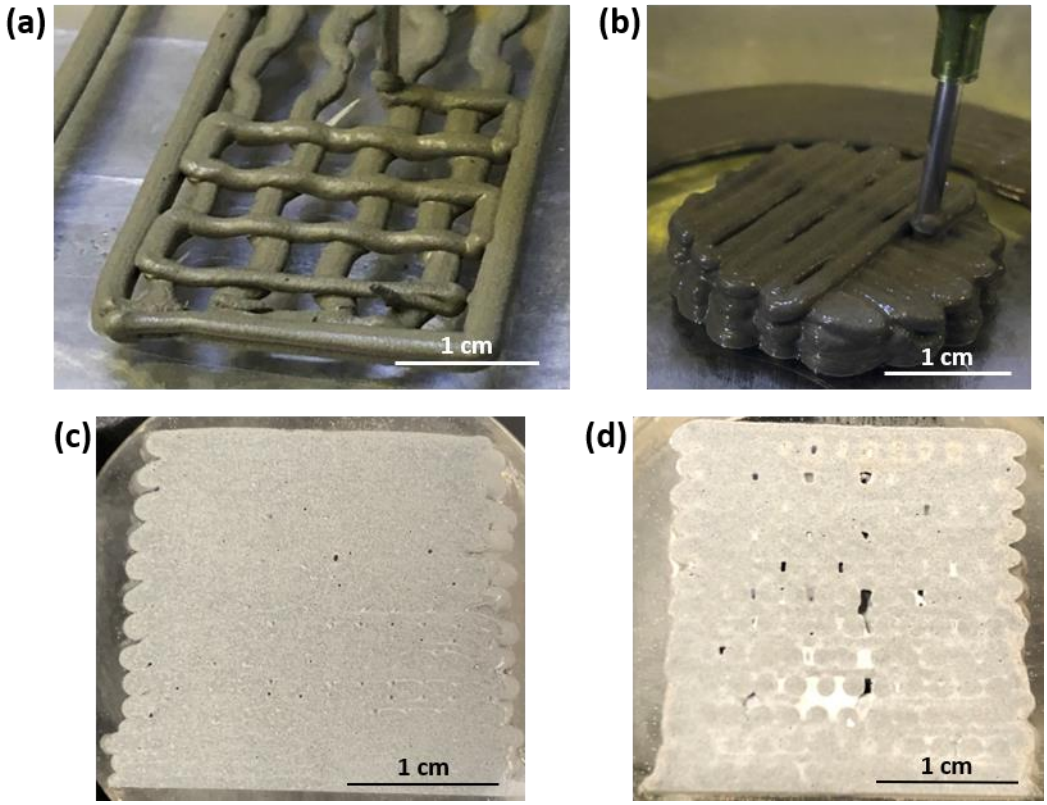

Figure 5-5. Extruded filaments 3D printed with (a) the HNC ink and (b) the OPC ink showing visibly more surface water. Polished cross-sections of specimens 3D printed with (c) the HNC ink and (d) the OPC ink showing an increase in printing errors (discontinuities, underextrusion, and structural shape).

Visual inspection of the fracture surfaces from beams of each cement ink type after flexural testing revealed that the macropores tended to be smaller in printed filaments for the HNC ink (less than 0.2 mm diameter) than the OPC ink (up to 0.5 mm diameter), and that they were larger (up to 1 mm diameter) and more frequent in the cast specimens for both ink types (Figure 5-6). This change suggested that printing had a consolidating effect on the filaments, removing larger air voids, especially for the HNC ink. Interlayer interfaces were slightly lighter in color than the bulk filament in some places for the HNC ink, though not for the OPC ink, possibly because the bleed water increased interlayer mixing for the OPC ink. However, there was no evidence of change in the interfacial microstructure when observed through BSE imaging and EDS analysis.

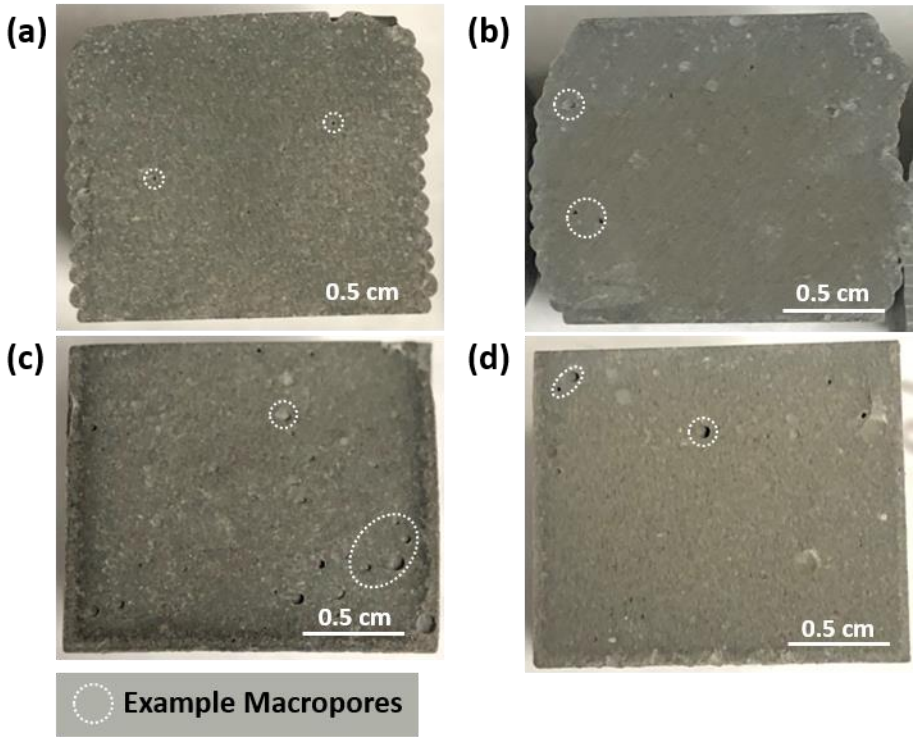

Figure 5-6. Cross-sections of flexure tested beams 3D printed with (a) the HNC ink (b) the OPC ink and cast with (c) the HNC ink and (d) the OPC ink.

5.3.2. Local mechanical properties

5.3.2.1. Local indentation modulus and hardness

The difference in response of the cement inks to the extrusion-based printing process was evidenced by variation in the median indentation moduli between the multiple locations probed on each printed structure, as measured by grid nanoindentation. Similar to previously reported for the OPC ink, the structures printed with the HNC ink displayed printed filaments that exhibited either low mechanical property (LMP; one grid area) or high mechanical property (HMP; two grid areas) filaments. For clarity, the following analysis focuses the presentation of the results and discussion on only one HMP filament grid area as the representative HMP filament.

The median modulus for the HNC ink HMP filament (Table 5-1) was significantly higher than that for the OPC ink HMP filaments (33.9 ± 4.8 GPa, compared to 23.1 – 27.9 GPa), while the HNC ink LMP filament was somewhat below the OPC ink LMP filament range (12.9 ± 1.6 GPa, compared to 13.7 – 18.8 GPa). The HNC ink cast specimen had a median modulus that was similar to the range of its OPC ink counterparts (28.1 ± 4.9 GPa, compared to 26.7 – 27.8 GPa), suggesting that HNC incorporation had a minimal effect on the micromechanical properties of the cast cement paste. The effect on hardness was generally observed to be smaller, with the HNC ink filaments and cast specimen having median hardness values that were either within or slightly above the ranges measured for the OPC ink. For the HNC ink, 81% of the LMP filament indents had a modulus value in the 10-20 GPa range, compared to only 1% for the HMP filament and 8% for the cast. For the HMP filament, nearly half (47%) of indents had a modulus value in the 30-40 GPa range, while the cast specimen had a majority (51%) in the 20-30 GPa range. Differences were smaller for the hardness distributions, though the LMP filament did have the highest proportion of indents (48%) in the 0-1 GPa range, while the HMP filament had the highest proportion of indents (56%) in the 1-2 GPa range (Figure 5-7).

For the HNC ink, it was observed that the presence of hydrophilic HNC significantly arrested the segregation of paste water, as evidenced by an apparent reduction in surface water on fresh filaments and an increase in filament consistency. This observation further indicated that the effect of water redistribution and change in local w/s ratio of the extruded filaments as the extrusion progressed that were previously reported by the authors as the mechanism affecting the

filament micromechanical properties was likely limited in the presence of HNC. Rather, the differences in the micromechanical properties of the HNC ink filaments were thought to be the results of other mechanisms related to the extrusion process.

Table 5-1. Median values (± median absolute deviation) of the indentation modulus and hardness for 3D printed and cast specimens with the HNC cement ink.

	Modulus (GPa)	**Hardness (GPa)**
LMP Filament	12.9 ± 1.6	1.0 ± 0.2
HMP Filament	33.9 ± 4.8	1.2 ± 0.3
Cast (w/s = 0.3)	28.1 ± 4.9	1.1 ± 0.3

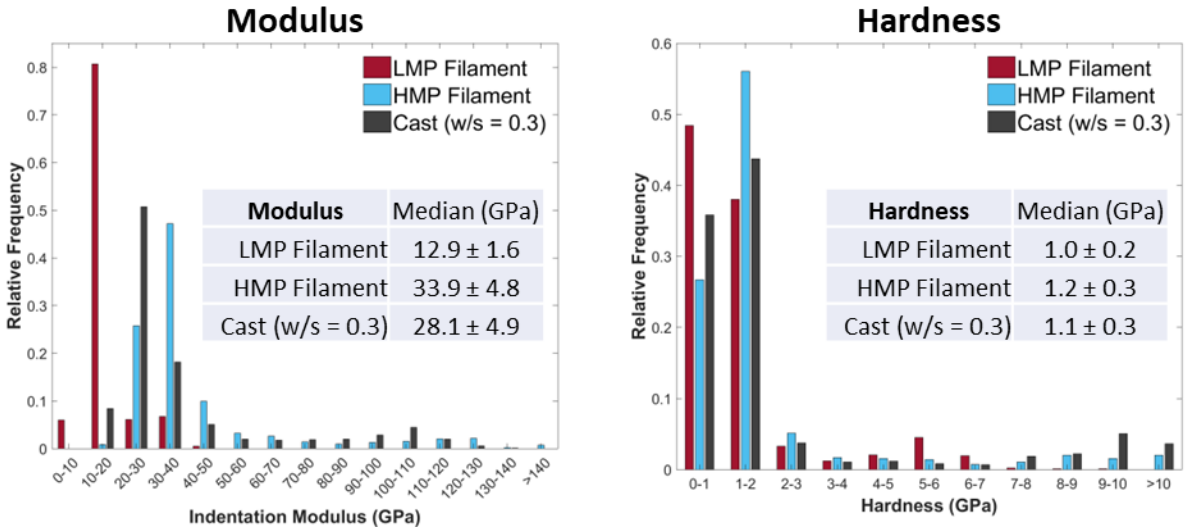

Figure 5-7. Histograms comparing modulus and hardness distributions for representative HNC ink filaments of each type and cast specimens. Median values (± median absolute deviation) are also provided.

5.3.2.2. Mechanically distinct phases from nanoindentation

Gaussian deconvolution of the modulus and hardness PDFs yielded four (4) primary distinct mechanical phases for all specimens 3D printed and cast with the HNC ink (Figure 5-8 and

Figure 5-9). The deconvolution parameters for the representative filaments and cast specimens are summarized in Table 5-2 and Table 5-3. The general trend of the peaks was the same as that previously reported for the OPC ink with the majority of indents being associated with Peak 1, no more than 25% of indents being associated with Peak 2, 16% with Peak 3, and 8% with Peak 4.

The general shape of the distributions for the HNC ink also followed that of the OPC ink, with a unimodal distribution associated with Peak 1 as opposed to separate peaks corresponding to two distinct types of the main hydrate phase C–S–H sometimes reported for cementitious materials (Figure 5-8). This behavior, which was previously attributed to the effect of viscosity-modifying and anti-washout admixtures and/or cement type used on the formation of the hydrated phases, was not observed to be significantly affected by the incorporation of HNC.

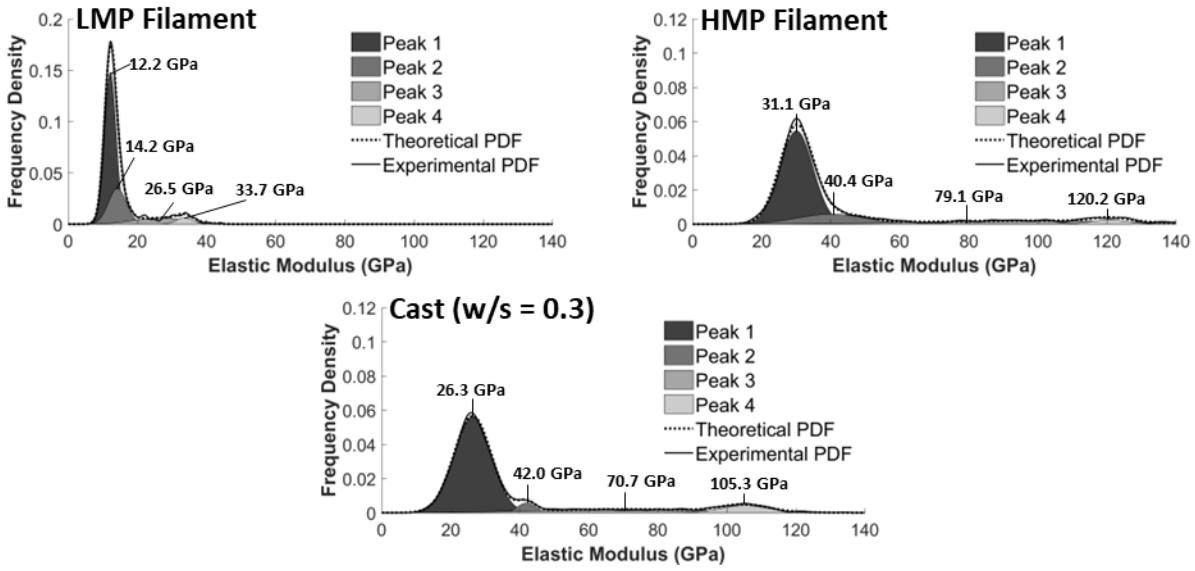

Figure 5-8. Gaussian deconvolution results for modulus for 3D printed filaments and cast cement pastes made with the HNC ink.

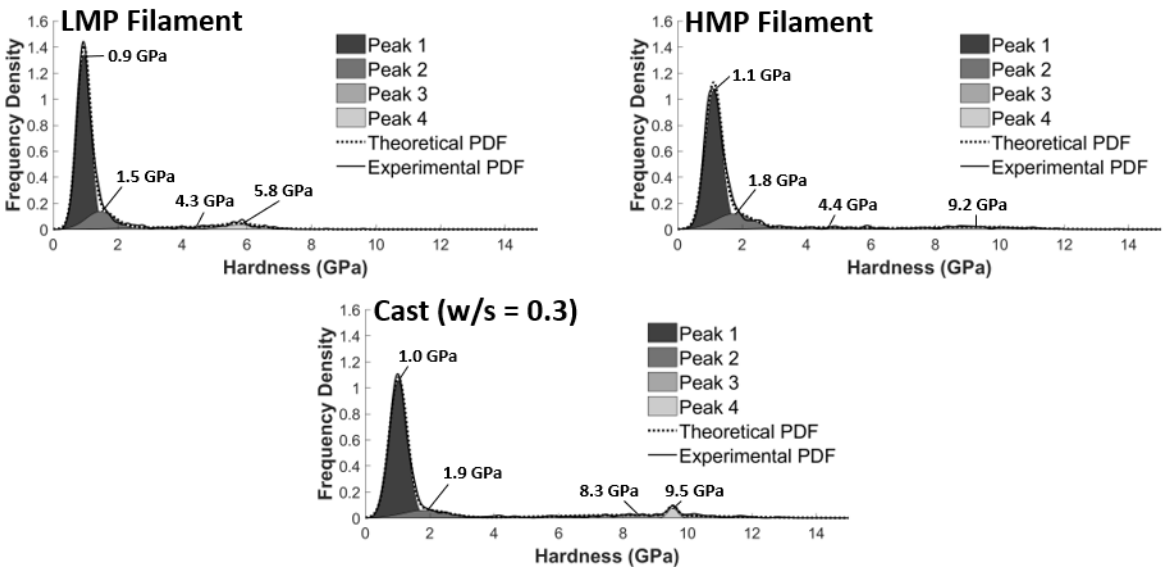

Figure 5-9. Gaussian deconvolution results for hardness for 3D printed filaments and cast cement pastes made with the HNC ink.

Table 5-2. Modulus deconvolution parameters for nanoindentation grids on 3D printed and cast specimens made with the HNC cement ink. Each grid was deconvoluted into four Gaussian distributions, with each having a characteristic mean (μ), standard deviation (σ), and weight percentage (Wt %).

	Peak 1		**Peak 2**		**Peak 3**		**Peak 4**	
	μ ± σ (GPa)	**Wt %**	**μ ± σ (GPa)**	**Wt %**	**μ ± σ (GPa)**	**Wt %**	**μ ± σ (GPa)**	**Wt %**
LMP Filament	12.2 ± 1.7	62.2	14.2 ± 2.6	22.6	26.5 ± 7.5	11.5	33.7 ± 2.4	3.7
HMP Filament	31.1 ± 4.6	64.0	40.4 ± 7.9	19.3	79.1 ± 32.5	14.0	120.2 ± 5.4	2.7
Cast (w/s = 0.3)	26.3 ± 5.4	75.8	42.0 ± 2.6	3.7	70.7 ± 25.1	13.2	105.3 ± 6.9	7.3

Table 5-3. Hardness deconvolution parameters for nanoindentation grids on 3D printed and cast specimens made with the HNC cement ink. Each grid was deconvoluted into four Gaussian distributions, with each having a characteristic mean (μ), standard deviation (σ), and weight percentage (Wt %).

	Peak 1		**Peak 2**		**Peak 3**		**Peak 4**	
	μ ± σ (GPa)	**Wt %**	**μ ± σ (GPa)**	**Wt %**	**μ ± σ (GPa)**	**Wt %**	**μ ± σ (GPa)**	**Wt %**

LMP Filament	0.9 ± 0.2	72.2	1.5 ± 0.4	15.3	4.3 ± 1.8	7.7	5.8 ± 0.5	4.8
HMP Filament	1.1 ± 0.3	70.0	1.8 ± 0.6	17.3	4.4 ± 1.6	5.8	9.2 ± 1.5	6.9
Cast (w/s = 0.3)	1.0 ± 0.3	73.3	1.9 ± 0.7	10.3	8.3 ± 2.4	13.6	9.5 ± 0.1	2.8

For Peak 1, the HNC ink HMP filament (Table 5-2) was found to have a 20% increase in mean modulus value (31.1 ± 4.6 GPa) compared to the highest mean modulus of the OPC ink HMP filaments (26.0 ± 5.0 GPa). This increase suggested that the presence of HNC provided a stiffening effect of the phases associated with Peak 1 for the HMP filament. For the LMP filament, the presence of HNC impacted the micromechanical properties differently than the HMP filament, resulting in similar behavior to the OPC ink LMP filaments, with large reductions in the Peak 1 modulus compared to the HMP filament and cast specimen. However, this effect was larger for the HNC ink LMP filament than for the corresponding OPC ink LMP filaments (61% decrease in mean Peak 1 modulus from the HMP filament, compared to 32 – 45% reductions for the OPC ink). A smaller effect was observed for the HNC ink cast specimen, for which the Peak 1 mean modulus value (26.3 ± 5.4 GPa) was within the range found for OPC ink cast specimens (23.5 – 27.8 GPa), suggesting that the HNC only had a small net impact on the average stiffness of the phases associated with Peak 1. The HNC ink HMP filament mean modulus was also much higher than that of the HNC ink cast, suggesting that the printing process affected the behavior of HNC in the microstructure.

Conversely, the Peak 1 hardness (Table 5-3) for the HNC ink HMP filament (1.1 ± 0.3 GPa) was only slightly higher than for the LMP filament (0.9 ± 0.2 GPa) and effectively the same as that for the HNC ink cast (1.0 ± 0.3 GPa) and the range of Peak 1 mean values for OPC ink HMP filaments (0.9 – 1.1 GPa). The incorporation of HNC and the printing process for the HNC ink primarily affected the stiffness (modulus) of the phase associated with Peak 1, but not their resistance to plastic deformation (hardness).

For all printed filaments, Peak 2 tended to form a right shoulder for Peak 1 on the overall distribution, between the ranges for Peaks 1 and 3, and the Peak 2 average modulus tended to move in tandem with Peak 1, with a smaller weight percentage and a larger standard deviation. For the HNC ink cast specimen, Peak 2 represented a smaller specific portion of the distribution, corresponding to a sharper peak in the 40 – 44 GPa modulus range. However, it was thought that

this result was the result of being associated with a relatively small number of indents, such that small changes in the distribution resulted in an anomalously small Peak 2 distribution.

The cast specimen experienced a reduction in modulus average for Peak 3 (70.7 ± 25.1 GPa) relative to the OPC ink cast specimens (88.1 – 106.3 GPa), but this difference was thought to be due to compensation for the anomalously small Peak 2, rather than a real reduction in modulus for the micromechanical phase associated with Peak 3. Peak 4 behavior for the cast specimen (105.3 ± 6.9 GPa) was within the OPC ink cast range (103.7 – 115.4 Gpa). The HNC ink cast specimen generally had similar hardness behavior for Peaks 3 and 4 as the OPC ink cast specimens. The HNC ink HMP filament had Peaks 3 and 4 mean modulus values (79.1 ± 32.5 GPa and 120.2 ± 5.4 GPa, respectively) that were higher than or near the top of the range previously found for the OPC filaments (47.7 – 86.3 GPa and 77.6 – 105.5 GPa, respectively), suggesting that HNC incorporation improved the phases associated with Peaks 3 and 4 for this filament. The Peak 3 average hardness for the HNC ink HMP filament experienced a significant reduction compared to the OPC ink HMP filaments (4.4 ± 1.6 GPa, compared to 6.4 – 9.2 Gpa), though Peak 4 was within the OPC ink range (9.2 ± 1.5 GPa, compared to 9.2 – 10.5 GPa). For the HNC ink LMP filament, mean modulus values for Peaks 3 and 4 (26.5 ± 7.5 GPa and 33.7 ± 2.4 GPa, respectively) were significantly reduced compared to the HNC ink HMP filament and cast specimen. The HNC ink LMP filament also experienced a significant reduction in hardness for Peaks 3 and 4 (4.3 ± 1.8 GPa and 5.8 ± 0.5 GPa, respectively) compared to the HNC ink cast specimen. As with the OPC ink LMP filaments, this effect is analogous to the downward shift in micromechanical properties caused by an increase in w/s ratio for the OPC ink cast specimens, as seen in the OPC ink specimen cast with a w/s ratio of 0.5 (Figure 3-5 and Figure 3-6). However, the presence of hydrophilic HNC particles was thought to restrict extrusion-based paste water segregation, and observations about filament extrusion qualities indicated that segregation was reduced. Therefore, additional evidence from the phase assemblage and microstructure was needed to draw firmer conclusions about this process.

5.3.3. Phase assemblage and microstructure

5.3.3.1. HNC clustering

BSE imaging revealed the presence of a distinctive phase randomly dispersed in the hydrated portion of the microstructure of the HNC cement ink (Figure 5-10a), present in both HMP and LMP filaments as well as in the cast specimen. This phase was generally larger than the other hydrated products and was approximately 25 µm in Feret diameter on average. EDS analysis (Figure 5-10b) showed that this phase was rich in Si and Al (approx. 13% and 10% by weight, respectively, Figure 5-10c) compared to the rest of the microstructure (7% and 2%, respectively), suggesting that they were clusters of HNC particles. However, the weight percentages of these clusters were less than the stoichiometric ratios for pure halloysite (22% and 21%, respectively), and there was still a significant amount of Ca within these clusters (approx. 14%, compared to 31% in the rest of the microstructure), along with some variability within and between clusters, indicating intermixing of hydration products within the clusters.

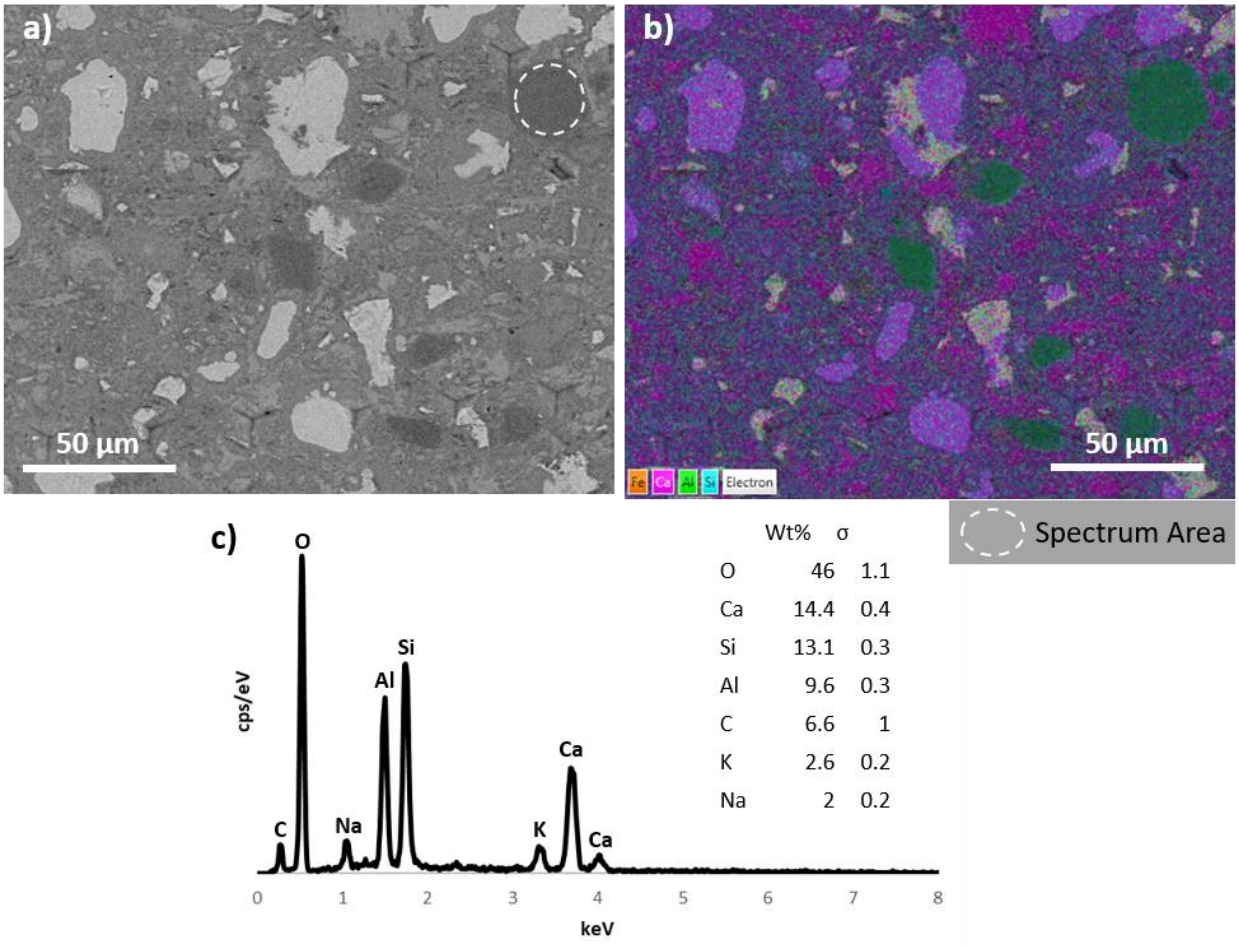

Figure 5-10. (a) BSE image of the microstructure of a filament 3D printed with the HNC cement inks, (b) EDS map of the BSE image area, and (c) an EDS spectrum of an HNC cluster with weight percentages (Wt%).

Image analysis of grid area BSE maps (4 images, 0.50 mm^2 per map; Figure 5-11) showed that these agglomerates were more prominent in the LMP filament, with 99 significant agglomerates per mm^2 (with significant being defined as having an image plane area greater than 50 μm^2) comprising 1.7% of the total area, compared to 78 agglomerates per mm^2 comprising 1.3% of the total area for the HMP filament. Therefore, there was a 24% increase in HNC clusters associated with the LMP filament compared to the HMP filament. It was thought that migration of HNC during extrusion was responsible for shifting the concentration of HNC in the microstructure, with partial clogging of the clusters in the extrusion nozzle similar to that previously described

for carbon microfibers in [183], producing regions of high and low HNC concentration (though without the propensity for extrusion discontinuities caused by the larger carbon microfibers).

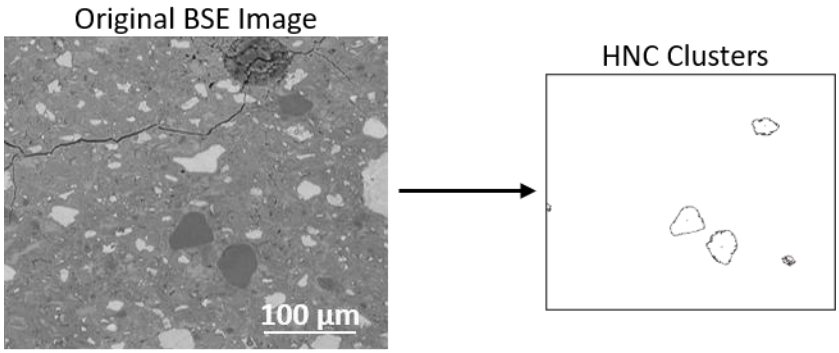

Figure 5-11. Example of image analysis showing the portion of a BSE image associated with HNC clusters.

For the cast specimen, a comparatively low number of particles (58 agglomerates per mm^2) covered a high proportion of the microstructure area (1.8%). These observations suggested that the 3D printing process played a role in breaking up HNC clusters and promoting dispersion, and that a higher proportion of the HNC in the cast microstructure were in the clustered state. Therefore, the cast specimen was believed to have a lower concentration of HNC dispersed in the microstructure than the HMP or LMP filaments.

5.3.3.2. Effect of HNC on degree of hydration

Image analysis of grid area BSE maps (Figure 5-12) revealed that the HNC ink filaments had a lower proportion of their microstructure associated with unhydrated particles (10.8 – 12.5%) compared to the OPC ink filaments (15.8 – 18.5%). The degree of hydration (α) was estimated using the Powers' Model described in [243], assuming that BSE area coverage was representative of volume fraction and specific gravities of 3.15 for the cement powder and 2.53 for the HNC [244]. Using this method, no significant effect was observed for the HNC ink cast specimen ($\alpha = 0.713$) compared to the OPC ink cast specimens (0.664 – 0.739 α-range). The HNC ink cast specimen was found to have increased clustering, thus limiting the effect of HNC on the hydration process. Therefore, these results further indicated that the cast HNC ink

specimen had a lower concentration of HNC in the dispersed state (and a higher proportion in the clustered state).

For the printed filaments, however, it was found that HNC incorporation promoted hydration, with HNC ink filaments having a range of 0.757 - 0.765 for α, compared to 0.641 – 0.693 for OPC filaments. This finding agrees with previous literature, which reported that the pozzolanic activity of the HNC fibers promotes hydration [43, 44, 245]. The largest effect was observed for the HNC ink LMP filament (α = 0.765). The HNC ink LMP filament had an increase in hydration 70% more than the HNC ink HMP filament (α = 0.727). Because dispersed HNC fibers have much greater exposed surface area to impact the cement hydration chemistry, it was thought that dispersed HNC concentration had a much more significant effect on degree of hydration. Additionally, the hydrophilic HNC fibers may have also served as reservoirs for water during curing, promoting hydration. In addition to the increase in clustered HNC, these results indicated that the LMP filament had an increase in dispersed HNC. Taken together, the increases in both states indicate a higher total concentration of HNC in the LMP filament.

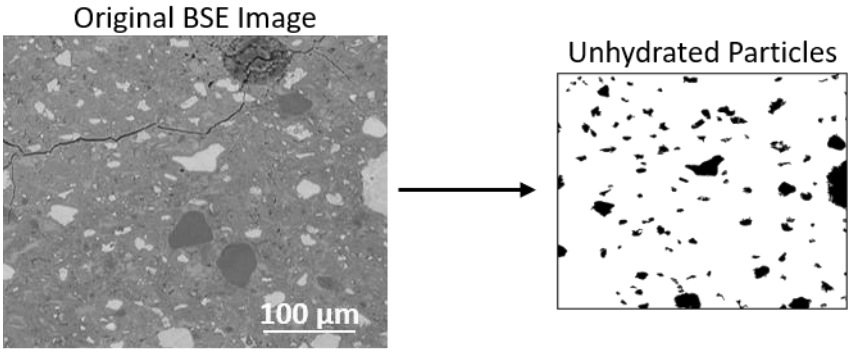

Figure 5-12. Example of image analysis showing the portion of a BSE image associated with unhydrated cement particles.

5.3.3.3. Chemical phase distribution

By comparing indent location overlaid BSE maps of grid areas with the mechanical property peaks to which each indent was most likely to belong (Figure 5-2), the microstructural features for each mechanical peak for the HNC ink was found to match the primary identities previously

established for the OPC ink: Peak 1 – hydrated phases (including HNC clusters), with mean values similar to the median values of the microstructure, suggesting primary control of the overall mechanical response; Peak 2 – composite indents on phase edges and high stiffness hydrates; Peaks 3 and 4 – unhydrated particles. For this analysis, indents belonging to Peak 1, associated with the hydrated portion of the microstructure and HNC clusters, were considered.

For the HNC ink filaments and cast specimen, 3 – 4% of the hydrate indents were associated with HNC clusters, 14 – 19% were associated with Al rich phases. The majority of the hydrate indents of the 3D printed filaments and cast cement pastes (66 - 76%; Table 5-4) exhibited a chemical composition that corresponded to mixtures of C–S–H and CH (mostly C–S–H or mostly CH).

The HNC cluster indents were found to have a wide variety of chemical makeups in addition to high Al/Ca and Si/Ca ratios, further evidencing the presence of a variety of hydration products within assemblages of HNC fibers (Figure 5-13). However, when considering whole clusters, the sum EDS spectra were very similar (Figure 5-10c), suggesting that that there was some consistency to hydrate intermixing with HNC clusters at larger scales. Additionally, the proportion of indents associated with HNC clusters was consistently higher (3 – 4%) than the area coverage calculated by image analysis (1 – 2%), suggesting that clusters which were smaller than those considered ‘significant’ in the image analysis procedure were also present.

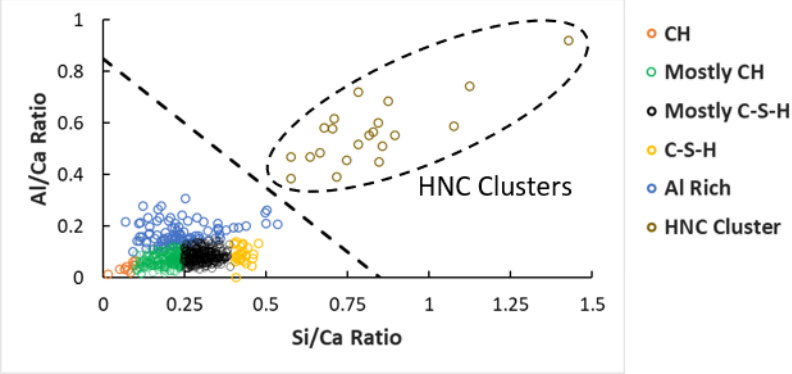

Figure 5-13. Segmentation of indents associated with hydrates by chemical composition using SEM-EDS analysis, showing an additional phase representative of the HNC clusters for the HNC ink.

Al rich hydrate phases were found to be more prevalent for filaments printed with the HNC ink compared to the OPC ink filaments. Removing indents associated with HNC clusters from consideration, 15 – 20% of indents in HNC ink filaments were categorized as 'Al Rich' (Table 5-4), compared to 5 – 10% of indents for OPC ink filaments. This result is likely due to a combination of indenting on phases that include dispersed HNC fibers – which are comparatively high in Al, and increased formation of aluminate hydrate phases due to increased availability of Al from the HNC fibers. The HNC ink LMP filament had the highest proportion of Al rich indents (20%) compared to the HNC ink HMP filament (16%) and the HNC ink cast specimen (15%). In addition to the changes in cluster prevalence and degree of hydration previously discussed, this further indicated the HNC ink LMP filament having the highest concentration of dispersed HNC in its microstructure, and the HNC ink cast specimen having the lowest. Several of the Al rich indents in the HNC ink LMP filament were near the (Al + Si)/Ca cutoff to be categorized with the HNC clusters (Figure 5-14). However, most of these indents were observed to not be part of a significant HNC cluster, suggesting that smaller HNC clusters or regions rich in dispersed fibers were also interspersed in the microstructure for the LMP filament.

The proportion of indents associated with mixed phases (mostly CH and mostly C-S-H) for the HNC ink filaments and cast specimen (66 – 76%) was smaller than for the OPC ink (76 – 84%). However, this difference was because a larger proportion of indents were associated with Al rich phases and HNC clusters, rather than a reduction in CH/C-S-H mixing. Among CH, mostly CH, mostly C-S-H, and C-S-H indents, 86 – 94% of indents were associated with mixed phases for the HNC ink, compared to 87 – 89% for the OPC ink.

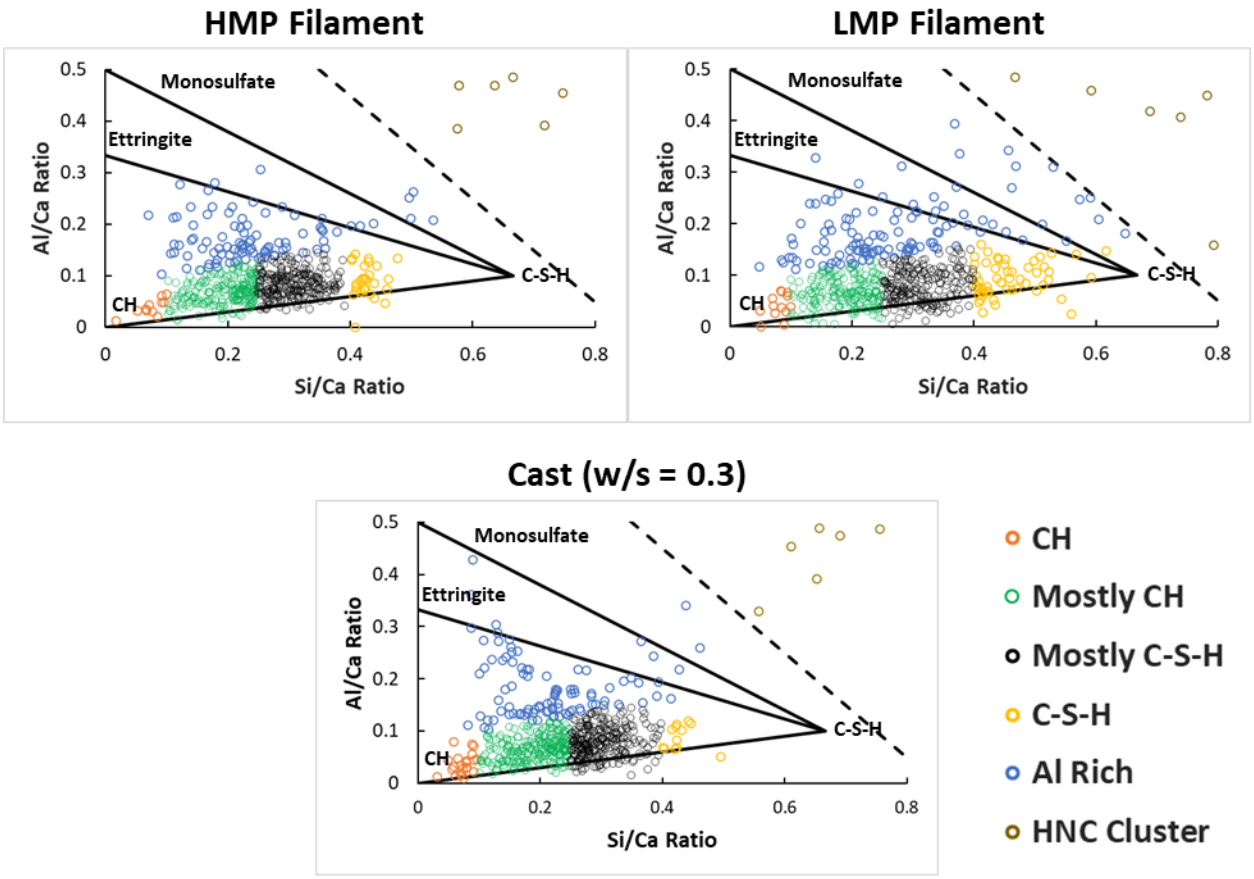

Figure 5-14. Segmentation of indents associated with hydrates by chemical composition using SEM-EDS analysis for filaments and cast HNC ink specimens (rescaled compared to Figure 5-13 to focus on non-HNC Cluster indents).

Table 5-4. Percentage of indents in each chemical phase category from SEM-EDS for the HNC ink.

	Low-Al Phases				High-Al Phases	
	Primarily CH		Primarily C-S-H			
	CH	Mostly CH	Mostly C-S-H	C-S-H	Al Rich	HNC Cluster
LMP Filament	2.1	31.1	34.7	8.7	19.1	4.3
HMP Filament	1.8	35.6	39.4	4.4	15.4	3.4
Cast (w/s = 0.3)	3.4	35.1	41.0	1.8	14.6	4.1

5.3.3.4. Pozzolanic activity of HNC

Pozzolanic activity was evidenced within the HNC ink specimens, converting CH into C-S-H. Since the dispersed fibers had a much greater exposed surface area to react with the hydrated matrix, they were thought to be primarily responsible for this reactivity. For indents associated with low-Al phases (i.e., 'CH', 'Mostly CH', 'Mostly C-S-H', and 'C-S-H'), the HNC ink filaments had a higher proportion of primarily C-S-H phases ('C-S-H' + 'Mostly C-S-H') at the expense of primarily CH phases ('CH' + 'Mostly CH'). For HNC ink filaments, 54 – 57% of low-Al indents were primarily C-S-H (Table 5-4), and 43 – 46% were primarily CH, compared to 43 – 48% and 52 – 57%, respectively, for the OPC ink filaments.

The LMP filament evidenced the greatest degree of pozzolanic activity, with a higher proportion of 'primarily C-S-H' indents than the HMP filament (57.0%, compared to 54.0% for the HNC ink HMP filament and 45.0% on average for OPC ink filaments). This change represented a 30% increase in converting 'primarily CH' phases to 'primarily C-S-H' phases. This effect was smaller for the cast HNC ink specimen (52.6%, compared to 48.8% on average for OPC ink cast specimens), further indicating that the printing process contributed to breaking up HNC clusters and dispersing HNC in the microstructure. The pozzolanic activity could also be seen from the clear trend of increasing average Si/Ca ratio among the low Al phase indents: 0.273 for the LMP filament, 0.260 for the HMP filament, and 0.247 for the cast specimen (Figure 5-14).

The increase in 'primarily C-S-H' and Al rich phases for the HNC ink LMP filament provided further evidence of reactivity of the individual HNC fibers. As the external siloxane surface of the HNC fibers contributed to the pozzolanic reaction increasing the primarily C-S-H phases, the internal aluminol surface reacted with other hydrates to form aluminate phases. A low degree of reactivity would result in an increase in indent locations with high Si and high Al regions corresponding to unreacted fibers, instead of the observed increase in average Si concentration in low-Al phases and an increase in the prevalence of high-Al phases. As such, the LMP filament had the highest proportion of Al rich indents and 'primarily C-S-H' indents corresponding to the most HNC activity and the most dispersed HNC, while the cast HNC ink specimen had the least of each among the HNC ink specimens.

However, coupled nanoindentation and ESEM/EDS did not provide a complete picture of CH in the microstructure due to the high degree of hydrate phase mixing and the higher nanoindentation failure rate on 'pure' CH phases (Figure 3-9). Therefore, TGA was also used to measure the amount of CH in the microstructure. However, because TGA required powdered samples that were homogenized from the whole of a printed or cast specimen, only the net effect of 3D printing and HNC incorporation could be measured, not the differences associated with changes in HNC concentration and clustering in HMP and LMP filaments. TGA results (Table 5-5) further revealed that HNC incorporation resulted in a reduction in CH in 3D printed and cast specimens relative to their OPC ink counterparts. However, a larger reduction in CH was observed between the 3D printed and cast specimens. The TGA results indicated a reduction in CH associated with printing for both the HNC ink and OPC ink. This was in contrast with the EDS signatures (Table 5-4) of the indents, which only showed a reduction in CH associated with printing for the HNC ink. The HNC's pozzolanic activity pushed many indents in the printed filaments that were borderline between 'mostly CH' and 'mostly C-S-H' into the 'mostly C-S-H' category, despite the overall conversion rate of CH to C-S-H associated with pozzolanic activity being smaller than that associated with the printing process.

3D printing also resulted in an increase in $CaCO_3$ for both cement inks. It was thought that this increase was caused by the increase in surface area associated with filament deposition compared to casting, since carbonation is a diffusion-limited reaction with carbon dioxide. HNC incorporation did limit carbonation relative to the OPC ink, likely by reducing the available CH through pozzolanic activity.

Table 5-5. Mass percentage of calcium hydroxide (CH) and calcium carbonate ($CaCO_3$) as determined by TGA for specimens 3D printed (3DP) and cast with each cement ink.

Specimen Type	CH mass %	$CaCO_3$ mass %
HNC ink 3DP	13.7	3.2
HNC ink Cast	14.7	2.8
OPC ink 3DP	14.2	3.4
OPC ink Cast	14.9	3.0

5.3.3.5. Effect of HNC on microporosity

The presence of HNC impacted the micropore characteristics of the HNC ink filaments and cast specimen. Much of the microstructure had an apparent reduction in pores that were 3 – 8 μm in Feret diameter compared to the OPC ink filaments. However, there were also regions of the HNC ink microstructure that had an increase in pores in this size range (Figure 5-15). These regions of high microporosity were often associated with the area surrounding larger pores and varied in size but were generally smaller than 1 mm in diameter. Areas of very high microporosity were generally not found to be suitable for nanoindentation and so were avoided for grid location selection. However, there was a significant variation in microporosity found in the indentation areas for both the HMP and LMP filaments, as well as for the cast specimen. Consequently, changes in mechanical property distributions could not be directly related to changes in the pore structure at this 3 – 8 μm size range. However, HNC incorporation clearly impacted the pore structure, and it was believed that HNC also impacted the nanopore structure and mesopore structure that controlled the microstructural arrangements of the hydrates and their micromechanical properties.

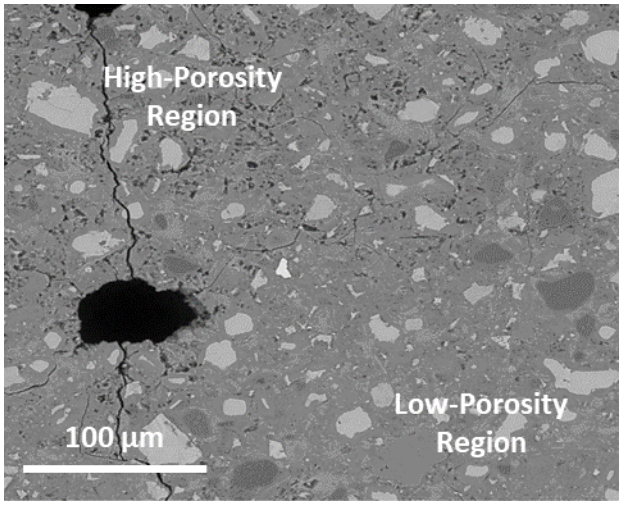

Figure 5-15. Regions of high and low microporosity in the microstructure of the 3D printed HNC ink specimen.

5.3.4. Chemo-mechanical coupling

5.3.4.1. Coupling nanoindentation and chemical information from ESEM/EDS

The range of indentation modulus values of the morphological categories of the hydrate phases within HNC ink filaments and cast specimen were, overall, more similar to each other than to the corresponding categories in dissimilar filaments. That is, changes in mechanical properties between filaments and cast specimens were primarily caused by the same morphological categories having different mechanical properties, rather than proportions changing for morphological categories that had relatively constant properties (Table 5-6). This "homogenization" of the mechanical properties within the filaments indicated that the change in micromechanical properties between LMP and HMP filaments was likely caused by changes to the microstructural arrangement of the hydration products, rather than changes in the relative proportions of the chemical phases.

For the HMP filament and cast specimen, the HNC cluster indents had a significant reduction in modulus values compared to other chemical phases, as agglomerations of largely unreacted fibers with interspersed hydration products were less densely packed and had lower mechanical properties than other phases. However, for the LMP filament, the HNC cluster indents were within the range reported for other phases, suggesting that this effect was less pronounced when the entire microstructure had lower stiffness.

The hardness distributions for each morphological category generally had much smaller changes than the modulus values both between categories within filaments and between filaments within the same category (Table 5-7). This result was in agreement with previous findings for the OPC ink, that the changes in hydrated phase packing density, which is responsible for large difference in elastic response (modulus) generally has a much smaller impact on plastic response (hardness). However, it can be observed that there was a reduction in hardness for the HNC clusters in the cast specimen. It is thought that this was caused by the greater size of the clusters in the cast specimen compared to the 3D printed filaments. These larger clusters had higher volume-to-surface area ratios, allowing them to behave more differently than the surrounding hydrate matrix and have reduced plastic responses. Beyond the shifting average values and standard deviations, the incorporation of HNC seemed to have little effect on the shape of the distribution for each phase (Figure 5-16).

Table 5-6. Average modulus values (± σ, in GPa) for each chemical phase categorization for the HNC ink.

	Low-Al Phases				High-Al Phases	
	Primarily CH		Primarily C-S-H			
	CH	**Mostly CH**	**Mostly C-S-H**	**C-S-H**	**Al Rich**	**HNC Cluster**
LMP Filament	12.8 ± 1.4	12.0 ± 1.4	12.3 ± 1.7	12.4 ± 1.5	12.0 ± 1.5	12.4 ± 1.1
HMP Filament	34.8 ± 3.5	32.1 ± 4.5	31.2 ± 4.2	30.6 ± 3.9	31.3 ± 4.1	29.3 ± 4.4
Cast (w/s = 0.3)	26.9 ± 5.9	26.9 ± 4.9	26.6 ± 4.7	24.2 ± 5.2	25.9 ± 5.1	21.4 ± 4.5

Table 5-7. Average hardness values (± σ, in GPa) for each chemical phase categorization for the HNC ink.

	Low-Al Phases				High-Al Phases	
	Primarily CH		Primarily C-S-H			
	CH	**Mostly CH**	**Mostly C-S-H**	**C-S-H**	**Al Rich**	**HNC Cluster**
LMP Filament	1.1 ± 0.2	0.9 ± 0.2	0.9 ± 0.2	1.0 ± 0.2	0.9 ± 0.2	1.0 ± 0.1
HMP Filament	1.3 ± 0.3	1.1 ± 0.3	1.1 ± 0.2	1.0 ± 0.2	1.1 ± 0.3	1.1 ± 0.3
Cast (w/s = 0.3)	1.1 ± 0.4	1.1 ± 0.3	1.1 ± 0.3	1.0 ± 0.3	1.0 ± 0.3	0.8 ± 0.3

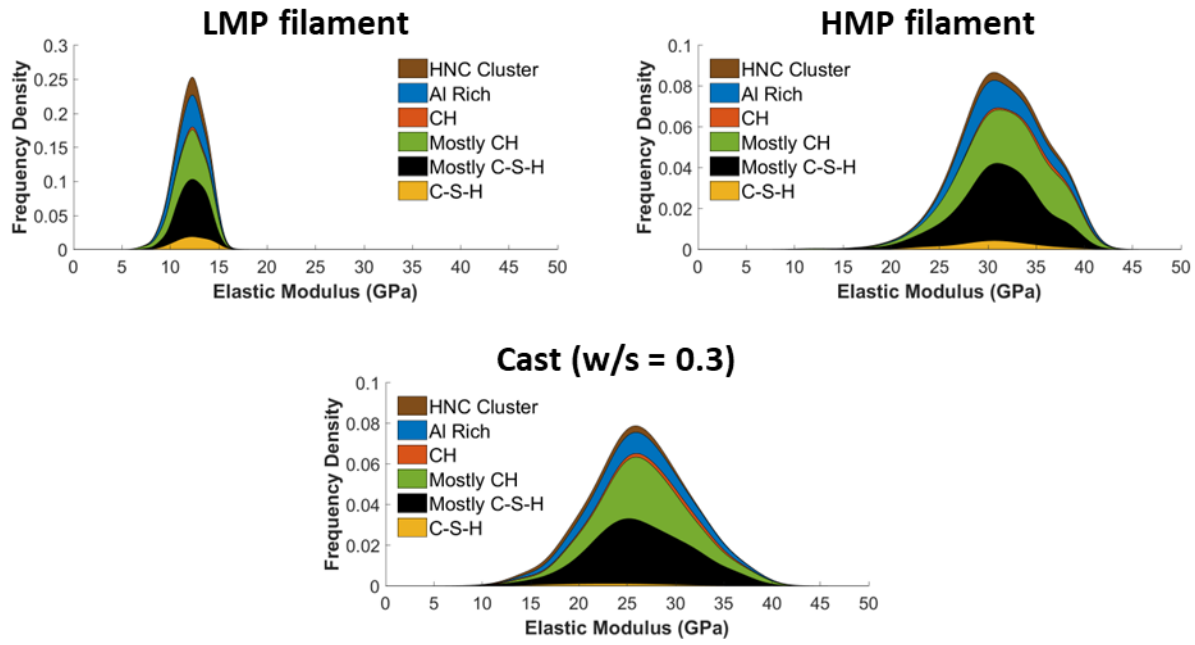

Figure 5-16. Modulus experimental probability distribution functions of hydrate indents for 3D printed filaments and cast cement pastes made with the HNC ink, distinguished by chemical phase classification.

5.3.4.2. C-S-H phase distribution

While the hydrated microstructure was primarily mixed C-S-H and CH phases, further refinement of the EDS segmentation showed that the incorporation of HNC also impacted the behavior of indents identified as 'pure' C-S-H. Examining only the indents identified as 'C-S-H' and categorizing by stiffness into categories of packing density based on previously reported literature of cementitious materials with similar w/s ratios, the following C-S-H phases were defined: loosely-packed (LP; modulus less than 15 GPa), low-density (LD; 15-28 GPa), high-density (HD; 28-37 GPa), and ultra-high-density (UHD; greater than 37 GPa) [180, 181, 187-192].

For the HNC ink LMP filament moduli, most of the C-S-H distribution (88%) was in the LP category, a distinctive downward shift compared to the OPC ink LMP filament, which had only 4% LP C-S-H and 96% LD C-S-H. The HNC ink LMP filament modulus distribution was also significantly compressed compared to the HNC ink HMP filament and cast specimen.

Conversely, the HNC ink HMP C-S-H stiffened compared to the OPC ink HMP filament, with 67% of its modulus distribution being HD C-S-H, compared to only 36% HD C-S-H in the OPC ink. The cast specimen was similarly distributed, but with a wider distribution and with a less normal distribution likely caused by the low number of pure C-S-H indents (Figure 5-17). As with the whole hydrated microstructure, HNC incorporation caused a significant densification of C-S-H for the HMP filament and a loosening of C-S-H for the LMP filament relative to their OPC ink counterparts.

Hardness distributions for C-S-H further illustrated the insensitivity of plastic response to the changes in hydrate packing density, which affected the elastic response (Figure 5-18). The hardness distributions for the HNC ink LMP and HMP filaments were very similar in shape and location. For the HNC cast hardness values, the distribution was slightly more spread and less normally distributed. However, this result may have been skewed by the small number of indents associated with pure C-S-H for the cast specimen.

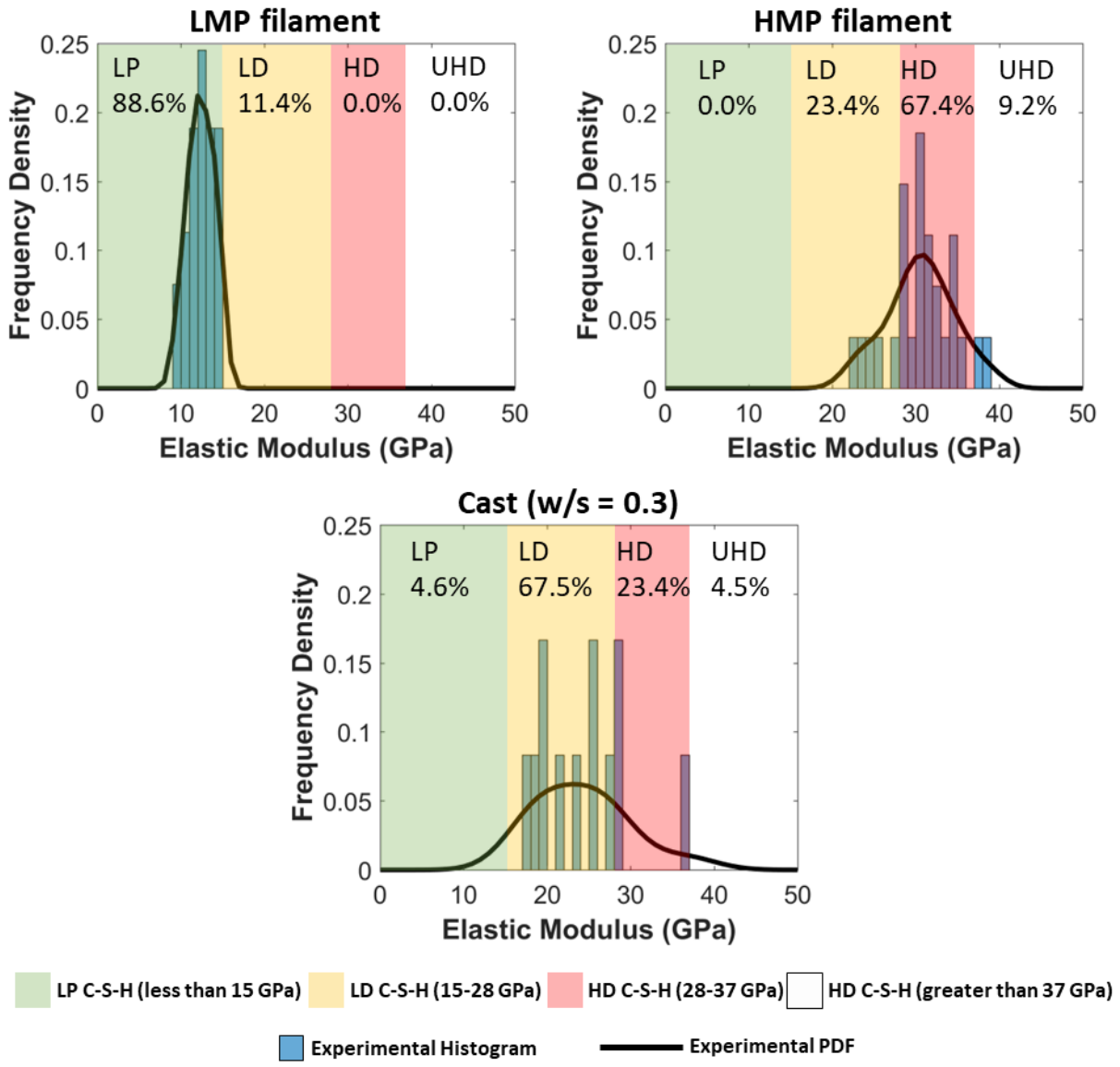

Figure 5-17. Modulus PDFs for indents categorized as "pure" C–S–H based on EDS and nanoindentation data for the HNC ink. Modulus ranges for C–S–H categories are based on typical values reported in the literature for loosely packed (LP), low-density (LD), and high-density (HD) C–S–H.

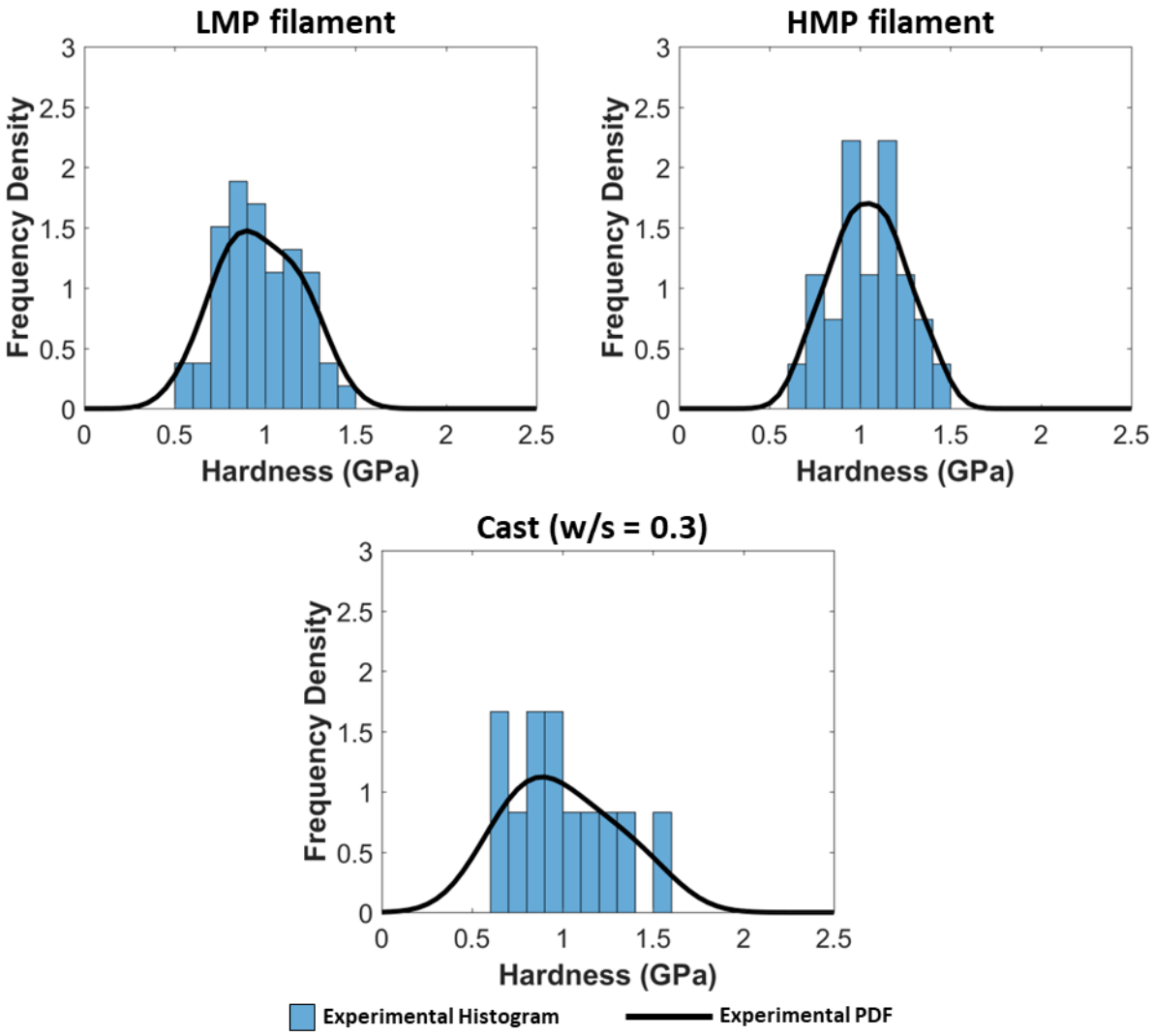

Figure 5-18. Hardness PDFs for indents categorized as "pure" C–S–H based on EDS and nanoindentation data for the HNC ink.

5.3.5. Influence of HNC incorporation on chemo-mechanical behavior

Overall, there was evidence of HNC incorporation's impact on the pore structure, of changes in clustered and dispersed HNC associated with the formation of HMP and LMP filaments and the cast specimen, and major changes in micromechanical properties associated with those changes. Changes in the mesostructure (*approx.* 100 nm) and microstructural arrangement of hydrate phases have been previously reported to play a significant role in determining micromechanical

properties, with higher modulus being associated with higher hydrate density [195, 205, 217-221]. Therefore, the driving force for the changes in micromechanical properties was attributed to local concentration and clustering behavior of HNC within a given filament.

For the LMP filament, which evidenced the highest concentration of HNC in the dispersed and clustered states (based on cluster frequency, degree of hydration, and pozzolanic activity), the presence of HNC was found to be detrimental to the stiffness of hydration products. The presence of too many HNC particles and clusters effectively interrupted the formation of the matrix of hydration products, resulting in lower packing density, an increase in loosely-packed C-S-H, and outweighing the effects of pozzolanic activity and pore-filling. Additionally, the hydrophilic HNC particles were thought to migrate with their absorbed water, and the pore spaces of the less densely packed filament were thought to be saturated with water due to the 100% humidity curing conditions. Consequently, the LMP filament was thought to effectively have an elevated w/s ratio, which may have also contributed to the increase in degree of hydration. This effective increase in w/s ratio caused an analogous effect of the increased w/s ratio in the OPC ink LMP filaments unhydrated cement particles. For both cement inks, the LMP filaments had significantly reduced mean modulus and hardness values for Peaks 3 and 4, associated with unhydrated particles, compared to the cast specimens. In both cases, this reduction was attributed to an increase in local w/s ratio (or an effective increase in local w/s ratio for the HNC ink). This increase in local w/s ratio allowed for an increased effect of the shear stresses of the extrusion process, contributing to the partial dissolution of the unhydrated particles and reducing their micromechanical properties.

For the HMP filament, which evidenced lower clustered and dispersed HNC concentrations, HNC's presence was beneficial to the microstructural arrangement of hydration products, with pozzolanic activity and pore-filling effects resulting in a densified matrix of hydration products with an increase in high-density and ultra-high-density C-S-H. Therefore, it was believed that there exists a concentration for dispersed HNC below which the presence of HNC improves the micromechanical properties through the mechanisms attributed to it in previous literature: densifying the microstructure as nano-filler and increasing degree of hydration through pozzolanic activity and calcium aluminosilicate formation [43, 44, 245]. The HMP filament, which was shown to have less HNC than the LMP filament, had a concentration below the

threshold concentration and therefore experienced significantly enhanced micromechanical properties. Additionally, the HMP filament did not have a reduction in mean modulus for Peak 3 analogous to the reduction caused by partial unhydrated particle dissolution from shear stress during extrusion for the OPC ink HMP filament. However, there was a significant reduction in mean hardness for Peak 3 relative to the cast specimen. These results suggested that the HNC incorporation limited the effect of the shear stresses on the elastic modulus for the HMP filament, but not on the hardness.

The HNC cast specimen, which did not experience extrusion pressure and filament formation to aid in HNC dispersion, was found to have comparatively little HNC dispersed in its microstructure. Consequently, the impact of HNC incorporation on the microstructure was comparatively small, and the HNC cast specimen had micromechanical properties similar to those observed for the OPC ink cast specimens.

5.3.6. Macromechanical properties

5.3.6.1. Compressive strength

The effect of the interaction between HNC incorporation and the 3D printing process was evidenced by the difference in compressive strength between the specimens 3D printed and cast with the HNC ink. The 3D printed samples with the HNC ink were found to be significantly stronger than their cast counterparts (at 95% confidence), having 60% higher strength on average (Figure 5-19a). Meanwhile, the specimens printed and cast with the OPC ink were not found to have significantly different strength. Additionally, the HNC ink cast specimens were significantly weaker than their OPC ink cast counterparts. It was thought that the increase in HNC clusters in the cast specimens, which were found to have lower micromechanical properties than the rest of the microstructure on average and may have introduced origin points for microcracks through weak interfaces between clusters and other hydrate phases, were primarily responsible for this reduction in strength.

In contrast, the printed HNC specimens, which were found to have more dispersed HNC in the microstructure, had very similar strength as the printed OPC ink specimens on average. The HNC and OPC inks were found to have different behaviors at the filament and micromechanical levels, with the HNC ink contributing to an increase in microscale stiffness for HMP filaments

and a decrease for LMP filaments, and with the HNC ink filaments having more consistent extrusion qualities. However, these differences were found to effectively negate each other at the macroscale. Still, the effects of the HNC in the 3D printed specimens could be seen in the variance of the compressive strength, with the standard deviation being reduced by 65% with the incorporation of HNC. Despite the HNC ink's improvement in printing quality, the HNC ink did not have an improvement in average compressive strength. This result suggests that, on average, the HNC reduced the load carrying capacity of the filaments on average. Therefore, the reduction in stiffness for the LMP filaments had a larger effect on macroscale strength than the improvement for the HMP filaments relative to the OPC ink. The OPC ink's higher variability in printing quality resulted in a larger range for compressive strength, with high quality prints being stronger than the HNC specimens by having filaments which combine to have higher load carrying capacity, but with lower quality prints being weaker due to voids and underextrusion errors.

Compressive modulus results (Figure 5-19b) were found to be similar to those for compressive strength, with the HNC printed structures being statistically stiffer than their cast counterparts and similar to the OPC ink printed specimens, though with less variance. This result suggests that the mechanism for the changes in load carrying capacity measured by compressive strength are related to those of changes in elastic behavior as measured by compressive modulus.

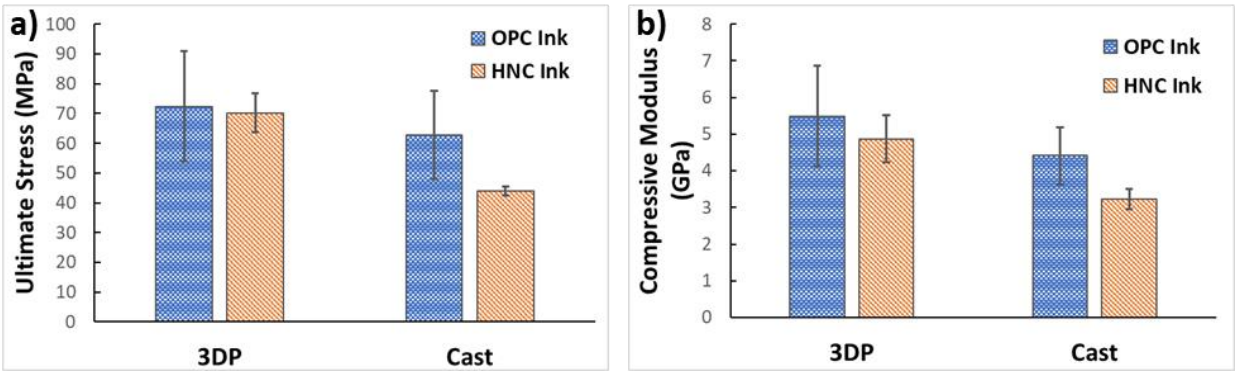

Figure 5-19. (a) Average compressive strength and standard deviation for each specimen type; (b) average compressive modulus and standard deviation for each specimen type.

5.3.6.2. Flexural Strength

For both the HNC and OPC cement inks, the 3D printed specimens were found to have a reduced flexure strength (measured as modulus of rupture as calculated by ASTM C239) compared to the cast samples (Figure 5-20a). For the HNC ink, the 21% average reduction in modulus of rupture was significant at 95% confidence, and the 17% average reduction for the OPC ink was significant at 90% confidence. These results were not consistent with previous literature, which has shown an increase in flexure strength of 3D printed specimens tested in similar orientations compared to cast specimens [79, 80], though it is consistently pointed out that these properties are dependent on the specifics of the printing parameters and ink formulation. There was no statistically significant difference between the two ink formulations for the 3D printed or cast specimens, though small increases for the 3D printed and cast HNC ink specimens suggested that there may have been some internal reinforcement benefit conferred by the HNC fibers. As with the compressive strength, the HNC ink 3D printed samples had a reduced variance compared to the OPC ink 3D printed samples (45% lower standard deviation). This reduction is in agreement with the observations of improved rheology and printing consistency, and of the fracture surfaces having smaller macropores for the HNC ink filaments than the OPC ink filaments (Figure 5-6).

Conversely, Young's modulus was found to be higher for the 3D printed specimens of both ink types compared to their cast counterparts (Figure 5-20b). The 58% increase for the HNC ink was significant at 95% confidence, and the 19% increase for the OPC ink was significant at 90% confidence. It is hypothesized that the previously suggested alignment of the oblate C-S-H globules in the direction of printing (Figure 3-13) may have increased the stiffness of the filaments in flexure compared to the cast specimens, though not improved ultimate strength as measured by modulus of rupture. This hypothesis is strengthened by the analogous micromechanical results showing that this alignment primarily affected elastic behavior (indentation modulus at the microscale and Young's modulus at the macroscale), but not plastic behavior (hardness at the microscale and flexural strength at the macroscale). This effect was further evidenced by the absence of a slight strain-stiffening effect in the 3D printed specimens which was present in the cast specimens (Figure 5-20c). The additional increase in Young's modulus between 3D printed and cast specimens associated with the incorporation of HNC may

also be caused by the potential alignment of the fibrous HNC particles in the direction of printing.

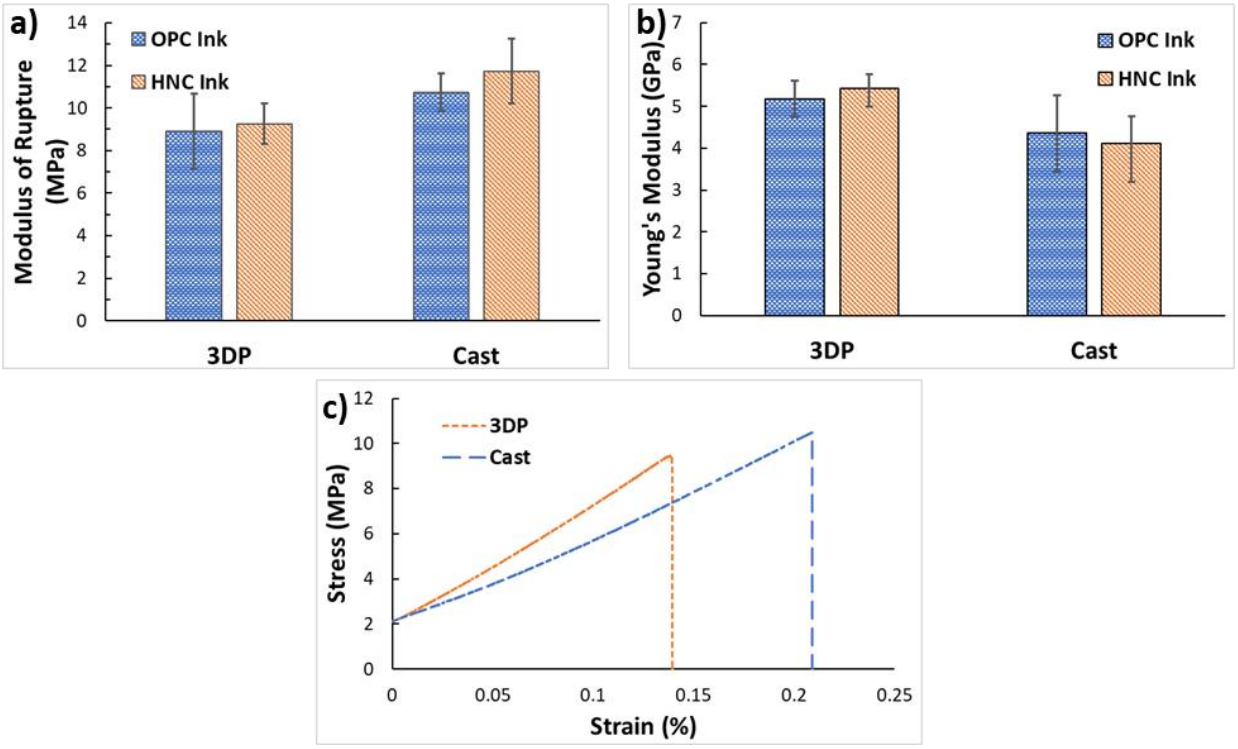

Figure 5-20. (a) Average flexural strength (modulus of rupture) and standard deviation for specimens 3D printed and cast with each cement ink; (b) average Young's modulus and standard deviation for each specimen type; and (c) representative stress/strain curves for 3D printed and cast samples with the HNC ink.

5.4. Conclusions

The effects of replacing 5% of cement with halloysite nanoclay (HNC) in 3D printing cement inks on filament behavior was assessed through observations of filament morphology, statistical grid nanoindentation paired with ESEM/EDS mapping, TGA, and macromechanical testing. Based on the presented results, the following conclusions can be drawn:

- HNC incorporation improved the ink printability, reducing underextrusion and discontinuity printing errors, extrusion pressure-driven segregation, and observed macropore size.
- The HNC ink was found to form high and low mechanical property filaments. This effect was thought to be caused by dynamic changes in HNC clustering and concentration distribution during the printing process.
- Micromechanical properties were increased by HNC incorporation in HMP filaments and reduced in the LMP filament relative to the cast specimen and the OPC ink. Cast specimens were found to have similar micromechanical properties for both inks.
- The 3D printing process was found to contribute to reducing HNC clustering, with the LMP filament having higher concentration of dispersed HNC fibers, interrupting hydrate matrix formation and contributing to a more loosely packed microstructure, while HMP filaments had a lower HNC concentration and were densified by its incorporation.
- HNC incorporation did not significantly affect the average macromechanical properties in 3D printed specimens compared to the OPC ink, but 3D printed HNC specimens were found to greatly reduce variance in properties. Meanwhile, HNC incorporation contributed to reduced compressive strength for the cast specimens.

These findings suggest that replacing 5% of cement with HNC can significantly influence the behavior of printed filaments and structures, and that HNC incorporation could lead to improved performance in some applications. Further work should be done to optimize the concentration and dispersion of HNC.

CHAPTER 6

EFFECTS OF INTERNAL ARCHITECTURE AND INK COMPOSITION ON THERMAL BEHAVIOR OF 3D PRINTED CEMENT PASTES AND HALLOYSITE NANOCLAY CEMENT COMPOSITES

The results of this chapter are being incorporated into the following manuscript:

Kosson M., Brown L., and Sanchez F. Effects of Internal Architecture and Ink Composition on Thermal Behavior of 3D Printed Cement Pastes and Halloysite Nanoclay Cement Composites. Expected submission August 2022.

6.1. Overview

For this study, the effect of internal architecture and HNC incorporation on the thermal behavior of 3D printed cement-based beams was investigated. Three internal architectures created by using different infill patterns were utilized: rectilinear, 3-dimensional honeycomb, and Archimedean chords. Solid cast beams were used as a reference comparison. Cement inks with and without 5% cement replacement with HNC were compared. The beam thermal behavior was characterized by using a novel approach that integrates a thermal conduction experimental setup for real-time infrared thermal imaging and a conceptual 1-dimensional heat transfer fin model for calculating the effective thermal conductivity of 3D printed beam with complex internal architectures.

6.2. Materials and Methods

6.2.1. Materials

The materials discussed in Section 3.2.1 were used in this study including Type I/II portland cement, the polycarboxylate-based high-range water reducer (MasterGlenium 7700), the viscosity-modifying admixture (MasterMatrix VMA 362), and the anti-washout admixture (MasterMatrix UW 450). Halloysite nanoclay (HNC) (Sigma-Aldrich, USA), which has a needle-like structure that is 30-70 nm in diameter and 1-3 μm in length, was used to affect the thermal capacity and hardened mechanical properties, and to control of the rheology and setting time of the cement pastes.

6.2.2. Cement composite preparation

6.2.2.1. Cement ink design and preparation

Two cement inks were used: a 'neat' cement paste ink (OPC ink) and an ink, which had 5% of the OPC replaced with HNC (HNC ink). Both inks had a 0.3 water-to-solid (w/s) ratio, 0.9% VMA 362 (per mass of solids), 0.35% Glenium 7700 (per mass of solids), and 1.0% UW 450 (per mass of solids). These ink designs provided adequate ink qualities for consistent printability in preliminary testing and were within the manufacturer's recommended dosages for admixtures [169-171].

The admixtures were added to the water and sonicated using a 500 W probe sonicator (Fisher Scientific Model 505 Sonic Dismembrator, Hampton, NH, USA) for 20 s at 50% power amplitude. When applicable, HNC powder was added to the OPC powder and stirred until visibly homogenous. Then, the HNC/OPC powder combination was mixed for 1 min at 400 RPM with a stainless-steel paddle bit in a mounted corded drill with rotation speed controlled by a DC motor. The homogenized water/admixture mix was added to the HNC/OPC powder and mixed for 1 min with rotation speed ramping up from 400 RPM to 1000 RPM, followed by 2 min at 1000 RPM.

6.2.2.2. Preparation of 3D printed and cast cement beams

All 3D printed cement beams were printed using a Hydra 430 gantry model 3D printer with EMO-XT modular 3D print heads (Hyrel 3D, Norcross, GA, USA). An .STL file for a beam measuring 90 mm long, 28 mm wide, and 14 mm high was generated, and slicing recipes with one vertical perimeter layer, no horizontal perimeter layers, a layer height of one mm, and three infill patterns were produced using Slic3r slicing software (Italy). The three infill patterns with 30% infill and a variety of filament pathways and void structures for heat conduction were selected to demonstrate the effect of different internal architectures on thermal properties: rectilinear (RL) – such that each successive layer was printed in an orthogonal alignment from the previous layer; 3-dimensional honeycomb (3DHC) – such that the extrusion produces interlocking hexagonal voids; and Archimedean chords (AC) – such that the extrusion pattern spirals outward from the center of the sample (Figure 6-1).

The OPC cement ink was manually loaded into the 3D print head. A vibrating table was used to aid loading with the HNC ink, which was more viscous than the OPC ink. Tamping with a 1.6 mm diameter stainless-steel rod mitigated air bubbles. Samples were 3D printed 14 layers high, which yielded a beam-shaped sample that was *ca.* 90 mm long, 28 mm wide, and 14 mm high. Three replicates were printed for each internal architecture and cement ink, totaling eighteen 3D printed samples.

As a control, each cement ink was also cast into beam-shaped silicon molds and tamped with a 1.6 mm stainless-steel rod to produce solid beams measuring 90 mm long, 28 mm wide, and 14 mm high. Three replicates of each cement composite type were cast. All beams were aged for 35 days in a curing chamber before characterization.

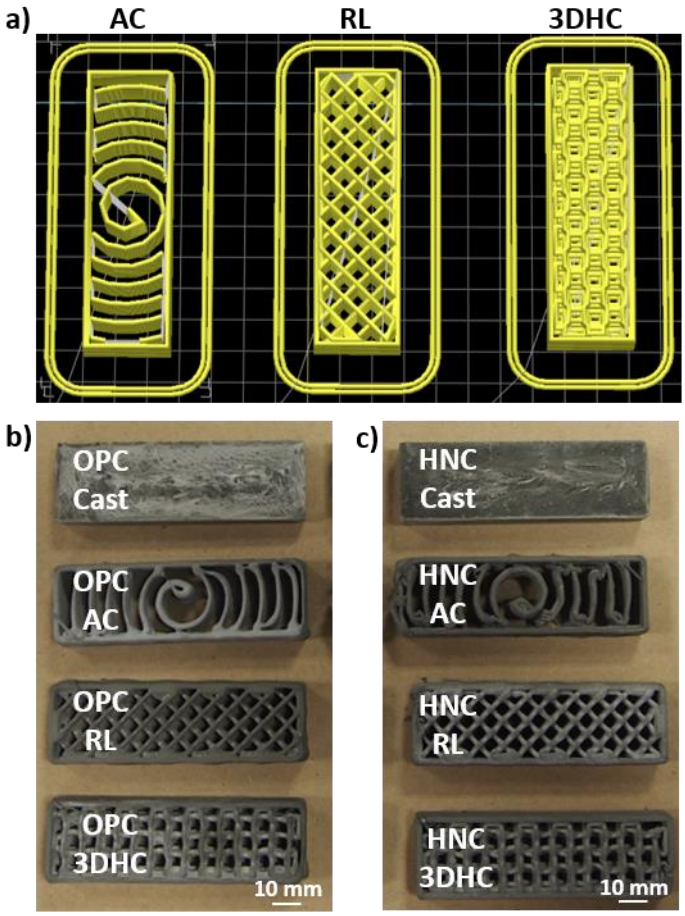

Figure 6-1. (a) Tool-path schematics of the infill patterns utilized for 3D printed beams to alter internal architecture: Archimedean Chords (AC), Rectilinear (RL), and Three-Dimensional

Honeycomb (3DHC); and cast and 3D printed specimens for each architecture made with (d) the OPC ink and (e) the HNC ink.

6.2.3. Thermal measurements

To measure differences in thermal conduction resulting from variations in ink composition and internal architecture, an experimental setup was designed where a thermal conductor (aluminum) in contact with a heating element at 60 °C was applied to one end of a 3D printed or cast beam (test beam). Refractory bricks were utilized to insulate the bottom and sides of the beam as well as provide a layer of separation between the beam and the heating element (Figure 6-2a). A FLIR A8300sc MWIR performance infrared camera was mounted above the sample to track temperature progression during testing (Figure 6-2b). An insulating rubber pad was placed above the exposed portion of the conductor to mitigate the effect of the conductor on IR images. The conductor was allowed to preheat to steady-state before testing, with the surface to be exposed to the test sample registering between 40.0 and 40.5 °C with the infrared camera. Test samples were coarsely sanded on the sides to reduce printing heterogeneity and were allowed to equilibrate to room temperature, then exposed to conductive heating for 120 minutes. The entire test setup was surrounded by acrylic sheets to minimize the effect of small differences in the room temperature and air flow on the test setup.

Thermal images were collected at ten-second intervals for the duration of testing. Image resolution was set to 1130 x 490 pixels. Cursors were placed in six locations near the centerline of each sample (Figure 6-2c) for temperature monitoring using the infrared camera software, with average temperature for a nine-pixel square recorded at 10 second intervals. These locations were selected such that they could be at nearly the same distance from the heat source and be in the middle of a printed filament for all patterns. There was some variation due to the differences in available locations between architectures, but they were placed approximately 18 mm apart, with the first cursor in the middle of the filament in contact with the heat source, and the last cursor on the opposite wall. Distances from the edge of the sample were approximated for the cast beams to be equivalent to the 3D printed beams.

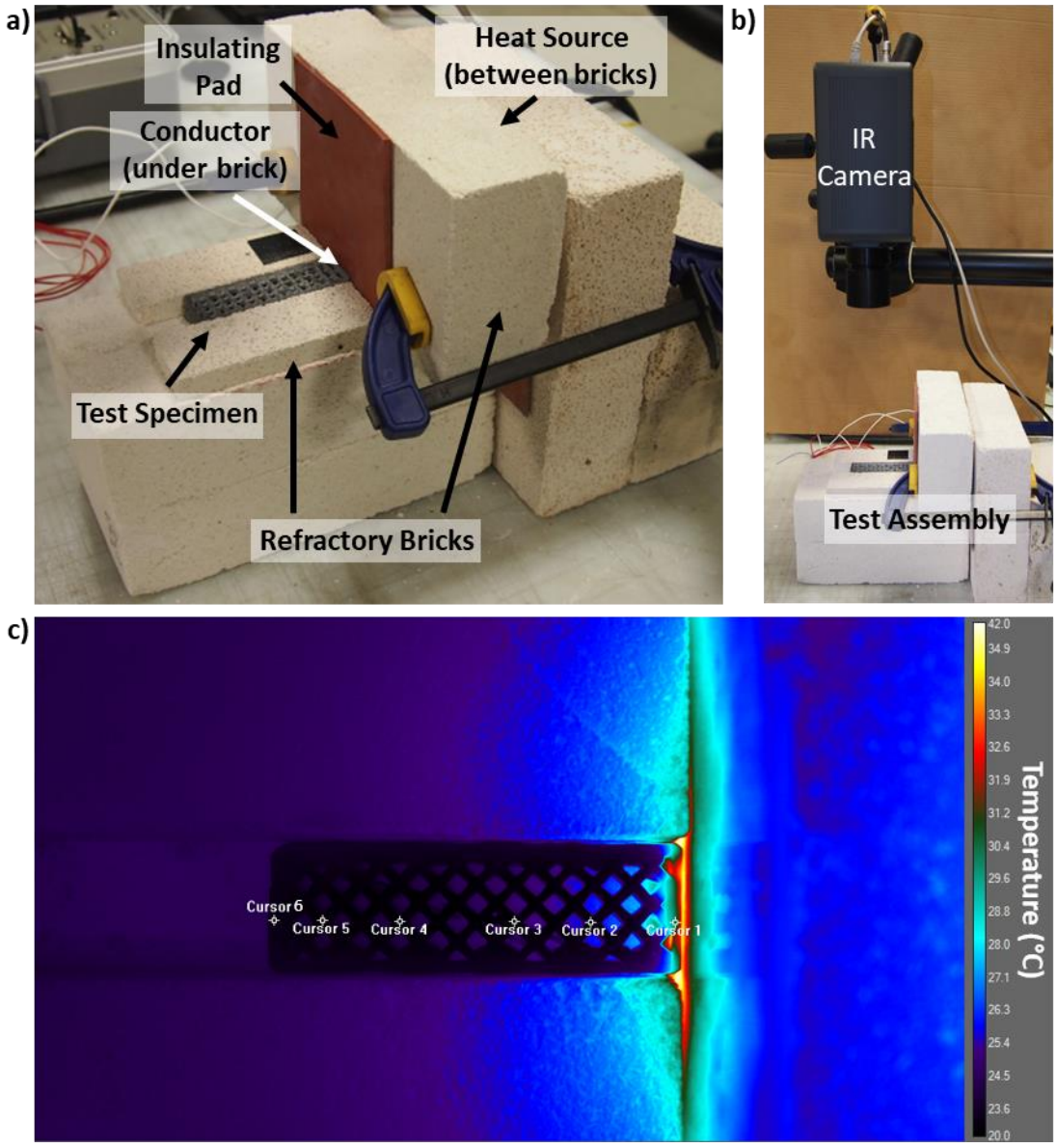

Figure 6-2. (a) Refractory brick sample holder, (b) thermal conduction experiment set-up, and (c) infrared image showing selection of six locations near centerline for temperature monitoring on a 3DHC beam at time $t = 0$.

6.2.4. Analytical model for heat transfer in the 3D printed and cast cement composites

To directly compare the effects of the 3D printed internal architecture and cement ink composition on thermal conductivity, testing beams were modeled as 1-dimensional cooling fins, with one end attached to a heated wall and the rest of the fin exposed to a convective cooling

environment (Figure 6-3). Conceptually, this model is very similar to the experimental setup, with the beam pressed up against the heating source and exposed to the air environment along its top. By modeling the beams – which could be solid or have significant air void patterning – as solid structures, the net effects of internal architecture and ink composition on heat flow could be measured without having to directly model air voids or filament shape. First, temperature evolutions for cursor locations along the beams were modeled in the unsteady-state to estimate the steady-state temperature at each location. Then, the estimated steady-state temperatures were used to model the steady-state temperature profile of the beams as a function of distance from the heat source. From this model, comparative values for the thermal conductivity could be determined. In this way, 'effective' heat transfer characteristics of the whole beam were determined as a single parameter, which accounted for the net role of thermal anisotropy and air voids. Similar approaches of determining the effective thermal conductivity of composite materials, wherein heat must pass through multiple phases, are common [246]. Because not all modeling parameters were known, this method only produced a comparative effective thermal conductivity value (k^*_{eff}) that is proportional to the effective thermal conductivity of the beam. However, this simple procedure allows for direct comparison of the relative thermal conductivity of multiple beam internal architectures and ink formulations.

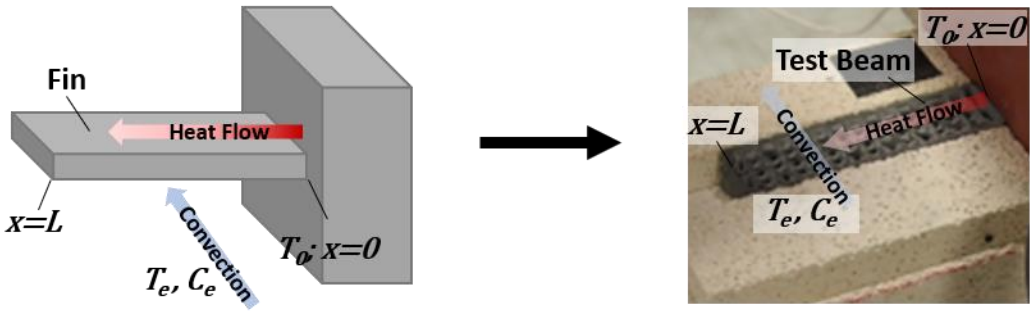

Figure 6-3. Schematic for a cooling fin of length L protruding from a heated wall of temperature T_0 in a convective media of temperature T_e and velocity C_e, where fin temperature is a function of distance from the heat source (x), shown to be conceptually similar to the test beam setup.

For this study, the modeling of the beam heating experimental setup in the unsteady-state is based on a simplified version of the analytical solution for a cooling fin provided by [247]. This

solution, which satisfies Fourier's equation with the initial condition that the fin is in equilibrium with the surrounding temperature, utilizes Green's functions that introduce an infinite summation series. For simplicity, the boundary condition case where the end of the beam is insulated is used. This approximation is appropriate because the temperature change at the end of the beam is small compared to closer to the heat source, indicating most heat is lost through the exposed top surface and little heat is lost through the exposed end. Therefore, the temperature in the beam as a function of distance from the heat source and time can be determined as such:

$$T(x,t) - T_e = \frac{q_0 L}{k}\frac{\left(e^{-m(2L-x)} + e^{-mx}\right)}{mL(1-e^{-2mL})} - \frac{q_0 L}{k}\frac{e^{-m^2\alpha t}}{m^2L^2} - 2\frac{q_0 L}{k}\sum_{n=1}^{\infty}\frac{\cos(\beta_n x/L)}{m^2L^2+\beta_n^2}\cdot\left[\exp\left[-\frac{(m^2L^2+\beta_n^2)\alpha t}{L^2}\right]\right] \quad \textit{Eq. 1}$$

Where $T(x,t)$ is the fin temperature as a function of distance from the heat source (x) and time (t); T_e is the convective environment temperature; q_0 is the rate of heat flow into the fin; L is the length of the fin; k is the conductive heat transfer coefficient; α is a time constant; m is a dimensionless fin constant where $m \equiv \sqrt{\frac{hA_h}{kV}}$ with h [$MLT^{-3}K^{-1}$] being the convective heat transfer coefficient, A_h [L^2] being the surface area for convection, and V [L^3] being the volume of the fin; and $\beta_n = (n - ½)\pi$.

However, as is discussed in the derivation of this analytical solution, the summation series term decays more quickly than the other terms, such that when the system has transitioned from initial heating to heat propagation, it is appropriate to represent the temperature as such:

$$T(x,t) - T_e = \frac{q_0 L}{k}\frac{\left(e^{-m(2L-x)} + e^{-mx}\right)}{mL(1-e^{-2mL})} - \frac{q_0 L}{k}\frac{e^{-m^2\alpha t}}{m^2L^2} \quad \textit{Eq. 2}$$

This expression can then be further simplified by making the following identities:

$$T_{S.S.}(x) \equiv \frac{q_0 L}{k}\frac{\left(e^{-m(2L-x)} + e^{-mx}\right)}{mL(1-e^{-2mL})} \quad \textit{Eq. 3}$$

Where $T_{S.S.}(x)$ is the steady-state temperature in the fin as a function of x,

$$\Delta T^*(x) \equiv \frac{q_0 L}{km^2 L^2} \qquad \textit{Eq. 4}$$

Where $\Delta T^*(x)$ is the increase in temperature between initial conditions and steady-state accounted for by the second term in *Eq. 1*, and

$$\Omega \equiv m^2 \alpha \qquad \textit{Eq. 5}$$

Where Ω [T^{-1}] represents a time constant. While the term $\Delta T^*(x)$ is independent of x as derived from *Eq. 2*, allowing it to fit separately at different values of x for the model reduced sensitivity to the summation term having not entirely decayed. Since the ultimate goal of this fitting is the determination of $T_{S.S.}(x)$ for steady-state modeling, this allowance was found to give more accurate results. Such an allowance was not found to be necessary for Ω.

Based on these simplifications, after a sufficient period of time to allow for the decay of the summation series term, it is appropriate to represent the temperature at each cursor point in a simple exponential form as a modified version of Newton's Law of Cooling, such that:

$$T(x,t) = T_{S.S.}(x) - \Delta T^*(x) e^{-\Omega t} \qquad \textit{Eq. 6}$$

Then, a least-square regression can easily be fitted to the temperature data to determine $T_{S.S.}(x)$, $\Delta T^*(x)$ for each cursor location, and Ω for each beam.

For this study, the first 1000 seconds of each experimental trial was removed from consideration to allow for the decay of the summation series term in *Eq. 1*. This time was found to be appropriate for all temperature profiles, and $T_{S.S.}(x)$ is generally insensitive to further increases in the time selected. Initial estimates for $T_{S.S.}(x)$, $\Delta T^*(x)$ for each cursor point, and Ω for each beam were found by plotting the experimental data and roughly estimating regression. Sum of squares regression and sum of squares total for each time point was subsequently calculated for each cursor. These terms were used to calculate an initial R^2 value for each cursor point. Excel's GRG Non-linear Solver functionality was then used to minimize the sum of ($1-R^2$) values for each cursor by altering $T_{S.S.}(x)$, $\Delta T^*(x)$, and Ω values. Regression equations were checked manually to ensure that the result provided was an appropriate value and not a local minimum for ($1-R^2$). In this way, $T_{S.S.}(x)$ values were determined to be used for steady-state modeling for each beam.

Once values for $T_{S.S.}(x)$ had been established for each cursor location, the steady-state model for the same conceptual setup was used, with the beam being treated as a cooling fin with one side

exposed to a heat source and its surface exposed to a convective cooling environment. This solution is also derived from Fournier's equation and utilizes the same boundary condition of there being no heat transfer from the end of the fin away from the heat source ($x = L$). The other boundary condition is that the temperature of the fin where it is joined to the heat source ($x = 0$) is the same as the heat source. In this situation, the following analytical solution of $T_{S.S.}(x)$ can be used [248]:

$$\frac{T_{S.S.}(x) - T_e}{T_{S.S.}(x = 0) - T_e} = \frac{\cosh\left(\left(1 - \frac{x}{L}\right) mL\right)}{\cosh\left(mL\right)} \qquad \textit{Eq. 7}$$

Where $T_{S.S.}(x=0)$ was approximated by $T_{S.S.}$ for the first cursor position (near the heat source).

$T_{S.S.}(x)$, having been determined from the unsteady-state model, was used for each of the six cursor positions for each beam, $T_{S.S.}(x=0)$ was approximated as the $T_{S.S.}$ value found for the first cursor, and x/L was measured as the distance from the first cursor divided by the distance between the first and last cursor (i.e., $x/L = 0$ near the heat source and 1 near the edge of the beam exposed to the convective environment).

Then, a least-square regression could be taken to model $T_{S.S.}$ at each cursor using *Eq. 7*. Excel's GRG Non-linear Solver functionality was used to minimize (1-R^2) for each beam by altering mL and T_e. The conceptual fin model assumes that the convective media is flowing over a solid beam and T_e is the bulk temperature of the testing room. In this study, largely still air was exposed to complex architecture, allowing for the development of a more complex boundary layer. To account for this, T_e was allowed to be a fitted parameter.

The results were then made to be dimensionless by assigning dimensionless temperature, $\theta \equiv \frac{T_{S.S.}(x) - T_e}{T_{S.S.}(x=0) - T_e}$, and dimensionless length, x/L, yielding the final form:

$$\theta\left(\frac{x}{L}\right) = \frac{\cosh\left(\left(1 - \frac{x}{L}\right) mL\right)}{\cosh\left(mL\right)} \qquad \textit{Eq. 8}$$

This steady-state regression procedure yielded a fitted value for mL for each beam. Taking L as constant, this value is proportional to the effective Biot number for the beam, the ratio of the thermal conductivity coefficient to the convective coefficient. In changing the internal architecture of a 3D printed beam, the pathway for heat conduction is directly altered, changing

the cross-sectional area and tortuosity for heat flow. While this can also be expected to have an effect on the convective properties of the beam, there is less of a relationship between internal architecture and convective surface area. The addition of void structures increased the surface area for convection, but much of that added surface area was away from the top surface of the beam and, therefore, less exposed to the convective media. Likewise, changes in ink composition can be expected to have a greater effect on conductivity (a bulk property) by changing the internal pore structure and hydration products while having comparatively little effect on surface-controlled convective properties.

Therefore, for this study it was assumed that, in changing printing architecture and ink composition, changes in effective Biot number and heat profile were dominated by changes to the conductive behavior rather than the convective behavior. Consequently, with mL being inversely proportional to $(k)^{1/2}$, a dimensionless term for comparative thermal conductivity (k^*_{eff}) can be introduced, which is equal to $1/m^2$ and is proportional to the effective conductive heat transfer coefficient. k^*_{eff} can be directly compared between beams and beam types to determine the comparative effect of architecture and ink design on thermal conductivity.

It should be noted that the Ω value was not used to calculate k^*_{eff} from the unsteady-state model (*Eq. 5*) because there was more variability in Ω based on the initial conditions than for the steady-state model, which is only based on $T_{s.s.}$. Practically, much of this variation can be attributed to small variations in initial conditions for the samples and test setup.

6.3. Results and Discussion

6.3.1. Thermal imaging and temperature profiles

The influence of internal architecture design on thermal properties was overall greater than the influence of HNC incorporation in the cement ink. Among the 3D printed architectures, there was a clear hierarchy of temperature profiles. The AC pattern had the highest degree of heat buildup at Cursor 1 (near the heat source) due to the lack of direct conduction pathway between filaments, with the air void structure crossing the width of the beam. The AC pattern beams also had the most rapid initial rises in temperature at Cursor 1, followed by a rapid settling into a stable temperature profile. The cast beams, conversely, had the lowest degree of heat buildup at

Cursor 1, with a direct path for conduction not interrupted by air voids, and they had a more gradual initial temperature increase, which more gradually transitioned into a stable profile as heat flux was able to continue near the heat source without the higher buildup of driving force required for the less direct flow path of the printed structures. By Cursor 2 – approximately 19 mm from the heat source – and for each subsequent cursor, this dynamic had reversed, with the temperature profiles for the AC beams stabilizing at a lower temperature due to the comparatively low heat flux reaching that point. At all cursors, the temperature profiles for the RL and 3DHC beams were intermediate between that of the AC and cast beams (Figure 6-4). There was, however, not a clear hierarchy between the RL and 3DHC beams based solely on architecture.

The effect of the HNC incorporation was evidenced by the difference in temperature profile behavior when comparing the RL and 3DHC architectures for each ink. For the OPC ink, the temperature profiles were very similar between the two architectures at Cursors 1 and 2 before diverging with the RL beams having higher maximum recorded temperatures at subsequent cursors (Figure 6-5). Conversely, for the HNC ink, the 3DHC beams had more heat buildup more rapidly at Cursor 1, but behaved more similarly to the RL beams at subsequent cursors. This difference can be attributed to the role of thermal anisotropy in directing heat flow within the beams, which appears to have been increased by the incorporation and potential alignment of HNC particles with different thermal behavior from the OPC ink. For the 3DHC architecture, there were layers in which filaments ran predominantly parallel to the direction of heat flow, leading to a buildup of heat in these layers with the heat being relatively trapped by the air void structure. However, it also had layers of filaments which predominantly ran the length of the beam, providing a relatively direct heat conduction pathway in these layers. For the RL beams, conversely, all filaments were at a 45-degree angle relative to the length of the beam. These architecture differences did not significantly impact the temperature profiles for the OPC ink, but when combined with the increased thermal anisotropy imparted by the HNC ink, significant differences in the temperature profiles were observed. For the RL beams printed with the HNC ink there were better conduction pathways away from the heat source, increasing flux and allowing the temperature profile there to settle in a lower temperature range for Cursor 1. However, because this conduction pathway did not lead directly toward the measurement point at subsequent cursors, the heat flux along the beam was reduced. For the 3DHC architecture,

however, the periodic filaments, which were predominantly across the width of the beam served as heat reservoirs (Figure 6-1a), such that it took longer to reach steady state as the cross-filaments warmed, but the warmed cross filaments eventually allowed increased heat flow, allowing similar steady state temperatures as the RL architecture away from the heat source to be reached more gradually. Visualization of heat transfer through each beam type can be seen in Figure 6-6 and Figure 6-7.

These results are in agreement with previous literature, which has shown that infill properties in 3D printed structures can significantly impact thermal properties in thermoplastics 3D printed by fused deposition modeling or in numerical studies on cementitious materials, with filament dimensions, direction, and patterning contributing to thermal anisotropy and reducing thermal transmittance compared to non-printed structures [84, 152, 156, 249-251].

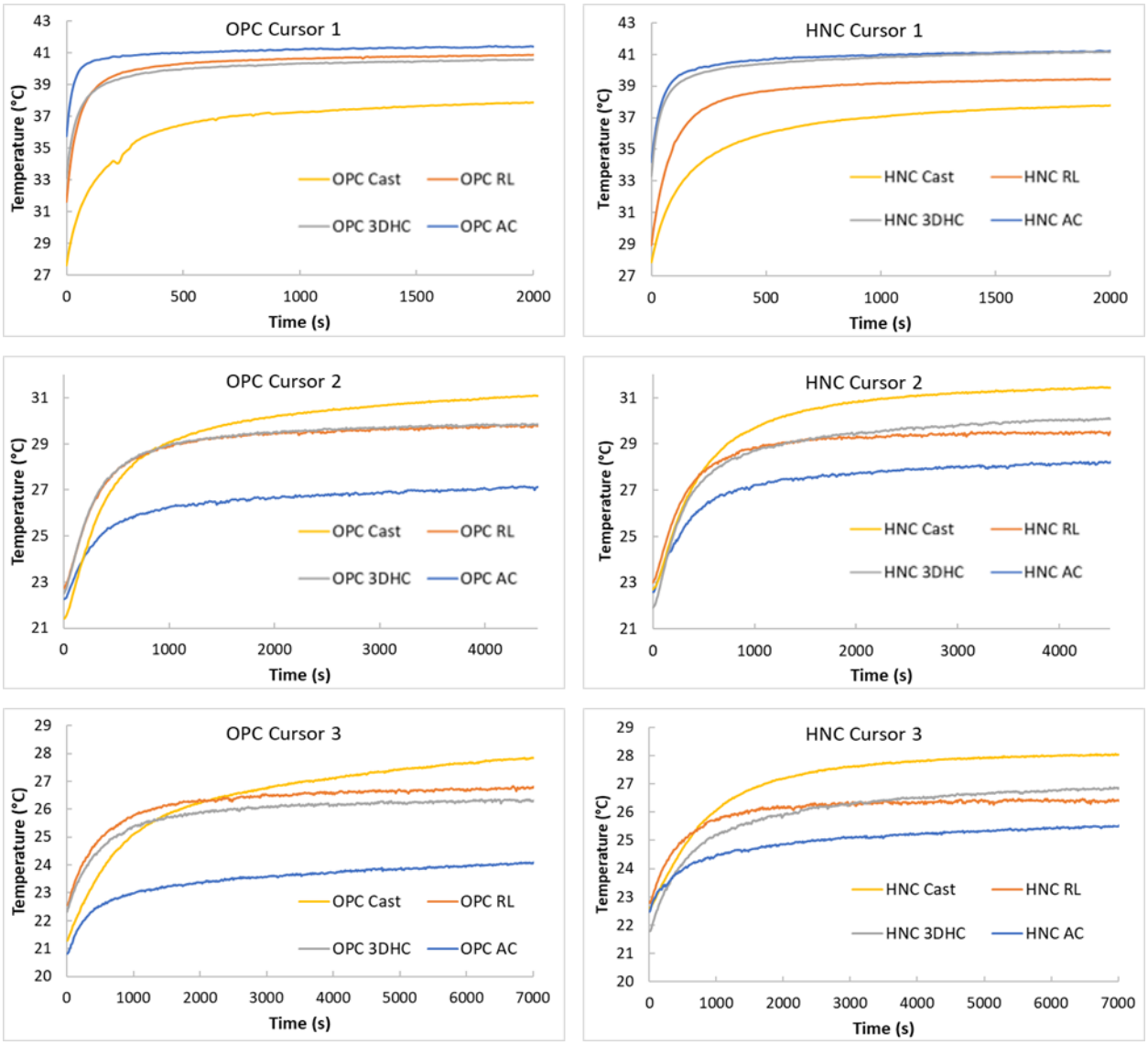

Figure 6-4. Representative temperature vs. time profiles at Cursors 1, 2, and 3 (approximately 1 mm, 19 mm, and 37 mm from the heat source, respectively) for each architecture and ink type. Note that axis scales change by cursor to highlight effects in different temperature ranges and time-scales.

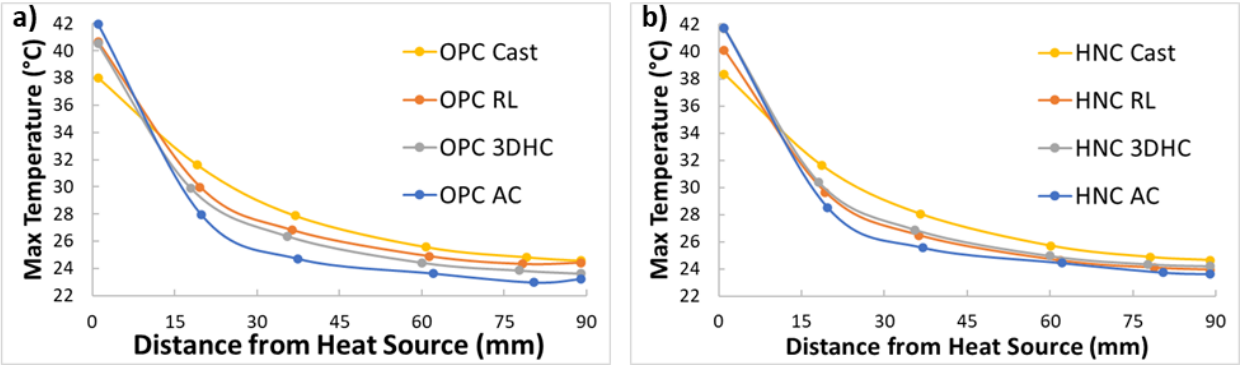

Figure 6-5. Maximum temperature vs. distance from heat source plots of representative beams for each architecture type for (a) the OPC ink and (b) the HNC ink.

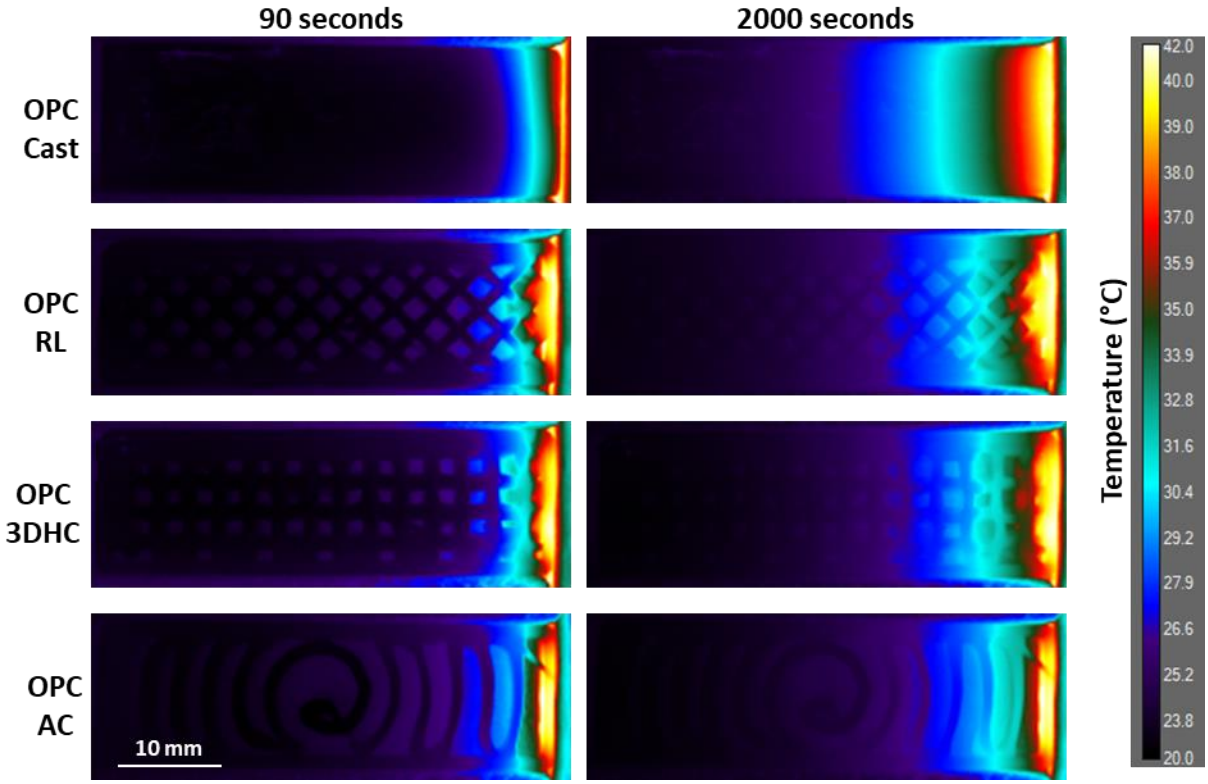

Figure 6-6. Thermal imaging 90 and 2000 seconds after the start of testing for beams 3D printed and cast with the OPC cement ink.

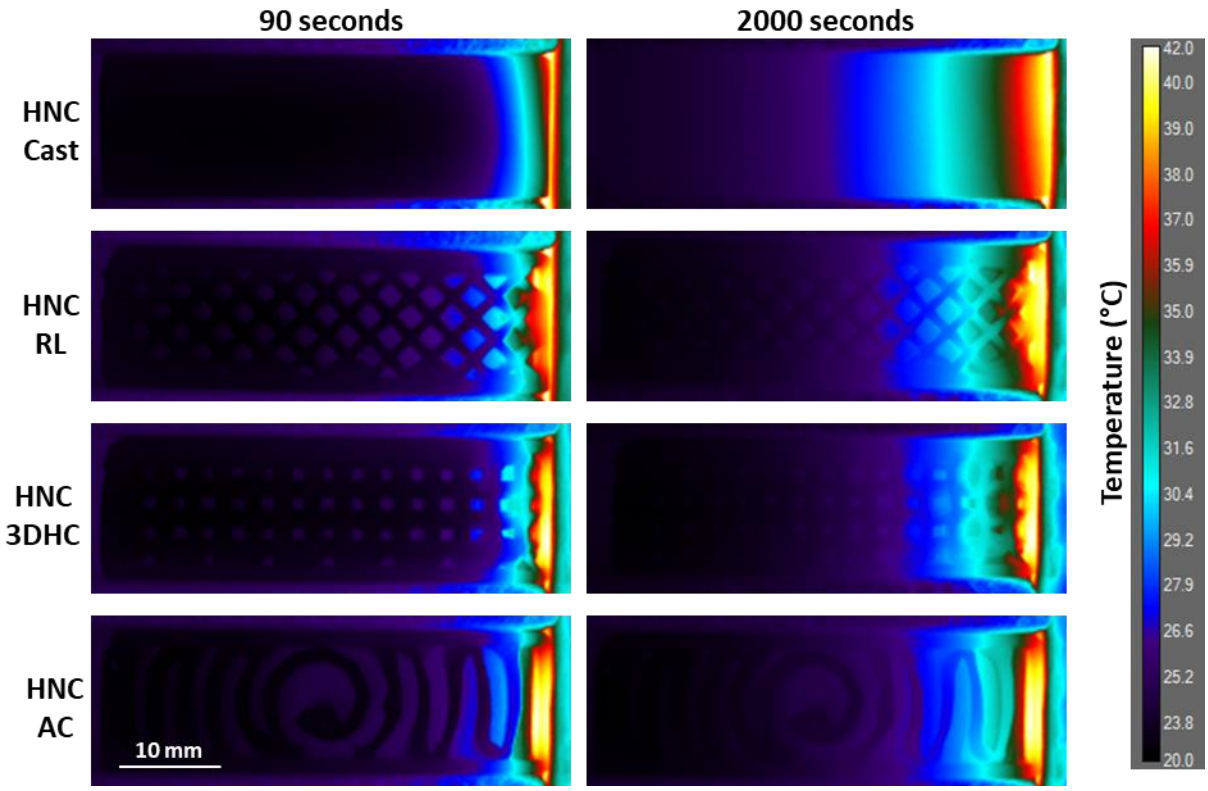

Figure 6-7. Thermal imaging 90 and 2000 seconds after the start of testing for beams 3D printed and cast with the HNC cement ink.

6.3.2. Comparative effective thermal conductivity from analytical model

In agreement with the trends discussed for the maximum temperature vs. cursor profiles (Figure 6-5), there was a clear hierarchy for the effective thermal conductivity based on internal architecture (in order of descending conductivity: cast, RL, 3DHC, and AC, Table 6-1). Statistically significant differences (Welch's T-Test, $\alpha = 0.05$) were observed for each architecture type within each ink type, with the cast beams having the highest effective thermal conductivity, and the AC beams having a 76% and 77% decrease relative to the cast for the OPC and HNC inks, respectively. While differences between the RL and 3DHC could not be clearly differentiated from the experimental measurements, the analytical results revealed that the RL beams had significantly higher effective thermal conductivity than the 3DHC beams (12% and 15% higher for the OPC and HNC inks, respectively). This indicates that the increase in filament

conduction pathways (Figure 6-1a) resulted in increased conductivity, despite those pathways having a less direct path along the beam compared to the more direct but fewer filaments in the 3DHC architecture.

In agreement with the discussion of the temperature profiles, the differences between ink types were smaller than for internal architectures. However, the analytical results revealed that the HNC ink did experience a marginally lower average effective thermal conductivity than the OPC ink for each internal architecture, indicating that HNC incorporation played an insulating role. This difference was only statistically significant at $\alpha = 0.05$ for the AC beams and at $\alpha = 0.1$ for the 3DHC beams. However, the consistent results suggested that the HNC ink reduced the thermal conductivity on average. This result is in agreement with previous literature, which show that incorporating halloysite nanoclay in cementitious materials can result in a reduction in thermal conductivity [167, 168].

Table 6-1. Average k^*_{eff} values (± standard deviation) for each beam type.

	Architecture Type			
Ink Type	Cast	RL	3DHC	AC
OPC	0.1362 ± 0.0081	0.0456 ± 0.0020	0.0408 ± 0.0013	0.0329 ± 0.0013
HNC	0.1251 ± 0.0070	0.0443 ± 0.0018	0.0385 ± 0.0005	0.0282 ± 0.0020

The results for average k^*_{eff} values had standard deviation values that were 7% of the average value or lower for each beam type, indicating a high degree of repeatability based on the three replicates of each of eight sample types. This low degree of variability revealed that the method provided for comparing effective thermal conductivity yielded repeatable results, and, paired with the following more in-depth analysis and model fit quality, suggested that the assumptions made to account for small differences in testing environment were appropriate.

Generally, there was a good agreement between the experimental data collected for temperature evolution at each cursor and the analytical model described in *Eq. 6*. Out of 144 total cursor locations collected on 24 beams, 95 (66%) yielded $R^2 > 0.98$, and 136 (94%) yielded $R^2 > 0.90$.

Only 4 outlier cursors yielded $R^2 < 0.8$. The cast beams generally provided the best curve fits (Figure 6-8a; median $R^2 = 0.99$ for all cast beam cursors, compared to 0.96 for all cursors on 3D printed beams), which is to be expected since they deviated the least from the conceptual model of a solid cooling fin. As predicted by the summation series term presented in *Eq. 1*, the first 1000 s of beam testing generally presented lower temperatures, but starting the curve-fitting at 1000 s provided adequate time for that term to decompose and the exponential form to dominate (Figure 6-8).

In agreement with the assumptions on the boundary conditions, there was a general reduction in fitting quality near the end of the beams away from the heat source. For all samples, Cursors 1-4 had a mean R^2 value of 0.98, while Cursors 5 and 6 had a mean R^2 value of 0.95. Further from the heat source, where less heat was being conducted, small variations in convection had a larger effect on the temperature profile, so the beam was more prone to fluctuations in temperature caused by small changes in room conditions. Additionally, this reduction in R^2 value was primarily driven by the 4 outlier cursor fits having $R^2 < 0.8$ (mean $R^2 = 0.54$). These low-quality fits ($R^2 < 0.8$) generally coincided with slightly reduced fit qualities for cursors closer to the heat source (mean $R^2 = 0.92$ for cursors preceding poor-quality fits). This indicates that non-steady state fit quality was occasionally impacted by small variations in testing conditions, likely with changes in convection conditions greatly affecting cursors far from the heat source while only slightly affecting those closer. The R^2 values for the other 44 Cursors 5 and 6 profiles was on par with that of Cursors 1-4 ($R^2 = 0.98$ for each; Figure 6-8b). Even for the low-R^2 outlier cursors, the fitted value obtained for $T_{s.s.}$ was determined to be appropriate for use in the steady-state model, as it represented a good central estimate for the steady-state temperature, despite the lower signal-to-noise ratio (Figure 6-8c). This result further indicates that the experimental approach was robust despite the potential for small changes in the testing environment.

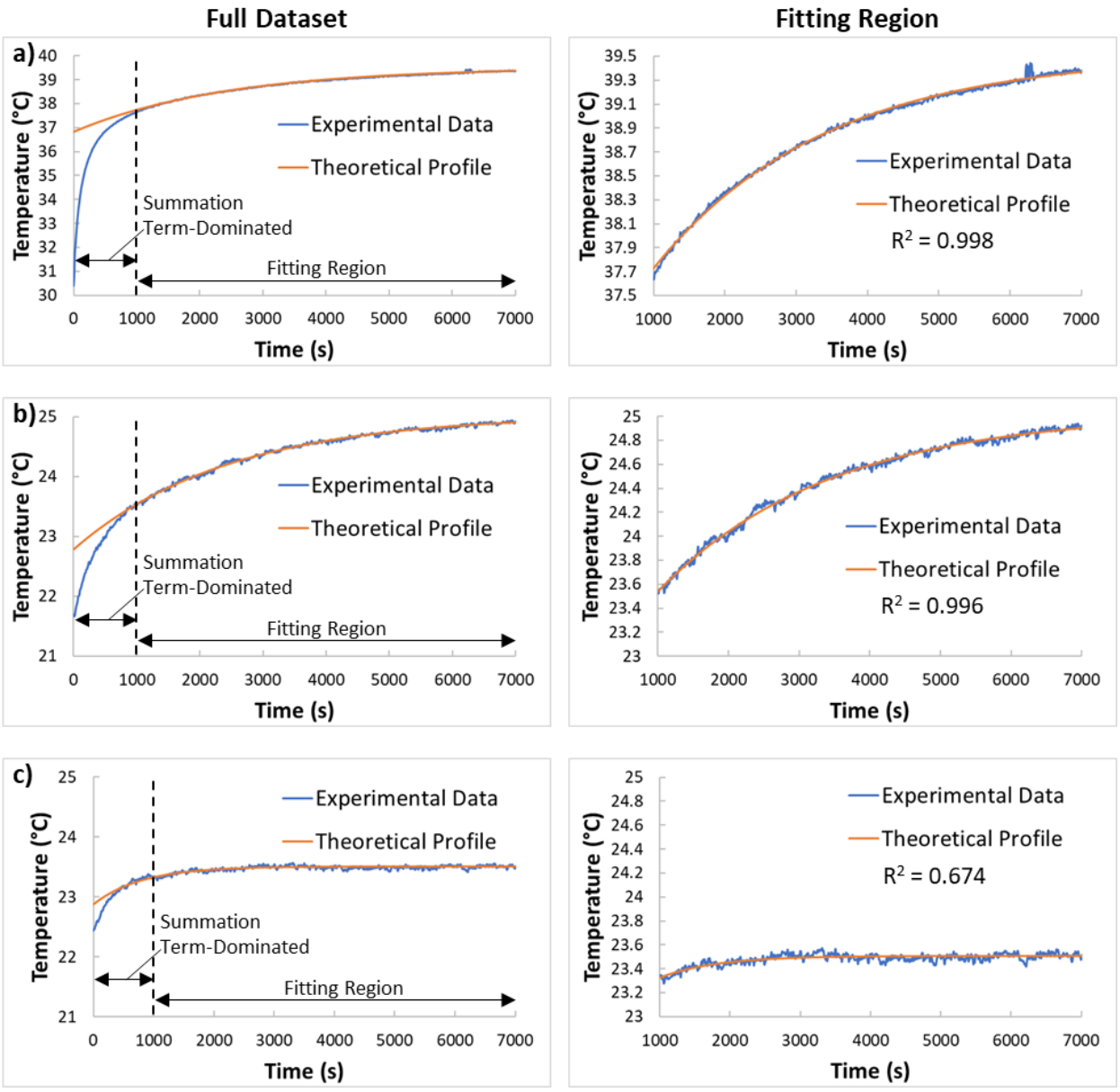

Figure 6-8. Experimental data and theoretical temperature profiles fitted to experimental data starting at 1000 seconds for (a) a high-quality fit near the heat source (Cursor 1 for an HNC cast beam); (b) a high-quality fit further from the heat source (Cursor 4 for an HNC 3DHC beam); and (c) a low-quality fit (Cursor 6 for an HNC RL beam).

Using the $T_{s.s.}$ calculated for each cursor location with the unsteady-state model to fit the steady-state model for each beam presented in *Eq. 8* yielded high-quality fitting ($R^2 > 0.997$ for all

beams tested). Examples of the steady-state temperature profile as a function of distance from the heat source are shown for the OPC ink with each internal architecture in Figure 6-9. The range for the dimensionless temperature θ for each beam was nearly 0 to 1 for all 3D printed samples (Figure 6-9b-d), (and had to be constrained to prevent slightly negative values at for Cursor 6 in some cases). Practically, this range occurred because the convective environmental temperature (T_e) was a fitted parameter, yielding temperatures that were very near or equal to the Cursor 6 steady-state temperature ($T_{S.S.}$). These T_e values were significantly higher than what was measured for the actual air temperature in the testing room (22.1 – 24.5 °C for 3D printed beams, compared to 20.6 °C room temperature) leading to less difference between T_e and $T_{S.S.}$ and θ values near 0. This discrepancy is due to the relatively still air forming a boundary layer around the beam with a higher temperature than the surrounding air. However, this was not the case for the cast beams, as the flat top surface led to less stagnation of the air in the void structure, allowing a greater difference between air and surface temperature (Figure 6-9a).

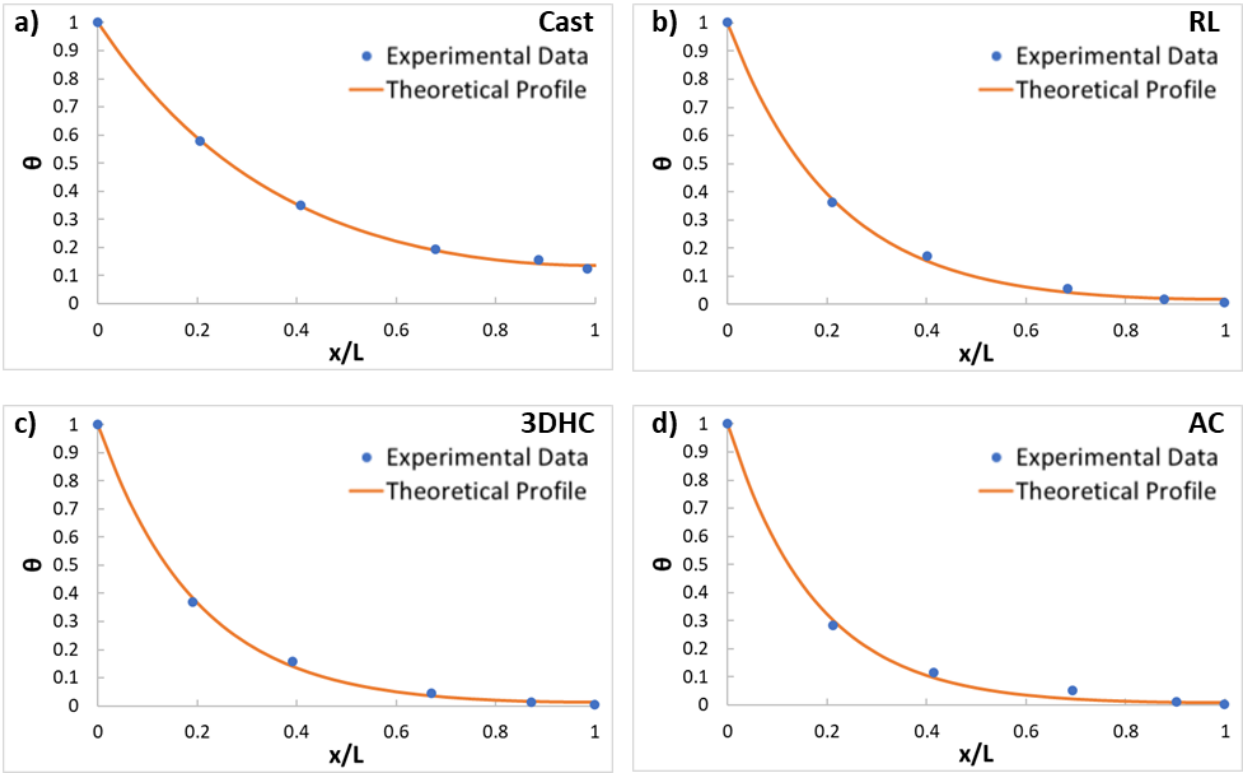

Figure 6-9. Experimental data and theoretical temperature profiles for OPC ink beams (a) cast; and with printed internal architectures: (b) rectilinear (RL), (c) 3-dimensional honeycomb (3DHC), and (d) Archimedean chords (AC).

6.4. Conclusions

The effects of internal architecture and ink formulation on thermal properties for 3D printed cement-composite beams were evaluated by using a novel approach that integrated a thermal conduction experimental setup for real-time infrared thermal imaging and a conceptual 1-dimensional heat transfer fin model for calculating the effective thermal conductivity of 3D printed beam with complex internal architectures. Based on the presented results, the following conclusions could be drawn:

- The difference in effective thermal conductivity between cement inks was smaller than that for internal architectures, though the HNC ink consistently had lower thermal conductivity than the OPC ink for each internal architecture type.
- The following clear progression was observed for internal architectures in order of decreasing effective thermal conductivity, regardless of cement ink used: cast, RL, 3DHC, AC, with air voids and fewer direct conduction pathways resulting in reduced conductivity.
- The experimental setup combined with the conceptual 1-dimensional heat transfer fin model was found to be robust, producing results with a good degree of repeatability.

These findings suggest that internal architecture design and cement ink formulation can be used to tune the thermal properties of 3D printed structures, and that the proposed experimental setup can be used for a wide variety of internal architectures and material compositions for developing construction-scale 3D printing technology to improve the thermal performance of building envelopes.

CHAPTER 7

CONCLUSIONS AND FUTURE WORK

The effects of the 3D printing process and cement ink formulation on the chemo-mechanical and thermal properties of 3D printed cement-based materials were studied. Results showed that the extrusion shear forces required for filament formation and extrusion can result in dynamic changes in the composition of extruded filaments compared to the original cement ink formulation. These changes were shown to impact ink printability and multiscale mechanical performance of printed filaments and structures. Cement inks, which did not adequately prevent segregation from this mechanism were not consistently printable. Even for cement inks with adequate printability, dynamic changes in filament composition and water-to-cement (w/c) ratio resulted in the formation of high mechanical property (HMP) and low mechanical property (LMP) filaments. Cement ink additives were found to impact the ink stability, with carbon nanofibers (CNFs) found to cause underextrusion and generally reduce printability, resulting in reduced macromechanical properties. Carbon microfibers (CFs) were found to preferentially align in the direction of printing and reduce the impact of printing on compressive strength, though CF-induced blockages periodically caused printing discontinuities. Halloysite nanoclay (HNC) incorporation was found to increase filament stability and improve printability. However, HNC incorporation did not prevent the formation of HMP and LMP filaments due to variations in HNC concentration and clustering behavior. 3D printing was found to help break up HNC clusters. HNC was also found to marginally reduce the thermal conductivity of printed structures. A much larger effect on thermal conductivity was found for changes in the internal architecture of printed structures caused by differences in void structures and heat conduction pathways.

A summary of the primary conclusions from each of the main chapters of this dissertation, which provides insight into the relationships between the 3D printing process, cement ink formulation, and multiscale performance, follows:

Chapter 3: The effects of the printing process on the micromechanical properties of printed filaments were examined through the use of statistical grid nanoindentation coupled with environmental scanning electron microscopy and energy-dispersive X-ray spectroscopy

(ESEM/EDS). Dynamic changes in the w/c ratio during the extrusion process combined with stress-induced dissolution of the cement particles led to variation in the median modulus of the printed filaments, with filaments having values greater than 23 GPa or lower than 20 GPa. All extruded filaments and cast specimens (except the specimen cast with a higher w/c ratio) were found to have four distinct micromechanical phases: one associated with the hydrated portions of the microstructure, which accounted for the majority of all indents, one associated with composite phases near the interfaces between hydrates and unhydrated particles, and two associated with unhydrated particles. For the hydrated portion of the microstructure, hardness values experienced significantly less impact than modulus, indicating that changes in phase assemblage primarily impacted resistance to elastic deformation, not plastic deformation. In the unhydrated portion of the microstructure, increased shear stresses associated with higher w/c ratio resulted in partial dissolution of unhydrated cement particles, causing a reduction in modulus and hardness values. The absence of separate peaks for different C-S-H morphologies and a high proportion of mixed hydrate phases were attributed to the effects of the admixtures required for printability on the hydration chemistry, particularly the deposition of CH. The distribution of modulus values was also found to have been affected by extrusion through a small diameter nozzle, which caused the printed filaments to have a more uniform mesoscale packing of C-S-H compared to their traditionally cast counterparts.

Chapter 4: The effect of CNF and CF internal reinforcement on filament formation and microstructure and macroscale mechanical properties was studied. Fiber type was found to have a significant impact on the lubrication layer, with the CNF ink having the largest lubrication layer due to CNF hydrophobicity. This resulted in characteristically underextruded filaments for the CNF ink with a high amount of surface water. Consequently, CNF inclusion was determined to promote segregation and reduce printability. For the CF ink, CFs were found to align in the direction of printing, though occasional failure to properly align led to nozzle blockages and discontinuous extrusion. Partial blockages of the printing nozzle resulted in zones of high- and low-CF density in the microstructure, as fibers occasionally built up at the nozzle and were discharged at once. While 3D printing resulted in lower seven-day compressive strength compared to cast specimens, the addition of CFs within the cement ink reduced the strength difference between the cast and printed cement composites and provided a strain softening in the post peak behavior.

Chapter 5: The effect of HNC on the chemo-mechanical behavior of a cement ink was investigated. HNC incorporation was found to improve the stability of the cement ink, resulting in increased printability with a reduced printing error rate. Visibly less surface water on extruded filaments was also observed, indicating a reduction in ink segregation under extrusion pressure. However, HMP and LMP filaments were still formed for the HNC ink, with the HNC ink having HMP filaments with higher median modulus values (34 GPa) and the LMP filaments having lower median modulus values (13 GPa) than the corresponding OPC ink filaments. The HNC ink cast specimen had similar micromechanical properties as the OPC ink cast specimens. HNC clusters, intermixed with hydration products, were observed in the microstructure. The extruded filaments were found to have smaller clusters than the cast specimen, indicating that the printing process helped to break up clusters. The HMP filament had a lower concentration of clustered HNC than the LMP filament or cast specimen. The effect of HNC dispersed in the microstructure was compared between the filaments and cast specimen through degree of hydration, the concentration of Al rich hydrate phases, and pozzolanic activity. The LMP filament was found to have the most HNC dispersed in the microstructure, followed by the HMP filament, then the cast specimen. Changes in HNC concentration in filaments were attributed to migration during extrusion and partial blockages in the printing nozzle, resulting in regions of high- and low-concentration, similarly to that observed for the CFs. The presence of HNC in the HMP filament, which had evidence of the least clustered and dispersed HNC, improved the density of the microstructure compared to the cast specimen and the OPC ink filaments. In the LMP filament, which had more clustered and dispersed HNC, HNC was thought to interrupt the hydrate phase matrix, resulting in a more loosely-packed microstructure with lower micromechanical properties, analogous to the effect of higher w/c ratio in the OPC ink LMP filaments. For the cast specimen, which had the most HNC in the clustered state, the HNC's effects on the micromechanical properties were marginal. At the macroscale, specimens printed with the HNC ink had similar average compressive and flexural properties as those printed with the OPC ink, though with a significant reduction in variance. This was attributed to the improvement in filament extrusion quality being offset by the behavior of HNC in the microstructure. This is further evidenced by the behavior of the HNC ink cast specimens, which had a significant reduction in strength compared to the OPC ink cast specimens absent the benefit of improved printability or clusters being broken up by the printing process.

Chapter 6: The effects of internal architecture and HNC incorporation on thermal behavior were studied. Comparative effective thermal conductivities were evaluated by analyzing results based on a conceptual model. A printed beam with one end exposed to a heating source was modeled as a cooling fin conducting heat away from a heat source to disperse heat by convection. The unsteady-state temperature profile of each beam was analyzed at several distances from the heat source to estimate the steady-state behavior as a function of distance from the heat source. The estimated steady-state behavior was then used to model the steady-state temperature profile of the whole beam as a function of distance from the heat source. From this, a value which is proportional to the effective thermal conductivity constant of the beam could be calculated. This value allowed effective thermal conductivity to be compared between beams with different internal architectures and ink formulations. Internal architecture was found to have a larger impact on thermal conductivity than HNC incorporation, with differences in void structure and conductivity pathways resulting in a hierarchy of thermal conductivity by internal architecture. The cast specimens were found to have the highest thermal conductivity, as conduction directly along the beam was allowed. Thermal conductivity was lowest for the AC pattern, which did not have connecting filaments throughout the beam, resulting in a greater than 75% reduction in thermal conductivity compared to the cast. The 3DHC pattern had increased thermal conductivity compared to the AC pattern, followed by the RL pattern. The effect of HNC was comparatively small, though it did result thermal conductivity being reduced by 3 – 14%, depending on internal architecture. The analytical model was found to produce results with a high degree of repeatability, with the standard deviation being 7% of the average value or less for comparative effective thermal conductivity for all specimen types.

Future Work: Based on the research presented in this dissertation, addressing the following questions in future work is recommended:

- *Micromechanical anisotropy in printed filaments:* Is there a directionality in micromechanical properties of printed filaments based on orientation caused by the proposed alignment of mesoscale C-S-H during printing?
- *HNC concentration and clustering in cement ink formulations:* Can HNC's dispersion qualities and effect on the microstructure be influenced by changing the concentration of HNC in the cement ink or alternative dispersion methods (e.g., sonication)?

- *Using HNC to improve printability for inks with CNF:* Can the improvement in ink stability from HNC incorporation be used to improve the printability of cement inks with CNFs or help promote CNF dispersion?
- *Influence of fiber reinforcement on thermal performance:* How do different types of short fiber reinforcement impact the thermal behavior of printed structures, and how is thermal anisotropy influenced by fiber alignment in the direction of printing?

REFERENCES

[1] Y.W.D. Tay, B. Panda, S.C. Paul, N.A. Noor Mohamed, M.J. Tan, K.F. Leong, 3D printing trends in building and construction industry: a review, Virtual and Physical Prototyping 12(3) (2017) 261-276.
[2] P. Wu, J. Wang, X. Wang, A critical review of the use of 3-D printing in the construction industry, Automation in Construction 68 (2016) 21-31.
[3] V. Mechtcherine, F.P. Bos, A. Perrot, W.L. da Silva, V. Nerella, S. Fataei, R.J. Wolfs, M. Sonebi, N. Roussel, Extrusion-based additive manufacturing with cement-based materials–production steps, processes, and their underlying physics: a review, Cement and Concrete Research 132 (2020) 106037.
[4] S. Hou, Z. Duan, J. Xiao, J. Ye, A review of 3D printed concrete: Performance requirements, testing measurements and mix design, Construction and Building Materials (2020) 121745.
[5] K.V. Wong, A. Hernandez, A review of additive manufacturing, ISRN Mechanical Engineering 2012 (2012).
[6] B. Lu, Y. Weng, M. Li, Y. Qian, K.F. Leong, M.J. Tan, S. Qian, A systematical review of 3D printable cementitious materials, Construction and Building Materials 207 (2019) 477-490.
[7] M.S. Khan, F. Sanchez, H. Zhou, 3-D printing of concrete: Beyond horizons, Cement and Concrete Research 133 (2020) 106070.
[8] T. Wangler, N. Roussel, F.P. Bos, T.A. Salet, R.J. Flatt, Digital concrete: a review, Cement and Concrete Research 123 (2019) 105780.
[9] T.S. Rushing, P.B. Stynoski, L.A. Barna, G.K. Al-Chaar, J.F. Burroughs, J.D. Shannon, M.A. Kreiger, M.P. Case, Investigation of concrete mixtures for additive construction, 3D Concrete Printing Technology, Elsevier2019, pp. 137-160.
[10] M. Hambach, D. Volkmer, Properties of 3D-printed fiber-reinforced Portland cement paste, Cement and Concrete Composites 79 (2017) 62-70.
[11] V. Mechtcherine, J. Grafe, V.N. Nerella, E. Spaniol, M. Hertel, U. Füssel, 3D-printed steel reinforcement for digital concrete construction – Manufacture, mechanical properties and bond behaviour, Construction and Building Materials 179 (2018) 125-137.
[12] V.N. Nerella, H. Ogura, V. Mechtcherine, Incorporating reinforcement into digital concrete construction, Proceedings of IASS Annual Symposia, International Association for Shell and Spatial Structures (IASS), 2018, pp. 1-8.
[13] B. Panda, S.C. Paul, M.J. Tan, Anisotropic mechanical performance of 3D printed fiber reinforced sustainable construction material, Materials Letters 209 (2017) 146-149.
[14] B. Nematollahi, P. Vijay, J. Sanjayan, A. Nazari, M. Xia, V. Naidu Nerella, V. Mechtcherine, Effect of polypropylene fibre addition on properties of geopolymers made by 3D printing for digital construction, Materials 11(12) (2018) 2352.
[15] Y. Weng, S. Qian, L. He, M. Li, M.J. Tan, 3D printable high performance fiber reinforced cementitious composites for large-scale printing, (2018).
[16] B. Zareiyan, B. Khoshnevis, Effects of mixture ingredients on interlayer adhesion of concrete in Contour Crafting, Rapid Prototyping Journal 24(3) (2018) 584-592.
[17] F. Bos, E. Bosco, T. Salet, Ductility of 3D printed concrete reinforced with short straight steel fibers, Virtual and Physical Prototyping 14(2) (2019) 160-174.
[18] D.G. Soltan, V.C. Li, A self-reinforced cementitious composite for building-scale 3D printing, Cement and Concrete Composites 90 (2018) 1-13.

[19] Y. Bao, M. Xu, D. Soltan, T. Xia, A. Shih, H.L. Clack, V.C. Li, Three-Dimensional Printing Multifunctional Engineered Cementitious Composites (ECC) for Structural Elements, RILEM International Conference on Concrete and Digital Fabrication, Springer, 2018, pp. 115-128.
[20] J. Yu, C.K. Leung, Impact of 3D Printing Direction on Mechanical Performance of Strain-Hardening Cementitious Composite (SHCC), RILEM International Conference on Concrete and Digital Fabrication, Springer, 2018, pp. 255-265.
[21] H. Ogura, V. Nerella, V. Mechtcherine, Developing and testing of strain-hardening cement-based composites (SHCC) in the context of 3D-printing, Materials 11(8) (2018) 1375.
[22] A. Kazemian, X. Yuan, E. Cochran, B. Khoshnevis, Cementitious materials for construction-scale 3D printing: Laboratory testing of fresh printing mixture, Construction and Building Materials 145 (2017) 639-647.
[23] S.C. Figueiredo, C.R. Rodríguez, Z.Y. Ahmed, D. Bos, Y. Xu, T.M. Salet, O. Çopuroğlu, E. Schlangen, F.P. Bos, An approach to develop printable strain hardening cementitious composites, Materials & Design 169 (2019) 107651.
[24] M. Hambach, M. Rutzen, D. Volkmer, Properties of 3D-printed fiber-reinforced Portland cement paste, 3D Concrete Printing Technology, Elsevier2019, pp. 73-113.
[25] S. Ramakrishnan, S. Muthukrishnan, J. Sanjayan, K. Pasupathy, Concrete 3D printing of lightweight elements using hollow-core extrusion of filaments, Cement and Concrete Composites 123 (2021) 104220.
[26] B. Panda, S. Ruan, C. Unluer, M.J. Tan, Investigation of the properties of alkali-activated slag mixes involving the use of nanoclay and nucleation seeds for 3D printing, Composites Part B: Engineering 186 (2020) 107826.
[27] Y. Qian, S. Ma, S. Kawashima, G. De Schutter, Rheological characterization of the viscoelastic solid-like properties of fresh cement pastes with nanoclay addition, Theoretical and Applied Fracture Mechanics 103 (2019) 102262.
[28] S. Kaushik, M. Sonebi, G. Amato, A. Perrot, U.K. Das, Influence of nanoclay on the fresh and rheological behaviour of 3D printing mortar, Materials Today: Proceedings (2022).
[29] A.S. Natanzi, C. McNally, Characterising Concrete Mixes for 3D Printing, RILEM International Conference on Concrete and Digital Fabrication, Springer, 2020, pp. 83-92.
[30] M. Sonebi, M. Dedenis, S. Amziane, A. Abdalqader, A. Perrot, Effect of Red Mud, Nanoclay, and Natural Fiber on Fresh and Rheological Properties of Three-Dimensional Concrete Printing, ACI Materials Journal 118(6) (2021).
[31] M.A. Moeini, M. Hosseinpoor, A. Yahia, 3D printing of cement-based materials with adapted buildability, Construction and Building Materials 337 (2022) 127614.
[32] S. Kawashima, K. Wang, R.D. Ferron, J.H. Kim, N. Tregger, S. Shah, A review of the effect of nanoclays on the fresh and hardened properties of cement-based materials, Cement and Concrete Research 147 (2021) 106502.
[33] T. Pan, Y. Jiang, H. He, Y. Wang, K. Yin, Effect of Structural Build-Up on Interlayer Bond Strength of 3D Printed Cement Mortars, Materials 14(2) (2021) 236.
[34] Y. Zhang, Y. Zhang, G. Liu, Y. Yang, M. Wu, B. Pang, Fresh properties of a novel 3D printing concrete ink, Construction and building materials 174 (2018) 263-271.
[35] D. Chung, Cement reinforced with short carbon fibers: a multifunctional material, Composites Part B: Engineering 31(6-7) (2000) 511-526.
[36] F. Sanchez, L. Zhang, C. Ince, Multi-scale performance and durability of carbon nanofiber/cement composites, Nanotechnology in Construction 3, Springer2009, pp. 345-350.

[37] L. Gao, T.-W. Chou, E.T. Thostenson, Z. Zhang, A comparative study of damage sensing in fiber composites using uniformly and non-uniformly dispersed carbon nanotubes, Carbon 48(13) (2010) 3788-3794.
[38] D. Gao, M. Sturm, Y.L. Mo, Electrical resistance of carbon-nanofiber concrete, Smart Materials and Structures 18(9) (2009) 095039.
[39] L. Gao, T.-W. Chou, E.T. Thostenson, Z. Zhang, M. Coulaud, In situ sensing of impact damage in epoxy/glass fiber composites using percolating carbon nanotube networks, Carbon 49(10) (2011) 3382-3385.
[40] M.S. Konsta-Gdoutos, Z.S. Metaxa, S.P. Shah, Highly dispersed carbon nanotube reinforced cement based materials, Cement and Concrete Research 40(7) (2010) 1052-1059.
[41] J. Hogancamp, Z. Grasley, Dispersion of High Concentrations of Carbon Nanofibers in Portland Cement Mortars, Journal of Nanomaterials 2017 (2017) 11.
[42] T.T. Haw, F. Hart, A. Rashidi, P. Pasbakhsh, Sustainable cementitious composites reinforced with metakaolin and halloysite nanotubes for construction and building applications, Applied Clay Science 188 (2020) 105533.
[43] H. Liu, J. Jin, Y. Yu, H. Liu, S. Liu, J. Shen, X. Xia, H. Ji, Influence of halloysite nanotube on hydration products and mechanical properties of oil well cement slurries with nano-silica, Construction and Building Materials 247 (2020) 118545.
[44] N. Farzadnia, A.A.A. Ali, R. Demirboga, M.P. Anwar, Effect of halloysite nanoclay on mechanical properties, thermal behavior and microstructure of cement mortars, Cement and concrete research 48 (2013) 97-104.
[45] M.A. Moeini, M. Hosseinpoor, A. Yahia, Effectiveness of the rheometric methods to evaluate the build-up of cementitious mortars used for 3D printing, Construction and Building Materials 257 (2020) 119551.
[46] B. Panda, M.J. Tan, Experimental study on mix proportion and fresh properties of fly ash based geopolymer for 3D concrete printing, Ceramics International 44(9) (2018) 10258-10265.
[47] A. Perrot, D. Rangeard, A. Pierre, Structural built-up of cement-based materials used for 3D-printing extrusion techniques, Materials and Structures 49(4) (2016) 1213-1220.
[48] M. Khan, Mix suitable for concrete 3D printing: A review, Materials Today: Proceedings 32 (2020) 831-837.
[49] M. Chen, B. Liu, L. Li, L. Cao, Y. Huang, S. Wang, P. Zhao, L. Lu, X. Cheng, Rheological parameters, thixotropy and creep of 3D-printed calcium sulfoaluminate cement composites modified by bentonite, Composites Part B: Engineering 186 (2020) 107821.
[50] Q. Yuan, Z. Li, D. Zhou, T. Huang, H. Huang, D. Jiao, C. Shi, A feasible method for measuring the buildability of fresh 3D printing mortar, Construction and Building Materials 227 (2019) 116600.
[51] Z. Malaeb, H. Hachem, A. Tourbah, T. Maalouf, N. El Zarwi, F. Hamzeh, 3D concrete printing: machine and mix design, International Journal of Civil Engineering 6(6) (2015) 14-22.
[52] V.N. Nerella, V. Mechtcherine, Studying the Printability of Fresh Concrete for Formwork-Free Concrete Onsite 3D Printing Technology (CONPrint3D), 3D Concrete Printing Technology, Elsevier2019, pp. 333-347.
[53] G. Ma, Z. Li, L. Wang, Printable properties of cementitious material containing copper tailings for extrusion based 3D printing, Construction and building materials 162 (2018) 613-627.

[54] T.T. Le, S.A. Austin, S. Lim, R.A. Buswell, A.G. Gibb, T. Thorpe, Mix design and fresh properties for high-performance printing concrete, Materials and structures 45(8) (2012) 1221-1232.
[55] S. Lim, R.A. Buswell, T.T. Le, S.A. Austin, A.G. Gibb, T. Thorpe, Developments in construction-scale additive manufacturing processes, Automation in construction 21 (2012) 262-268.
[56] H.T. Afarani, N.H. Moser, E.J. Garboczi, E.N. Esfahani, J.J. Biernacki, Print fidelity metrics for additive manufacturing of cement-based materials, Additive Manufacturing 55 (2022) 102784.
[57] A.M. Neville, Properties of concrete, Longman London1995.
[58] C. Özel, K.T. Yücel, Effect of cement content, fibers, chemical admixtures and aggregate shape on rheological parameters of pumping concrete, Arabian Journal for Science and Engineering 38(5) (2013) 1059-1074.
[59] B. Panda, S.C. Paul, N.A.N. Mohamed, Y.W.D. Tay, M.J. Tan, Measurement of tensile bond strength of 3D printed geopolymer mortar, Measurement 113 (2018) 108-116.
[60] Z.Y. AHMED, F.P. BOS, R. WOLFS, T.A. SALET, Design considerations due to scale effects in 3D concrete printing, PARAMETRICISM VS. MATERIALISM (2016) 115.
[61] R.A. Buswell, W.L. de Silva, S. Jones, J. Dirrenberger, 3D printing using concrete extrusion: A roadmap for research, Cement and Concrete Research (2018).
[62] N. Roussel, Rheological requirements for printable concretes, Cement and Concrete Research 112 (2018) 76-85.
[63] Z. Li, L. Wang, G. Ma, Method for the enhancement of buildability and bending resistance of 3D printable tailing mortar, International Journal of Concrete Structures and Materials 12(1) (2018) 37.
[64] R. Wolfs, F. Bos, T. Salet, Hardened properties of 3D printed concrete: The influence of process parameters on interlayer adhesion, Cement and Concrete Research 119 (2019) 132-140.
[65] B. Zareiyan, B. Khoshnevis, Interlayer adhesion and strength of structures in Contour Crafting-Effects of aggregate size, extrusion rate, and layer thickness, Automation in Construction 81 (2017) 112-121.
[66] B. Zareiyan, B. Khoshnevis, Effects of interlocking on interlayer adhesion and strength of structures in 3D printing of concrete, Automation in Construction 83 (2017) 212-221.
[67] V.N. Nerella, S. Hempel, V. Mechtcherine, Micro-and macroscopic investigations on the interface between layers of 3D-printed cementitious elements, Proceedings of the International Conference on Advances in Construction Materials and Systems, Chennai, India, 2017, p. 8.
[68] N. Roussel, F. Cussigh, Distinct-layer casting of SCC: the mechanical consequences of thixotropy, Cement and Concrete Research 38(5) (2008) 624-632.
[69] E. Keita, H. Bessaies-Bey, W. Zuo, P. Belin, N. Roussel, Weak bond strength between successive layers in extrusion-based additive manufacturing: measurement and physical origin, Cement and Concrete Research 123 (2019) 105787.
[70] B. Panda, N. Mohamed, N. Ahamed, S.C. Paul, G. Bhagath Singh, M.J. Tan, B. Šavija, The effect of material fresh properties and process parameters on buildability and interlayer adhesion of 3D printed concrete, Materials 12(13) (2019) 2149.
[71] T. Marchment, J. Sanjayan, M. Xia, Method of enhancing interlayer bond strength in construction scale 3D printing with mortar by effective bond area amplification, Materials & Design 169 (2019) 107684.

[72] Y.W.D. Tay, G.H.A. Ting, Y. Qian, B. Panda, L. He, M.J. Tan, Time gap effect on bond strength of 3D-printed concrete, Virtual and Physical Prototyping 14(1) (2019) 104-113.
[73] J. Putten, G.D. Schutter, K.V. Tittelboom, The effect of print parameters on the (micro) structure of 3D printed cementitious materials, RILEM International Conference on Concrete and Digital Fabrication, Springer, 2018, pp. 234-244.
[74] Z. Geng, W. She, W. Zuo, K. Lyu, H. Pan, Y. Zhang, C. Miao, Layer-interface properties in 3D printed concrete: Dual hierarchical structure and micromechanical characterization, Cement and Concrete Research 138 (2020) 106220.
[75] J.G. Sanjayan, B. Nematollahi, M. Xia, T. Marchment, Effect of surface moisture on inter-layer strength of 3D printed concrete, Construction and Building Materials 172 (2018) 468-475.
[76] V.N. Nerella, S. Hempel, V. Mechtcherine, Effects of layer-Interface properties on mechanical performance of concrete elements produced by extrusion-based 3D-printing, Construction and Building Materials 205 (2019) 586-601.
[77] E. Hosseini, M. Zakertabrizi, A.H. Korayem, G. Xu, A novel method to enhance the interlayer bonding of 3D printing concrete: An experimental and computational investigation, Cement and Concrete Composites 99 (2019) 112-119.
[78] R. Wolfs, F. Bos, T. Salet, Early age mechanical behaviour of 3D printed concrete: Numerical modelling and experimental testing, Cement and Concrete Research 106 (2018) 103-116.
[79] S.C. Paul, Y.W.D. Tay, B. Panda, M.J. Tan, Fresh and hardened properties of 3D printable cementitious materials for building and construction, Archives of civil and mechanical engineering 18(1) (2018) 311-319.
[80] T.T. Le, S.A. Austin, S. Lim, R.A. Buswell, R. Law, A.G. Gibb, T. Thorpe, Hardened properties of high-performance printing concrete, Cement and Concrete Research 42(3) (2012) 558-566.
[81] Y. Zhang, Y. Zhang, W. She, L. Yang, G. Liu, Y. Yang, Rheological and harden properties of the high-thixotropy 3D printing concrete, Construction and Building Materials 201 (2019) 278-285.
[82] Y. Chen, Y. Zhang, B. Pang, Z. Liu, G. Liu, Extrusion-based 3D printing concrete with coarse aggregate: Printability and direction-dependent mechanical performance, Construction and Building Materials 296 (2021) 123624.
[83] H. Alghamdi, N. Neithalath, Synthesis and characterization of 3D-printable geopolymeric foams for thermally efficient building envelope materials, Cement and Concrete Composites 104 (2019) 103377.
[84] G. Ma, A. Ruhan, P. Xie, Z. Pan, L. Wang, J.C. Hower, 3D-printable aerogel-incorporated concrete: Anisotropy influence on physical, mechanical, and thermal insulation properties, Construction and Building Materials 323 (2022) 126551.
[85] T. de Rubeis, 3D-Printed Blocks: Thermal Performance Analysis and Opportunities for Insulating Materials, Sustainability 14(3) (2022) 1077.
[86] G. De Schutter, D. Feys, Pumping of fresh concrete: insights and challenges, RILEM Technical Letters 1 (2016) 76-80.
[87] D. Feys, G. De Schutter, K.H. Khayat, R. Verhoeven, Changes in rheology of self-consolidating concrete induced by pumping, Materials and Structures 49(11) (2016) 4657-4677.
[88] A. Perrot, D. Rangeard, V.N. Nerella, V. Mechtcherine, Extrusion of cement-based materials-an overview, RILEM Technical Letters 3 (2018) 91-97.

[89] T.D. Ngo, A. Kashani, G. Imbalzano, K.T. Nguyen, D. Hui, Additive manufacturing (3D printing): A review of materials, methods, applications and challenges, Composites Part B: Engineering 143 (2018) 172-196.
[90] I.E. Agency, Technology Roadmap: Low-Carbon Transition in the Cement Industry, International Energy Agency Paris, 2018.
[91] K. Kuzmenko, N. Ducoulombier, A. Feraille, N. Roussel, Environmental impact of extrusion-based additive manufacturing: generic model, power measurements and influence of printing resolution, Cement and Concrete Research 157 (2022) 106807.
[92] J. Liu, C. Lv, Properties of 3D-Printed Polymer Fiber-Reinforced Mortars: A Review, Polymers 14(7) (2022) 1315.
[93] F. Bester, M. van den Heever, J. Kruger, G. van Zijl, Reinforcing digitally fabricated concrete: A systems approach review, Additive Manufacturing (2020) 101737.
[94] S. Pessoa, A.S. Guimarães, S.S. Lucas, N. Simões, 3D printing in the construction industry-A systematic review of the thermal performance in buildings, Renewable and Sustainable Energy Reviews 141 (2021) 110794.
[95] F. De Larrard, C. Ferraris, T. Sedran, Fresh concrete: a Herschel-Bulkley material, Materials and structures 31(7) (1998) 494-498.
[96] A.S. Mohammad, J.J. Biernacki, 2D stationary computational printing of cement-based pastes, Cement and Concrete Research 159 (2022).
[97] C.F. Ferraris, F. DeLarrard, Testing and modeling of fresh concrete rheology, 1998.
[98] P.F.G. Banfill, The rheology of fresh cement and concrete-a review, Proceedings of the 11th international cement chemistry congress, 2003, pp. 50-62.
[99] M. Choi, N. Roussel, Y. Kim, J. Kim, Lubrication layer properties during concrete pumping, Cement and Concrete Research 45 (2013) 69-78.
[100] J.H. Kim, S.H. Kwon, S. Kawashima, H.J. Yim, Rheology of cement paste under high pressure, Cement and Concrete Composites 77 (2017) 60-67.
[101] J. Vosahlik, Pumping of Concrete Mixtures: Rheology, Lubrication Layer Properties and Pumping Pressure Assessment, 2018.
[102] D. Kaplan, F. de Larrard, T. Sedran, Design of concrete pumping circuit, ACI materials journal 102(2) (2005) 110.
[103] J. Spangenberg, N. Roussel, J. Hattel, H. Stang, J. Skocek, M. Geiker, Flow induced particle migration in fresh concrete: theoretical frame, numerical simulations and experimental results on model fluids, Cement and Concrete Research 42(4) (2012) 633-641.
[104] M. Moini, J. Olek, J.P. Youngblood, B. Magee, P.D. Zavattieri, Additive manufacturing and performance of architectured cement-based materials, Advanced Materials 30(43) (2018) 1802123.
[105] Y.-C. Wu, Q. Yang, X. Kong, P. Zhi, J. Xiao, Uncertainty quantification for the representative volume element of geometrically monoclinic 3D printed concrete, International Journal of Solids and Structures 226 (2021) 111102.
[106] D. Asprone, C. Menna, F.P. Bos, T.A. Salet, J. Mata-Falcón, W. Kaufmann, Rethinking reinforcement for digital fabrication with concrete, Cement and Concrete Research 112 (2018) 111-121.
[107] M.T. Souza, I.M. Ferreira, E.G. de Moraes, L. Senff, A.P.N. de Oliveira, 3D printed concrete for large-scale buildings: An overview of rheology, printing parameters, chemical admixtures, reinforcements, and economic and environmental prospects, Journal of Building Engineering 32 (2020) 101833.

[108] B. Khoshnevis, Automated construction by contour crafting—related robotics and information technologies, Automation in construction 13(1) (2004) 5-19.
[109] F.P. Bos, Z.Y. Ahmed, R.J. Wolfs, T.A. Salet, 3D printing concrete with reinforcement, High Tech Concrete: Where Technology and Engineering Meet, Springer2018, pp. 2484-2493.
[110] F.P. Bos, Z.Y. Ahmed, E.R. Jutinov, T.A. Salet, Experimental exploration of metal cable as reinforcement in 3D printed concrete, Materials 10(11) (2017) 1314.
[111] Z. Li, L. Wang, G. Ma, J. Sanjayan, D. Feng, Strength and ductility enhancement of 3D printing structure reinforced by embedding continuous micro-cables, Construction and Building Materials 264 (2020) 120196.
[112] S. Lim, R.A. Buswell, T.T. Le, R. Wackrow, S.A. Austin, A.G. Gibb, T. Thorpe, Development of a viable concrete printing process, (2011).
[113] M. Liu, Q. Zhang, Z. Tan, L. Wang, Z. Li, G. Ma, Investigation of steel wire mesh reinforcement method for 3D concrete printing, Archives of Civil and Mechanical Engineering 21(1) (2021) 1-18.
[114] T. Marchment, J. Sanjayan, Mesh reinforcing method for 3D Concrete Printing, Automation in Construction 109 (2020) 102992.
[115] V. Mechtcherine, J. Grafe, V.N. Nerella, E. Spaniol, M. Hertel, U. Füssel, 3D-printed steel reinforcement for digital concrete construction–Manufacture, mechanical properties and bond behaviour, Construction and Building Materials 179 (2018) 125-137.
[116] V. Mechtcherine, V.N. Nerella, H. Ogura, J. Grafe, E. Spaniol, M. Hertel, U. Füssel, Alternative reinforcements for digital concrete construction, RILEM International Conference on Concrete and Digital Fabrication, Springer, 2018, pp. 167-175.
[117] B. Nematollahi, M. Xia, J. Sanjayan, P. Vijay, Effect of type of fiber on inter-layer bond and flexural strengths of extrusion-based 3D printed geopolymer, Materials Science Forum, Trans Tech Publ, 2018, pp. 155-162.
[118] P. Banfill, G. Starrs, G. Derruau, W. McCarter, T. Chrisp, Rheology of low carbon fibre content reinforced cement mortar, Cement and Concrete Composites 28(9) (2006) 773-780.
[119] L. Martinie, P. Rossi, N. Roussel, Rheology of fiber reinforced cementitious materials: classification and prediction, Cement and concrete research 40(2) (2010) 226-234.
[120] G. Ma, Z. Li, L. Wang, F. Wang, J. Sanjayan, Mechanical anisotropy of aligned fiber reinforced composite for extrusion-based 3D printing, Construction and Building Materials 202 (2019) 770-783.
[121] D. Jiao, R. De Schryver, C. Shi, G. De Schutter, Thixotropic structural build-up of cement-based materials: A state-of-the-art review, Cement and Concrete Composites 122 (2021) 104152.
[122] M. Morsy, S. Alsayed, M. Aqel, Effect of nano-clay on mechanical properties and microstructure of ordinary Portland cement mortar, International Journal of Civil & Environmental Engineering IJCEE-IJENS 10(01) (2010) 23-27.
[123] H. Liu, M. Xu, Z. Zhang, S. Liu, H. Zhang, C. Zhang, J. Fu, M. Cong, Z. Li, The Strength and Microstructure Properties of Oil Well Cement with Halloysite Nanotube, IOP Conference Series: Earth and Environmental Science, IOP Publishing, 2020, p. 012118.
[124] H. Yang, Y. Zhang, J. Ouyang, Physicochemical properties of halloysite, Developments in Clay Science 7 (2016) 67-91.
[125] Global Status Report 2017: Towards a zero-emission, efficient, and resilient buildings and construction sector, International Energy Agency, 2017.
[126] The Future of Cooling: Opportunities for energy-efficient air conditioning, International Engergy Agency, 2018.

[127] 2021 Global Status Report for Buildings and Construction: Towards a Zero-emission, Efficient and Resilient Buildings and Construction Sector, United Nations Environment Programme, 2021.
[128] H. Li, Q. Zeng, S. Xu, Effect of pore shape on the thermal conductivity of partially saturated cement-based porous composites, Cement and Concrete Composites 81 (2017) 87-96.
[129] K.-Q. Li, D.-Q. Li, Y. Liu, Meso-scale investigations on the effective thermal conductivity of multi-phase materials using the finite element method, International Journal of Heat and Mass Transfer 151 (2020) 119383.
[130] G. Chen, F. Li, P. Jing, J. Geng, Z. Si, Effect of Pore Structure on Thermal Conductivity and Mechanical Properties of Autoclaved Aerated Concrete, Materials 14(2) (2021) 339.
[131] P.K. Sarkar, N. Mitra, Thermal conductivity of cement paste: Influence of macro-porosity, Cement and Concrete Research 143 (2021) 106385.
[132] A.d.P. Peruzzi, J.A. Rossignolo, H. Kahn, Air-entrained concrete: relationship between thermal conductivity and pore distribution analyzed by X-ray tomography, Journal of Civil Engineering and Architecture 12(7) (2018).
[133] H.-K. Kim, J. Jeon, H.-K. Lee, Workability, and mechanical, acoustic and thermal properties of lightweight aggregate concrete with a high volume of entrained air, Construction and Building Materials 29 (2012) 193-200.
[134] M.A. Hossain, Mechanical and thermal performance of cement mortar incorporating super absorbent polymer (SAP), Civil Engineering Journal 6(11) (2020).
[135] Y.-W. Jeong, T.-H. Koh, K.-S. Youm, J. Moon, Experimental evaluation of thermal performance and durability of thermally-enhanced concretes, Applied Sciences 7(8) (2017) 811.
[136] G. Samson, A. Phelipot-Mardelé, C. Lanos, A review of thermomechanical properties of lightweight concrete, Magazine of Concrete Research 69(4) (2017) 201-216.
[137] Q. Zeng, R. Fang, H. Li, Y. Peng, J. Wang, Tailoring the thermal and mechanical properties of lightweight cement-based composites by macro and micro fillers, Cement and Concrete Composites 102 (2019) 169-184.
[138] Q. Zeng, T. Mao, H. Li, Y. Peng, Thermally insulating lightweight cement-based composites incorporating glass beads and nano-silica aerogels for sustainably energy-saving buildings, Energy and Buildings 174 (2018) 97-110.
[139] B.R. Thompson, T.S. Horozov, S.D. Stoyanov, V.N. Paunov, Hierarchically porous composites fabricated by hydrogel templating and viscous trapping techniques, Materials & Design 137 (2018) 384-393.
[140] P. Xiao, Z. Yifeng, W. Peng, L. Dan, Estimation of thermal conduction in hollow-glass-beads-filled cement-based composites by variational asymptotic homogenization method, Applied Thermal Engineering 161 (2019) 114191.
[141] J. Lu, J. Jiang, Z. Lu, J. Li, Y. Niu, Y. Yang, Pore structure and hardened properties of aerogel/cement composites based on nanosilica and surface modification, Construction and Building Materials 245 (2020) 118434.
[142] M. Záleská, J. Pokorný, M. Pavlíková, Z. Pavlík, Thermal properties of light-weight concrete with waste polypropylene aggregate, AIP Conference Proceedings, AIP Publishing LLC, 2017, p. 040043.
[143] Y. Xie, J. Li, Z. Lu, J. Jiang, Y. Niu, Effects of bentonite slurry on air-void structure and properties of foamed concrete, Construction and Building Materials 179 (2018) 207-219.

[144] Z. Zhao, X. Qu, F. Li, J. Wei, Effects of steel slag and silica fume additions on compressive strength and thermal properties of lime-fly ash pastes, Construction and Building Materials 183 (2018) 439-450.
[145] K. Ali, M.I. Qureshi, S. Saleem, S.U. Khan, Effect of waste electronic plastic and silica fume on mechanical properties and thermal performance of concrete, Construction and Building Materials 285 (2021) 122952.
[146] D.P. Bentz, M.A. Peltz, A. Duran-Herrera, P. Valdez, C. Juarez, Thermal properties of high-volume fly ash mortars and concretes, Journal of Building Physics 34(3) (2011) 263-275.
[147] D. Vásquez-Molina, J.M. Mejía-Arcila, R.M.-d. Gutiérrez, Mechanical and thermal performance of a geopolymeric and hybrid material based on fly ash, Dyna 83(195) (2016) 216-223.
[148] T.-C. Ling, C.-S. Poon, Use of phase change materials for thermal energy storage in concrete: An overview, Construction and Building Materials 46 (2013) 55-62.
[149] U. Berardi, A.A. Gallardo, Properties of concretes enhanced with phase change materials for building applications, Energy and Buildings 199 (2019) 402-414.
[150] A. Adesina, P. Awoyera, A. Sivakrishna, K.R. Kumar, R. Gobinath, Phase change materials in concrete: An overview of properties, Materials Today: Proceedings 27 (2020) 391-395.
[151] S. Drissi, T.-C. Ling, K.H. Mo, A. Eddhahak, A review of microencapsulated and composite phase change materials: Alteration of strength and thermal properties of cement-based materials, Renewable and Sustainable Energy Reviews 110 (2019) 467-484.
[152] H. Marais, H. Christen, S. Cho, W. De Villiers, G. Van Zijl, Computational assessment of thermal performance of 3D printed concrete wall structures with cavities, Journal of Building Engineering 41 (2021) 102431.
[153] B.O. Ayegba, K.-J.I. Egbe, A. Matin Nazar, M. Huang, M.A. Hariri-Ardebili, Resource Efficiency and Thermal Comfort of 3D Printable Concrete Building Envelopes Optimized by Performance Enhancing Insulation: A Numerical Study, Energies 15(3) (2022) 1069.
[154] T. Suntharalingam, P. Gatheeshgar, I. Upasiri, K. Poologanathan, B. Nagaratnam, H. Rajanayagam, S. Navaratnam, Numerical Study of Fire and Energy Performance of Innovative Light-Weight 3D Printed Concrete Wall Configurations in Modular Building System, Sustainability 13(4) (2021) 2314.
[155] T. Suntharalingam, I. Upasiri, B. Nagaratnam, K. Poologanathan, P. Gatheeshgar, K.D. Tsavdaridis, D. Nuwanthika, Finite Element Modelling to Predict the Fire Performance of Bio-Inspired 3D-Printed Concrete Wall Panels Exposed to Realistic Fire, Buildings 12(2) (2022) 111.
[156] T. Suntharalingam, I. Upasiri, P. Gatheeshgar, K. Poologanathan, B. Nagaratnam, P. Santos, H. Rajanayagam, Energy Performance of 3D-Printed Concrete Walls: A Numerical Study, Buildings 11(10) (2021) 432.
[157] S. Yang, S. Wi, J.H. Park, H.M. Cho, S. Kim, Novel proposal to overcome insulation limitations due to nonlinear structures using 3D printing: Hybrid heat-storage system, Energy and Buildings 197 (2019) 177-187.
[158] C. Gosselin, R. Duballet, P. Roux, N. Gaudillière, J. Dirrenberger, P. Morel, Large-scale 3D printing of ultra-high performance concrete–a new processing route for architects and builders, Materials & Design 100 (2016) 102-109.
[159] J. Sun, J. Xiao, Z. Li, X. Feng, Experimental study on the thermal performance of a 3D printed concrete prototype building, Energy and Buildings 241 (2021) 110965.

[160] B. Furet, P. Poullain, S. Garnier, 3D printing for construction based on a complex wall of polymer-foam and concrete, Additive Manufacturing 28 (2019) 58-64.
[161] D. Falliano, E. Gugliandolo, D. De Domenico, G. Ricciardi, Experimental investigation on the mechanical strength and thermal conductivity of extrudable foamed concrete and preliminary views on its potential application in 3D printed multilayer insulating panels, RILEM International Conference on Concrete and Digital Fabrication, Springer, 2018, pp. 277-286.
[162] M. Gomaa, J. Carfrae, S. Goodhew, W. Jabi, A. Veliz Reyes, Thermal performance exploration of 3D printed cob, Architectural Science Review 62(3) (2019) 230-237.
[163] S. Volpe, V. Sangiorgio, A. Petrella, A. Coppola, M. Notarnicola, F. Fiorito, Building Envelope Prefabricated with 3D Printing Technology, Sustainability 13(16) (2021) 8923.
[164] H. Cui, S. Yu, X. Cao, H. Yang, Evaluation of Printability and Thermal Properties of 3D Printed Concrete Mixed with Phase Change Materials, Energies 15(6) (2022) 1978.
[165] Y. He, Y. Zhang, C. Zhang, H. Zhou, Energy-saving potential of 3D printed concrete building with integrated living wall, Energy and Buildings 222 (2020) 110110.
[166] W.-C. Wang, Compressive strength and thermal conductivity of concrete with nanoclay under Various High-Temperatures, Construction and Building Materials 147 (2017) 305-311.
[167] J. Cho, G.R. Waetzig, M. Udayakantha, C.Y. Hong, S. Banerjee, Incorporation of hydroxyethylcellulose-functionalized halloysite as a means of decreasing the thermal conductivity of oilwell cement, Scientific reports 8(1) (2018) 1-13.
[168] M. Udayakantha, J. Cho, K.-W. Liu, A. Mukhopadhyay, S. Gupta, C.Y. Hong, S. Banerjee, An evaluation of the reduction of heat loss enabled by halloysite modification of oilwell cement, Engineering Research Express 1(2) (2019) 025028.
[169] BASF, MasterGlenium 7700, Data Sheet, 2018.
[170] BASF, MasterMatrix UW 450, Data Sheet, 2018.
[171] BASF, MasterMatrix VMA 362, Data Sheet, 2019.
[172] M. Miller, C. Bobko, M. Vandamme, F.-J. Ulm, Surface roughness criteria for cement paste nanoindentation, Cement and Concrete Research 38(4) (2008) 467-476.
[173] W.C. Oliver, G.M. Pharr, Measurement of hardness and elastic modulus by instrumented indentation: Advances in understanding and refinements to methodology, Journal of materials research 19(1) (2004) 3-20.
[174] W.C. Oliver, G.M. Pharr, An improved technique for determining hardness and elastic modulus using load and displacement sensing indentation experiments, Journal of materials research 7(6) (1992) 1564-1583.
[175] D.J. Shuman, A.L. Costa, M.S. Andrade, Calculating the elastic modulus from nanoindentation and microindentation reload curves, Materials characterization 58(4) (2007) 380-389.
[176] L. Brown, P.G. Allison, F. Sanchez, Use of nanoindentation phase characterization and homogenization to estimate the elastic modulus of heterogeneously decalcified cement pastes, Materials & Design 142 (2018) 308-318.
[177] G. Constantinides, K.R. Chandran, F.-J. Ulm, K. Van Vliet, Grid indentation analysis of composite microstructure and mechanics: Principles and validation, Materials Science and Engineering: A 430(1-2) (2006) 189-202.
[178] A. Clausner, F. Richter, Determination of yield stress from nano-indentation experiments, European Journal of Mechanics-A/Solids 51 (2015) 11-20.

[179] W. Da Silva, J. Němeček, P. Štemberk, Methodology for nanoindentation-assisted prediction of macroscale elastic properties of high performance cementitious composites, Cement and Concrete Composites 45 (2014) 57-68.
[180] J. Němeček, V. Králík, V. Šmilauer, L. Polívka, A. Jäger, Tensile strength of hydrated cement paste phases assessed by micro-bending tests and nanoindentation, Cement and Concrete Composites 73 (2016) 164-173.
[181] C. Hu, Y. Gao, Y. Zhang, Z. Li, Statistical nanoindentation technique in application to hardened cement pastes: influences of material microstructure and analysis method, Construction and Building Materials 113 (2016) 306-316.
[182] C. Stephens, Multiscale performance of cement-based composites with carbon nanofibers, Vanderbilt University2013.
[183] M. Kosson, L. Brown, F. Sanchez, Early-Age Performance of 3D Printed Carbon Nanofiber and Carbon Microfiber Cement Composites, Transportation Research Record: Journal of the Transportation Research Board 2674(2) (2020) 10-20.
[184] F.Š. TOMÁŠ SLAMEČKA, The effect of water ratio on microstructre and composition of the hydration products of Portland cement pastes, Ceramics− Silikáty 46(4) (2002) 152-158.
[185] S. Singh, P. Munjal, N. Thammishetti, Role of water/cement ratio on strength development of cement mortar, Journal of Building Engineering 4 (2015) 94-100.
[186] Y.-Y. Kim, K.-M. Lee, J.-W. Bang, S.-J. Kwon, Effect of W/C ratio on durability and porosity in cement mortar with constant cement amount, Advances in Materials Science and Engineering 2014 (2014).
[187] W. Ashraf, J. Olek, J. Jain, Microscopic features of non-hydraulic calcium silicate cement paste and mortar, Cement and Concrete Research 100 (2017) 361-372.
[188] K. Vallurupalli, W. Meng, J. Liu, K.H. Khayat, Effect of graphene oxide on rheology, hydration and strength development of cement paste, Construction and Building Materials 265 (2020) 120311.
[189] Y. Gao, C. Hu, Y. Zhang, Z. Li, J. Pan, Investigation on microstructure and microstructural elastic properties of mortar incorporating fly ash, Cement and Concrete Composites 86 (2018) 315-321.
[190] G. Constantinides, F.-J. Ulm, The nanogranular nature of C–S–H, Journal of the Mechanics and Physics of Solids 55(1) (2007) 64-90.
[191] P. Mondal, S.P. Shah, L.D. Marks, J.J. Gaitero, Comparative study of the effects of microsilica and nanosilica in concrete, Transportation Research Record 2141(1) (2010) 6-9.
[192] C. Hu, Y. Han, Y. Gao, Y. Zhang, Z. Li, Property investigation of calcium–silicate–hydrate (C–S–H) gel in cementitious composites, Materials Characterization 95 (2014) 129-139.
[193] S.C. Figueiredo, O. Çopuroğlu, E. Schlangen, Effect of viscosity modifier admixture on Portland cement paste hydration and microstructure, Construction and Building Materials 212 (2019) 818-840.
[194] P. Mondal, S.P. Shah, L.D. Marks, Nanoscale characterization of cementitious materials, ACI Materials Journal 105(2) (2008) 174.
[195] J.J. Chen, L. Sorelli, M. Vandamme, F.J. Ulm, G. Chanvillard, A Coupled nanoindentation/SEM-EDS study on low water/cement ratio Portland cement paste: evidence for C–S–H/Ca (OH) 2 nanocomposites, Journal of the American Ceramic Society 93(5) (2010) 1484-1493.

[196] L. Sorelli, G. Constantinides, F.-J. Ulm, F. Toutlemonde, The nano-mechanical signature of ultra high performance concrete by statistical nanoindentation techniques, Cement and Concrete Research 38(12) (2008) 1447-1456.
[197] W. Wilson, J. Rivera-Torres, L. Sorelli, A. Durán-Herrera, A. Tagnit-Hamou, The micromechanical signature of high-volume natural pozzolan concrete by combined statistical nanoindentation and SEM-EDS analyses, Cement and Concrete Research 91 (2017) 1-12.
[198] W. Wilson, L. Sorelli, A. Tagnit-Hamou, Automated coupling of NanoIndentation and Quantitative Energy-Dispersive Spectroscopy (NI-QEDS): A comprehensive method to disclose the micro-chemo-mechanical properties of cement pastes, Cement and Concrete Research 103 (2018) 49-65.
[199] L. Xu, F. Deng, Y. Chi, Nano-mechanical behavior of the interfacial transition zone between steel-polypropylene fiber and cement paste, Construction and Building Materials 145 (2017) 619-638.
[200] C. Hu, D. Hou, Z. Li, Micro-mechanical properties of calcium sulfoaluminate cement and the correlation with microstructures, Cement and Concrete Composites 80 (2017) 10-16.
[201] C. Hu, B. Xu, H. Ma, B. Chen, Z. Li, Micromechanical investigation of magnesium oxychloride cement paste, Construction and Building Materials 105 (2016) 496-502.
[202] Z. He, C. Qian, Y. Zhang, F. Zhao, Y. Hu, Nanoindentation characteristics of cement with different mineral admixtures, Science China Technological Sciences 56(5) (2013) 1119-1123.
[203] C. Hu, Z. Li, Y. Gao, Y. Han, Y. Zhang, Investigation on microstructures of cementitious composites incorporating slag, Advances in cement research 26(4) (2014) 222-232.
[204] R. Liu, F. Han, P. Yan, Characteristics of two types of CSH gel in hardened complex binder pastes blended with slag, Science China Technological Sciences 56(6) (2013) 1395-1402.
[205] C. Hu, Nanoindentation as a tool to measure and map mechanical properties of hardened cement pastes, MRS Communications 5(1) (2015) 83-87.
[206] O.A. Hisseine, W. Wilson, L. Sorelli, B. Tolnai, A. Tagnit-Hamou, Nanocellulose for improved concrete performance: A macro-to-micro investigation for disclosing the effects of cellulose filaments on strength of cement systems, Construction and Building Materials 206 (2019) 84-96.
[207] W. Wilson, L. Sorelli, A. Tagnit-Hamou, Unveiling micro-chemo-mechanical properties of C–(A)–S–H and other phases in blended-cement pastes, Cement and Concrete Research 107 (2018) 317-336.
[208] L. Brown, C.S. Stephens, P.G. Allison, F. Sanchez, Effect of Carbon Nanofiber Clustering on the Micromechanical Properties of a Cement Paste, Nanomaterials 12(2) (2022) 223.
[209] T. Howind, J. Hughes, W. Zhu, F. Puertas, S. Goñi Elizalde, M.S. Hernandez, A. Guerrero Bustos, M. Palacios, J.S. Dolado, Mapping of mechanical properties of cement paste microstructures, (2011).
[210] P. Acker, Micromechanical analysis of creep and shrinkage mechanisms, Creep, Shrinkage and Durability Mechanics of Concrete and other quasi-brittle Materials, Cambridge, MA (2001) 15-25.
[211] J. Pourchez, P. Grosseau, B. Ruot, Changes in C3S hydration in the presence of cellulose ethers, Cement and Concrete Research 40(2) (2010) 179-188.
[212] E. Knapen, D. Van Gemert, Cement hydration and microstructure formation in the presence of water-soluble polymers, Cement and concrete Research 39(1) (2009) 6-13.

[213] J. Beaudoin, Calcium hydroxide in cement matrices: Physico-mechanical and physico-chemical contributions, Calcium Hydroxide in Concrete in Materials Science of Concrete; American Ceramic Society: Westerville, OH, USA (2000) 131-132.
[214] B. Sindu, S. Sasmal, B. Saravanan, Evaluation of micro-mechanical properties of nonlinear cementitious composite using large-displacement transient nanoindentation analysis, Sādhanā 43(2) (2018) 1-15.
[215] M. Moradian, M.T. Ley, Z.C. Grasley, Stress induced dissolution and time-dependent deformation of portland cement paste, Materials & Design 157 (2018) 314-325.
[216] H. Grénman, T. Salmi, D.Y. Murzin, Solid-liquid reaction kinetics–experimental aspects and model development, Reviews in chemical engineering 27(1-2) (2011) 53-77.
[217] K. Velez, S. Maximilien, D. Damidot, G. Fantozzi, F. Sorrentino, Determination by nanoindentation of elastic modulus and hardness of pure constituents of Portland cement clinker, Cement and Concrete Research 31(4) (2001) 555-561.
[218] M. Vandamme, F.-J. Ulm, P. Fonollosa, Nanogranular packing of C–S–H at substochiometric conditions, Cement and Concrete Research 40(1) (2010) 14-26.
[219] Z. Yu, A. Zhou, D. Lau, Mesoscopic packing of disk-like building blocks in calcium silicate hydrate, Scientific reports 6(1) (2016) 1-8.
[220] G. Constantinides, F.-J. Ulm, K. Van Vliet, On the use of nanoindentation for cementitious materials, Materials and structures 36(3) (2003) 191-196.
[221] F. Pelisser, P.J.P. Gleize, A. Mikowski, Effect of the Ca/Si molar ratio on the micro/nanomechanical properties of synthetic CSH measured by nanoindentation, The Journal of Physical Chemistry C 116(32) (2012) 17219-17227.
[222] D. Fan, S. Yang, Mechanical properties of CSH globules and interfaces by molecular dynamics simulation, Construction and Building Materials 176 (2018) 573-582.
[223] H.M. Jennings, Refinements to colloid model of CSH in cement: CM-II, Cement and Concrete Research 38(3) (2008) 275-289.
[224] P.D. Tennis, H.M. Jennings, A model for two types of calcium silicate hydrate in the microstructure of Portland cement pastes, Cement and concrete research 30(6) (2000) 855-863.
[225] D. Hou, H. Li, L. Zhang, J. Zhang, Nano-scale mechanical properties investigation of CSH from hydrated tri-calcium silicate by nano-indentation and molecular dynamics simulation, Construction and Building Materials 189 (2018) 265-275.
[226] J. Li, W. Zhang, P.J. Monteiro, Preferred orientation of calcium aluminosilicate hydrate compacts: Implications for creep and indentation, Cement and Concrete Research 143 (2021) 106371.
[227] M. Vandamme, F.-J. Ulm, Nanoindentation investigation of creep properties of calcium silicate hydrates, Cement and Concrete Research 52 (2013) 38-52.
[228] P. Mondal, S.P. Shah, L. Marks, A reliable technique to determine the local mechanical properties at the nanoscale for cementitious materials, Cement and Concrete Research 37(10) (2007) 1440-1444.
[229] W. Zhu, J.J. Hughes, N. Bicanic, C.J. Pearce, Nanoindentation mapping of mechanical properties of cement paste and natural rocks, Materials characterization 58(11-12) (2007) 1189-1198.
[230] Z. Tan, S.A. Bernal, J.L. Provis, Reproducible mini-slump test procedure for measuring the yield stress of cementitious pastes, Materials and Structures 50(6) (2017) 235.
[231] A. International, ASTM C39/C39M-18 Standard Test Method for Compressive Strength of Cylindrical Concrete Specimens, ASTM International, West Conshohcken, PA, 2018.

[232] A. Perrot, C. Lanos, Y. Melinge, P. Estellé, Mortar physical properties evolution in extrusion flow, Rheologica Acta 46(8) (2007) 1065-1073.
[233] C. Gay, F. Sanchez, Performance of carbon nanofiber–cement composites with a high-range water reducer, Transportation Research Record 2142(1) (2010) 109-113.
[234] C. Stephens, L. Brown, F. Sanchez, Quantification of the re-agglomeration of carbon nanofiber aqueous dispersion in cement pastes and effect on the early age flexural response, Carbon 107 (2016) 482-500.
[235] F. Sanchez, C. Ince, Microstructure and macroscopic properties of hybrid carbon nanofiber/silica fume cement composites, Composites Science and Technology 69(7) (2009) 1310-1318.
[236] B.G. Compton, J.A. Lewis, 3D-printing of lightweight cellular composites, Advanced materials 26(34) (2014) 5930-5935.
[237] S. De, J. White, Short fibre-polymer composites, Elsevier1996.
[238] D.A. Norman, R.E. Robertson, The effect of fiber orientation on the toughening of short fiber-reinforced polymers, Journal of applied polymer science 90(10) (2003) 2740-2751.
[239] P. Stähli, J.G. Van Mier, Manufacturing, fibre anisotropy and fracture of hybrid fibre concrete, Engineering fracture mechanics 74(1-2) (2007) 223-242.
[240] J.E. Bolander, S. Choi, S.R. Duddukuri, Fracture of fiber-reinforced cement composites: effects of fiber dispersion, International journal of fracture 154(1-2) (2008) 73-86.
[241] F.P. Bos, E. Bosco, T.A.M. Salet, Ductility of 3D printed concrete reinforced with short straight steel fibers, Virtual and Physical Prototyping 14(2) (2019) 160-174.
[242] A. International, ASTM C293-08 Standard Test Method for Flexural Strength of Concrete (Using Simple Beam With Center-Point Loading), ASTM International, West Conshohcken, PA, 2010.
[243] E.I. Nadelman, K.E. Kurtis, Application of Powers' model to modern portland and portland limestone cement pastes, Journal of the American Ceramic Society 100(9) (2017) 4219-4231.
[244] Halloysite Nanoclay Safety Data Sheet, 2021. https://www.sigmaaldrich.com/US/en/sds/aldrich/685445.
[245] S. Allalou, R. Kheribet, A. Benmounah, Effects of calcined halloysite nano-clay on the mechanical properties and microstructure of low-clinker cement mortar, Case Studies in Construction Materials 10 (2019) e00213.
[246] K. Pietrak, T.S. Wiśniewski, A review of models for effective thermal conductivity of composite materials, Journal of Power Technologies 95(1) (2015).
[247] T. Singh, S. Shrivastava, H.S. Ber, Analysis of unsteady heat conduction through short fin with applicability of quasi theory, International Journal of Mechanical Engineering and Robotics Research 2(1) (2013) 269-283.
[248] Z.S. Spakovszky, 18.2 Heat Transfer From a Fin, 2006. https://web.mit.edu/16.unified/www/FALL/thermodynamics/notes/node128.html.
[249] Y. Han, Influence of 3D printing infill patterns on the effective thermal properties, The Journal of Purdue Undergraduate Research 6(1) (2016) 25.
[250] A. Elkholy, M. Rouby, R. Kempers, Characterization of the anisotropic thermal conductivity of additively manufactured components by fused filament fabrication, Progress in Additive Manufacturing 4(4) (2019) 497-515.
[251] S. Alqahtani, H.M. Ali, F. Farukh, V.V. Silberschmidt, K. Kandan, Thermal performance of additively manufactured polymer lattices, Journal of Building Engineering 39 (2021) 102243.

APPENDIX A: SUPPLEMENTARY MATERIAL FOR CHAPTER 3

Table A-1. Ranges of mean modulus values of the peaks determined via statistical deconvolution analysis of grid nanoindentation data for the high and low mechanical property (HMP and LMP) filaments and reference cast cement pastes.

	Peak 1 (GPa)	Peak 2 (GPa)	Peak 3 (GPa)	Peak 4 (GPa)
HMP filaments[a]	20.2-26.0	27.4-39.0	47.7-86.3	78.1-105.5
LMP filaments[b]	12.7-17.6	18.7-26.3	33.3-53.7	40.4-61.0
Cast – w/c=0.3[c]	23.5-27.8	32.7-44.4	88.1-106.3	103.7-115.4

[a] Ranges based on 6 HMP filaments obtained across 3 printed structures.

[b] Ranges based on 3 LMP filaments obtained across 3 printed structures.

[c] Ranges based on 3 cast replicates.

Table A-2. Ranges of mean hardness values of the peaks determined via statistical deconvolution analysis of grid nanoindentation data for the high and low mechanical property (HMP and LMP) filaments and reference cast cement pastes.

	Peak 1 (GPa)	Peak 2 (GPa)	Peak 3 (GPa)	Peak 4 (GPa)
HMP filaments[a]	0.9-1.1	1.4-2.2	6.4-9.2	9.2-10.5
LMP filaments[b]	0.8-1.0	1.4-2.1	4.7-7.2	6.6-8.4
Cast – w/c=0.3[c]	0.8-1.0	1.3-2.2	8.0-8.9	10.3-10.9

[a] Ranges based on 6 HMP filaments obtained across 3 printed structures.

[b] Ranges based on 3 LMP filaments obtained across 3 printed structures.

[c] Ranges based on 3 cast replicates.

Table A-3. Modulus deconvolution parameters for representative 3D printed filaments and cast specimens.

	Peak 1		**Peak 2**		**Peak 3**		**Peak 4**	
	$\mu \pm \sigma$ (GPa)	**Wt%**	**$\mu \pm \sigma$ (GPa)**	**Wt%**	**$\mu \pm \sigma$ (GPa)**	**Wt%**	**$\mu \pm \sigma$ (GPa)**	**Wt%**
HMP filament	25.8 ± 4.4	69.8	36.7 ± 7.6	11.6	79.5 ± 30.4	13.6	105.5 ± 5.2	5.0
LMP filament	17.6 ± 2.8	72.0	26.3 ± 5.9	13.1	53.7 ± 11.6	10.0	61.0 ± 3.1	4.8

Cast – w/c=0.3	24.7 ± 5.0	70.8	38.6 ± 8.8	13.1	93.6 ± 20.7	12.3	103.7 ± 5.8	3.8
Cast – w/c=0.5	17.1 ± 4.6	79.1	26.3 ± 9.0	17.5	81.5 ± 26.3	3.3	-	-

Table A-4. Hardness deconvolution parameters for representative 3D printed filaments and cast specimens.

	Peak 1		**Peak 2**		**Peak 3**		**Peak 4**	
	μ ± σ (GPa)	**Wt%**	**μ ± σ (GPa)**	**Wt%**	**μ ± σ (GPa)**	**Wt%**	**μ ± σ (GPa)**	**Wt%**
HMP filament	1.1 ± 0.2	72.6	1.8 ± 0.6	10.3	7.1 ± 3.5	11.5	10.5 ± 0.5	5.6
LMP filament	1.0 ± 0.2	75.7	2.1 ± 0.8	10.6	7.2 ± 1.9	8.0	8.4 ± 0.4	5.7
Cast – w/c=0.3	1.0 ± 0.3	74.9	2.2 ± 1.0	9.6	8.9 ± 2.8	9.8	10.3 ± 0.5	5.6
Cast – w/c=0.5	0.6 ± 0.2	83.3	1.35 ± 0.7	13.8	8.4 ± 2.9	3.0	-	-